CREEP DEFORMATION IN NICKEL BASE SUPERALLOY SINGLE CRYSTALS

by

Tresa M. Pollock

B.S.Met.E., PURDUE UNIVERSITY
(1984)

SUBMITTED IN PARTIAL FULFILLMENT
OF THE REQUIREMENTS FOR THE DEGREE OF
DOCTOR OF PHILOSOPHY
IN MATERIALS SCIENCE AND ENGINEERING

at the

MASSACHUSETTS INSTITUTE OF TECHNOLOGY

June 1989

Signature of Author Signature redacted
Department of Materials Science and Engineering
May 5, 1989

Certified by Signature redacted
Professor Ali S. Argon
Thesis Supervisor

Accepted by Signature redacted
Professor Samuel M. Allen, Chairman
Departmental Committee on Graduate Students

CREEP DEFORMATION IN NICKEL BASE SUPERALLOY SINGLE CRYSTALS

by

Tresa M. Pollock

Submitted to the Department of Materials Science and Engineering
on May 5, 1989 in partial fulfillment of the
requirements for the Degree of Doctor of Philosophy
in Metallurgy.

ABSTRACT

Creep deformation has been studied in $< 001 >$ nickel base superalloy single crystals in an effort to assess the factors contributing to the overall creep resistance of the two phase material. The details of the creep deformation process have been studied using stereo electron microscopy, mechanical tests, and finite element analysis.

Prior to the onset of normal primary creep there are incubation periods during which there is no externally measurable creep strain accumulated. These incubations are present because of the difficulty of spreading dislocations from widely spaced sources through the material. Very high stresses are required for shearing the ordered, dislocation-free γ' precipitates, which are individually isolated by 60 nm layers of γ matrix material. As a result, all deformation is confined to the matrix material until the very late stages of creep, when the stresses in the precipitates become very high. The forced Orowan bowing of the dislocations through the narrow matrix channels contributes a major portion of the creep resistance. Finite element analysis shows that further load carrying capacity is gained from pressure gradients which build up in the matrix material due to frictional constraint of the cuboidal γ' precipitates. There is also a smaller component of solid solution resistance.

In-situ annealing of TEM foils taken from steady state creep samples shows that static recovery is not effective in causing rearrangements in the very stable three dimensional nodal network which fills the matrix. As a result, at temperatures less than about 900°C, dynamic recovery is necessary for maintaining the "steady state" creep process. At temperatures higher than 900°C, static recovery becomes important. In addition, at these higher temperatures the precipitates merge to form long "rafts". The orientation of the rafts is dependent on the sense of misfit between the γ and γ' and the driving force for their formation is the reduction of elastic and γ/γ' interfacial energy.

Thesis Supervisor: Dr. Ali S. Argon
Title: Quentin Berg Professor of Mechanical Engineering

TABLE OF CONTENTS

Abstract 2

Acknowledgements 6

Introduction 7

Chapter One - Review of Creep Deformation in Nickel Base Alloys 10

1.1 Composition and Structure of Nickel Base Alloys 10

1.2 Creep Properties of Alloys with High Volume Fractions of γ' 12

1.3 Observed Modes of Creep Deformation 19

1.4 The Creep Equation and Creep Models 24

1.5 High Temperature Creep and Rafting 28

Chapter Two - Experimental Materials and Procedures 32

2.1 Nickel Base Single Crystal Material 32

2.2 Creep Specimens and Creep Testing 33

2.3 Stress - Strain Tests 34

2.4 Transmission Electron Microscopy 35

Chapter Three - Mechanical Tests 42

3.1 Steady Creep Experiments 42

3.2 Non-Steady Creep Experiments 43

3.3 Stress - Strain Experiments 44

Chapter Four - TEM Observations 55

4.1 The Aged Material 55

4.2 The Incubation Period 56

4.3 Primary Creep 58

4.4 Steady State Creep 66

4.5 Recovered Dislocation Structures 73

4.6 Structure Following Compression Testing 73

4.7 In-situ Annealing Observations 75

Chapter Five - Creep Resistance of the Two Phase γ/γ' Material 80

5.1 The Friction Hill Problem 80

5.2 The Finite Element Model 82

5.3 Results of the Displacement Control Analysis 86

5.4 Comparison of Finite Element Results with the 88

Schroeder and Webster Analysis

5.5 Load Control Analyses 93

5.6 Discussion 94

5.6.1 Microstructural Considerations 95

Chapter Six - High Temperature Rafting 98

6.1 Introduction 98

6.2 Rafting in Negative Misfit Crystals 100

6.3 Rafting in Positive Misfit Crystals 108

6.4 Discussion 111

Chapter Seven - Discussion and Conclusions 113

7.1 The γ' Precipitates 113

7.2 The Incubation Period 120

7.3 Deformation During Primary and Steady State Creep 125

7.4 Creep Resistance of the γ/γ' Material 126

7.5 Recovery 129

7.6 Conclusions 131

List of Tables 138

List of Figures 139

Appendix A - List of Alloy Compositions 146

Appendix B - Creep Curves 148

Appendix C - Finite Element Code 152

ACKNOWLEDGEMENTS

It is difficult to acknowledge all of the people who have helped me during my stay at MIT, and in advance I apologize to anyone who is neglected here in the final stages of this process.

It is with pleasure that I thank Professor Ali Argon for providing the opportunity for me to to pursue this work and for lending his insight and ideas to the problems addressed here. His commitment to research and teaching has been appreciated by this student.

I would also like to thank Professors Sam Allen, Robert Balluffi, and Regis Pelloux for their continued interest in my work over the past four years and for all of their helpful comments and criticism. Thanks are also due to Professor Frank McClintock for his input and attention to some of the details, and to Professor David Parks for his assistance with the finite element analyses.

Funding from the National Science Foundation and IBM is gratefully acknowledged. Material donated by Ram Darolia of General Electric is appreciated. This work would have been difficult without the continued generous donations of single crystals by Mehmet Doner of the Allison Division of General Motors.

Many other MIT people have provided valuable assistance and advice. Among these are Stuart Brown, Curt Bronkhurst, Tom Ference, Mike Frongillo, Mark Goorsky, Mehrdad Haghi, John Holmes, Janine Nell, Charlie White and Ed Zywicz.

Finally, there is no adequate way to acknowledge the sacrifices made by my husband so that this work could be completed. Thank you very much, Bill.

INTRODUCTION

Nickel base alloys have long been recognized as important engineering materials for applications which require high strength as well as a certain amount of toughness at temperatures in excess of 600°C. In the past two decades increases in maximum turbine inlet temperature and engine efficiency have been possible through metallurgical improvements of nickel base alloys as well as improved processing techniques for these materials. In particular, advances in solidification processing have enabled turbine components such as blades and vanes to be cast and utilized in single crystal form. With chemistry adjustments and the removal of grain boundaries, the maximum metal temperatures of single crystals in hot section components has increased by about 100°C.

During operation of a turbine engine, centrifugal and thermal stresses imposed on the blades result in maximum stresses of about 280 MPa at temperatures of 1100°C (i.e. $\sigma/\mu \sim 4\text{x}10^{-3}$ and $T/T_m \sim 0.85$) in the material near the blade tip [1], while the sections closer to the blade platform are subjected to lower temperatures and higher stresses. To maintain very close blade tip clearances, creep deformation must be kept to a minimum. For this reason creep data for strains less than 1% are important in the design process. However, it is usually steady state creep data for much larger strains which is available. In a recent report summarizing an effort to evaluate the state of advanced structural analysis techniques in blade design, one of the major conclusions was [2]: "The major discrepancy between the testing results and the analytical predic-

tions for this very severe thermomechanical cycle is due to the creep properties. Test results showed a much faster stress relaxation than had been analytically predicted. This suggests that the primary creep representation used was not accurate."

Although not a great deal of effort has been invested in studying the creep properties of nickel base alloys at small strains, it is obvious that such information is of importance. One problem with representing the primary creep behavior with constitutive models is the variety of primary creep responses observed for single and polycrystalline nickel base materials under different conditions of temperature and stress. In order to gain a thorough understanding of the creep response of these materials under realistic conditions it will not only be necessary to study the mechanical response of the material but also the mechanisms of creep deformation. Once an understanding of the details of the deformation is gained, meaningful constitutive models for use in design may be developed. Also, a detailed understanding of creep deformation processes may suggest methods for improving the microstructure and chemistry of alloys in a way alternate to the conventional method of alloy development which explores a large range of compositions and heat treatments and then optimizes properties through large-scale mechanical testing programs.

A review of the state of understanding of creep deformation in nickel base alloys will show that very high activation energies and stress exponents characterize the process. Limited TEM observations show a variety of apparent modes of deformation, and provide very little information about evolution of the dislocation structures or the steady state creep processes. Complicating the picture is the inherent instability of the precipitates at the temperatures where these alloys are useful.

The objective of this research was to first build a detailed understanding of the creep process under a selected set of conditions where the precipitates were relatively

stable in shape and distribution. The response of the material to various modes of deformation in the temperature range of 800° - 900°C was investigated and the results are reported in Chapter 3. The evolution of the dislocation structure was then studied with emphasis on the early stages of the creep deformation process (small strains). Stereo electron microscopy was particularly useful in understanding the arrangements in this geometrically well organized structure, and this is discussed in Chapter 4. A finite element model of the two phase microstructure was formulated, and although the creep deformation problem is not entirely a continuum problem, the finite element results provide some additional insight into the micromechanics of this particular two phase material deformation problem. This is found in Chapter 5. Chapter 6 reports the preliminary findings of some experiments aimed at understanding the creep process at higher temperatures, where the precipitates change shape very quickly under the influence of an applied stress. Finally Chapter 7 includes a general discussion of the creep deformation process in γ/γ' nickel base alloys and also the final conclusions of the research.

Chapter One

REVIEW OF CREEP DEFORMATION IN NICKEL BASE ALLOYS

Prior to discussing the results of studies on creep in nickel base single crystals, a short review of the composition and structure of nickel base alloys will be presented. Following this will be a review of the current understanding of the creep deformation problem. Because of the dramatic differences between the microstructures of more recently developed alloys which have very large volume fractions of γ' and earlier nickel base alloys which generally had less than 30% γ', this review will concentrate on high volume fraction γ' alloys. In addition, since single crystal alloys have only two phases (no carbides or borides) and no grain boundaries, the discussions will emphasize single crystals, with the idea that basic information about creep processes is more likely to be found in the less complicated single crystals.

1.1 Composition and Structure of Nickel Base Alloys

Nickel base alloys, or superalloys, are a class of two phase precipitation strengthened materials. In general they have a fcc nickel solid solution matrix (γ) with up to 70 volume percent γ' (Ni_3Al) which is ordered and coherent with the matrix. The misfit between the γ and γ' phases is minimal and in most commercial alloys is less than 0.5%. Typically there are between 6 and 15 alloying elements, as can be seen in Appendix A in the list of alloy compositions. Each alloying element is usually added

for a primary purpose, but there are certainly less prominent secondary consequences of adding or removing elements to or from a particular alloy.

Solutes of Cr, Co, Re, Mo, and W are found primarily in the matrix material. All five of these elements provide solid solution strengthing to the matrix. In addition, Cr is added for corrosion and oxidation resistance. Ti, Ta, and Nb partition primarily to the ordered Ni_3Al phase. They influence the volume fraction of γ' which will be formed during heat treatment as well as strengthen the γ' phase. In addition, in polycrystalline alloys, C, B, Hf, Zr segregate to grain boundaries and/or form additional phases which are thought to lead to improved high temperature properties.

Most of the more recently developed alloys and all of the commercial single crystal alloys have volume fractions of γ' in excess of 0.55, with the single crystal alloys usually around 65 volume percent γ'. The shape of the γ' precipitates has been observed to be dependent on size and relative magnitude of lattice mismatch between the γ and γ' phases. The γ' morphology can be roughly classified as spherical, cuboidal, or irregular. For a given level of misfit, the morphology will change from spherical to cuboidal to irregular as the precipitate coarsens, and the transition from spheres to cubes will occur at smaller γ' sizes for higher levels of misfit [3]. The cubes have $\{100\}$ type faces, which is undoubtedly due to elastic anisotropy of the system. The spherical γ' is completely coherent with the matrix, the cuboidal shape is usually coherent or semi-coherent and the irregular precipitates have nearly always lost coherency, with arrays of dislocations at the interfaces.

The two phase structure is produced by a two or three step heat treatment. In the first step the irregular γ' present following the casting process is put back into solution at a temperature which is often very near the melting temperature of the alloy, and in the case of single crystal alloys near 1300°C. With the removal of C, B,

Hf, and Zr, which often form low melting point phases, nearly complete dissolution of the primary γ' is possible, which is desirable in producing a uniform final structure. During cooling from the solution treatment temperature, γ' precipitates nucleate and begin to coarsen. An aging treatment in the range of 950°C - 1100°C, which is often determined by the requirements of the coatings applied, establishes the final γ' size, usually in the range of 0.2 - 0.5 μm in diameter.

1.2 Creep Properties of Alloys with High Volume Fractions of γ'

Most creep data available for high volume fraction γ' superalloys is in the temperature range of 760 - 1100°C at stresses up to 750 MPa. These conditions reflect a combination of the temperature range in which the materials are used, and the need to generate material properties in a reasonable length of time. Due to the anisotropic elastic properties of the single crystals, components are cast with the $< 001 >$ orientation corresponding to the major loading direction. The elastic modulus is a minimum in this orientation, giving a maximum resistance to thermal fatigue. In the $< 001 >$ orientation there are eight equally stressed slip systems, and no significant lattice rotations occur if all systems operate. For these reasons the majority of the information reported for nickel base single crystals is for crystals in the $< 001 >$ orientation. Unless otherwise stated, it can be assumed that the data reported here is for $< 001 >$ crystals.

In the temperature range of 760°C to 1000°C, the creep response of these alloys varies quite widely. Figure 1.1 shows some representative creep curves for several different $< 001 >$ oriented single crystals. The creep curves may show a regular three stage behavior with a primary transient followed by a period of steady state creep, and then tertiary creep and fracture. However, the primary transient is sometimes completely absent, as is the case for Curve 3 (Mar-M-200 at 855°C and 415 MPa). At

lower temperatures and higher stresses "steady state" may be more accurately defined as a short period of minimum creep rate followed by an extended tertiary transient, as in Curve 2. A long period of constant minimum creep rate, or true steady state creep, is usually only established at higher temperatures/lower stresses, shown by Curve 5 for Ni-13Al-9Mo-2Ta. At higher temperatures a well defined steady state creep rate is also established in single crystal alloys NASAIR 100 [11], Ni-5.8Al-14.6Mo-6.2Ta [12] and CMSX-2 [10]. The creep behavior is usually not found to be sensitive to small deviations from the $< 001 >$ orientation, and it has been suggested that there is little orientation dependence at deviations as high as 20^o from the $< 001 >$ [30,31].

It should be emphasized that within the temperature range of interest here, the γ' precipitate shape is usually to some extent unstable. During creep the precipitates "directionally coarsen" into long stringers or "rafts" extending anywhere from several to fifty microns in length. During very high temperature creep, the rafts develop very quickly, and are well formed even during the primary creep transient [12]. Once they are developed the precipitate arrangement is very stable until tertiary creep. At lower temperatures the rafts develop much more slowly and may only be of the order of several precipitate diameters [7,13]. There has been some discussion about whether the long continuous increase in creep rates, such as seen in Curves 2 and 3, is caused by the instability of the precipitates [14,15], but this issue does not appear to be resolved at the present time. The subject of rafting will be discussed further in a following section.

In Table 1.1 is a compilation of creep stress exponents and activation energies for high volume fraction γ' alloys in the polycrystalline, directionally solidified and/or single crystal form. These exponents and activation energies are calculated from the steady state creep data with the assumption that the thermally activated creep pro-

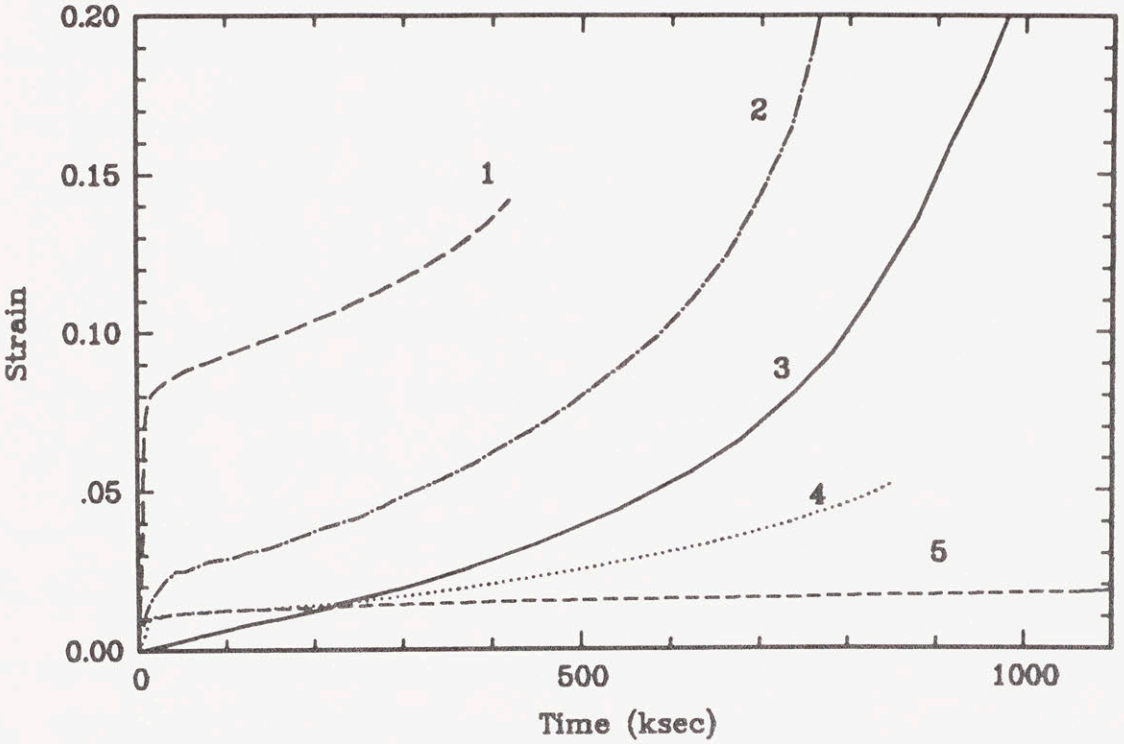

Figure 1.1 Creep curves for < 001 > single crystal alloys.
1 - SRR99, 750°C and 800 MPa (4)
2 - Mar-M-200, 760°C and 690 MPa (5)
3 - Mar-M-200, 855°C and 415 MPa (6)
4 - NASAIR 100, 760°C and 793 MPa (7)
5 - Ni-13Al-9Mo-2Ta, 1038°C and 207 MPa (8)

cesses are represented by the power law expression:

$$\dot{\varepsilon}_{ss} = A\left(\frac{\sigma}{\mu}\right)^{n} exp\left(\frac{-Q}{RT}\right) \tag{1}$$

where A is a constant having dimensions of reciprocal time, σ the uniaxial applied stress, μ the shear modulus, n the creep stress exponent, Q the activation energy for creep and R and T are the gas constant and absolute temperature, respectively. The activation energy for self diffusion in nickel is 280 kJ/mol [27], and if the creep process is diffusion controlled, it could be expected that the activation energy for creep would be equal to that for self diffusion. This is the case for pure metals and single phase alloys [28], but in general is not found to be true in two phase alloys, as can be seen in Table 1.1 for these $\gamma/\ \gamma'$ alloys. The listed nickel base alloys have activation energies in the range of 370 - 720 kJ/mol. In the case of polycrystalline alloys, there are usually two different activation energies and creep stress exponents for low and high stress regimes, as shown for IN738LC and IN100. In the lower stress regime grain boundary sliding occurs, while at higher stresses there is no noticeable grain boundary sliding [26]. The stress exponents in Table 1.1 range from 4.1 to 16., with many of the single crystals having creep stress exponents close to 8. Again, this is higher than the stress exponents usually observed in pure fcc metals and single phase solid solution alloys, which have creep stress exponents around 5 [29]. The reasons for these differences between single phase and two phase materials are not clear, and this will be discussed in later sections.

Looking at the creep behavior at very short times for several different single crystal alloys, several different types of behavior are found. In Figure 1.2 a normal primary creep response is shown by Curve B for NASAIR 100 at 1000°C - 207 MPa. However, for the other three materials there is an incubation period prior to the onset of creep at a significant (measurable) rate. The incubation may be followed by a normal primary

Table 1.1 Experimentally measured creep parameters for a variety of high volume fraction γ' nickel base alloys.

Material	Q (kJ/mol)	n	Volume Fraction γ'	γ' shape	Reference
NASAIR 100*	350	7.2-7.6	0.68	cuboidal	21
SC Mar-M-200*	627	7.7	0.60	irr. cube	5
DS Mar-M-200	566	–	0.60	irr. cube	16
SC Ni-7Ta-6Cr 5Al-2Mo*	565	11.	≈0.60	cuboidal	13
SC IN100*	–	11.3	≈0.60	cuboidal	22
SC Mar-M-247*	–	6.4	0.65	cuboidal	9
AF 115 (d=12.7μm)	520	15.	0.69	cuboidal	24
B6 (d=9μm)	700	16	0.68	spherical	24
MERL 76 (d=20μm)	370	7	0.67	cuboidal	24
					24
Ni-5.8Al-14.6Mo 6.2Ta*	475	8.7-10.9	≈0.60	cuboidal	12
IN738LC (high σ) d=2mm	570-730	8.3-9.8	0.48	bimodal	25
IN738LC (low σ)	370-420	4.1-4.9	0.48	bimodal	25
IN100 (high σ) d=0.2-0.5mm	720	8.5	0.55	cuboidal	26
				cuboidal	
IN100 (low σ)	440	4.5	0.55	cuboidal	26

* denotes a single crystal material

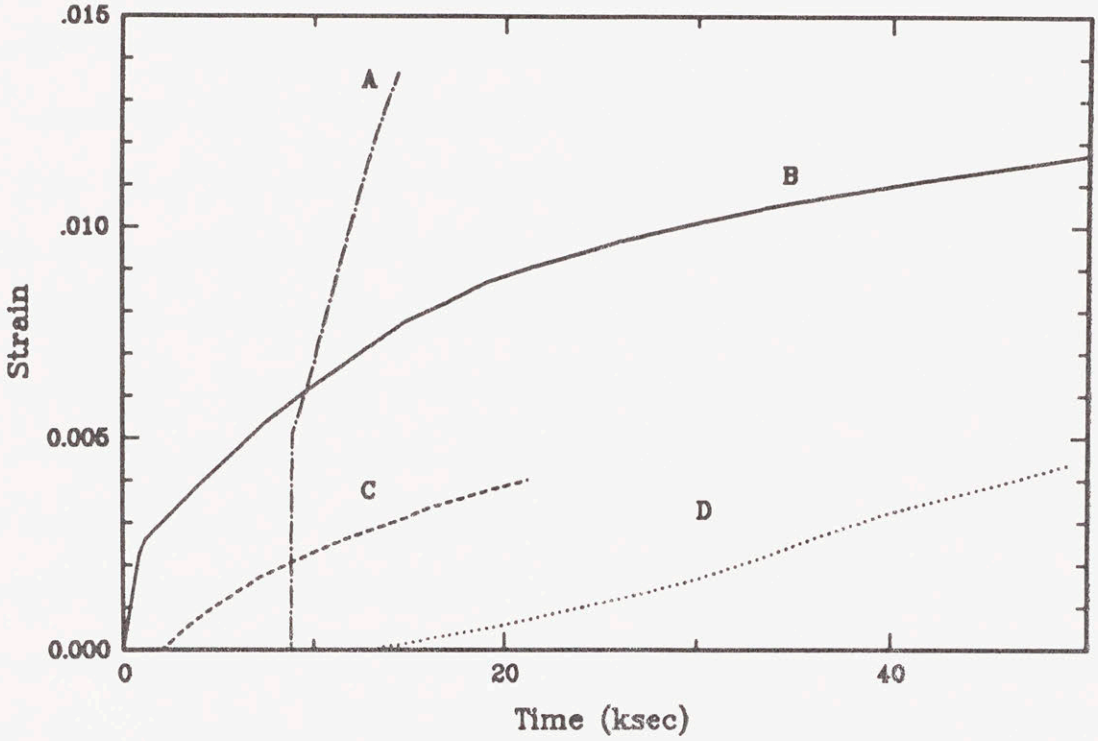

Figure 1.2 Small strain creep curves for $< 001 >$ single crystals.
A - Mar-M-200, 760°C and 689 MPa (5)
B - Alloy B, 1000°C and 207 MPa (9)
C - CMSX-2, 760°C and 750 MPa (10)
D - Alloy E, 1000°C and 207 MPa (9)

transient as shown by Curves A and C, or there may be a gradually accelerating creep rate, shown by Curve D. The incubation period may disappear for slightly different heat treatments [10] and through the introduction of dislocations by subjecting a sample to a shock wave [5]. Webster and Piearcey [16] in testing creep specimens with 0.250" diameter cylindrical gauge sections noted that even the surface condition of the sample influenced the incubation, with an electropolished sample showing an incubation period, while samples which were tested in the as-machined or surface sand-blasted condition showed no incubation at 760°C and 586 MPa.

It should also be noted that the amount of the primary creep strain varies rather dramatically for the materials shown in Figure 1.2. The primary creep behavior is shown to be dependent on the heat treatment given to the alloy [4,10,19], which of course could influence the volume fraction of the γ' as well as the size, shape and chemical composition. In single crystal and directionally solidified alloys, the primary creep strains are generally observed to be smaller at higher temperatures, and are very stress dependent at 760°C [20]. In polycrystalline Waspaloy, the amplitude, shape and length of the primary transient is found to be dependent on the grain size [17], with a finer grain size (ASTM 8.5) material accumulating less strain in the first 100 hours than the coarser grain size (ASTM 3.5) at 760°C and 379-448 MPa. (The creep strains were less than 0.1% and the material with coarse grains showed better steady state creep resistance.) Caron and Khan [18] report the amount of primary creep in single crystal alloy MXON to be sensitive to the level of Co and the γ' size, with these factors influencing the creep process through their effect on the homogeneity of primary creep deformation.

It should be pointed out that while it is easy to observe changes in creep behavior for changes in chemistry or heat treatment, it is difficult to establish the exact reason

for these changes, and almost impossible without examining in detail the changes in the γ' size, volume fraction and distribution as well as the resultant dislocation structures produced by the creep process. Where the information is available, some of the above observations will be discussed with emphasis on the γ/γ' arrangements and the dislocation structures produced by creep.

1.3 Observed Modes of Creep Deformation

Information concerning dislocation structures developed during creep deformation in nickel base alloys is limited. Even when there is an effort to study the deformation structures, a clear understanding of the creep deformation mechanisms rarely emerges. The information that is available can be roughly divided into three categories; (1), low temperatures/high stresses; (2), intermediate temperatures/intermediate stresses; and (3), high temperatures/low stresses. Limited observations show definite differences in the dislocation and precipitate structures in these three regimes and they will be summarized.

A point of interest which should be emphasized is that although there is a rise in flow stress with temperature with high rates of deformation, giving peak flow stresses around 800°C [65], there is no corresponding rise in creep resistance (at low rates of deformation) in this temperature range [73].

1.3.1 Low Temperatures / High Stresses

Here low temperatures are defined to be between 750 and 760°C. At these temperatures the precipitates retain their shape and distribution during the creep process in all alloys with moderate levels of misfit (<0.5%).

Leverant and Kear [5] studied dislocation structures following creep deformation at 689 MPa in Mar-M-200 single crystals (Curve 2 in Figure 1.1 and Curve A in Figure 1.2). The crystals had 60% γ' precipitates in the form of 0.25μm rounded cubes.

During primary and steady state creep, the γ' was sheared and intrinsic/extrinsic fault pairs were formed by the penetration of pairs of a/2< 112 > dislocations from the matrix. Lattice rotations measured by X-ray diffraction are consistent with these observations [39]. The magnitude of the primary creep, which may be as high as 6%, is thought to be dependent on the number of {111}< 112 > systems activated [5]. This mode of deformation during primary creep is reported for many alloys at these temperatures and stresses. Among these are CMSX-2 [10], SC Mar-M-247 [32], IN100 [22], and SRR99 [4]. It is fairly easy to identify this mode of γ' shearing since stacking faults extend across the diameter of the precipitates. In all of these cases a three stage creep curve of the type shown by Curve 2, Figure 1.1 was observed. An incubation period was reported for Mar-M-200.

One exception to this mode of γ' shearing during primary creep is reported for NASAIR 100 [7] at stresses of 600 and 793 MPa. Under these conditions, {111}< 110 > dislocations are reported to move long distances through the matrix during primary creep (Curve 4), and stacking faults in the precipitates are not observed until well into steady state. Fewer stacking faults are observed for the samples tested at 600 MPa than for those tested at 793 MPa.

Networks of a/2< 110 > dislocations at the γ/γ' interfaces during steady state creep are observed for all of the above materials. Some stacking faults are also reported to be present during steady state creep for IN100 [22], and SRR99 [4]. Shearing of the γ' by pairs of a/2< 110 > dislocations during steady state creep is observed in CMSX-2 [10].

To summarize, in most alloys shearing of the γ' by pairs of $a/2 < 112 >$ dislocations during primary creep is a common event. During steady state creep several different modes of deformation are reported, but since the steady state dislocation structure

is characterized by a much higher dislocation density, there is really no convincing evidence of a rate controlling mechanism for creep.

1.3.2 Intermediate Temperatures / Intermediate Stresses

Intermediate temperatures and stresses describes the temperature range of 800 - 900°C and stresses of 250 - 550 MPa. Under these conditions, the precipitate shape is still fairly stable, with only limited linking of the precipitates during longer creep experiments. There are widely varied observations with respect to the type of creep curve and dislocation arrangements in this temperature and stress range.

After creep deformation at 850°C and 250 MPa in Ni-10.7Al-1.2Ta-6.71Cr-1.21Mo single crystals oriented 15-17° from the < 001 >, Carry and Strudel [33] have observed fairly long, straight dislocations emerging from sharp subgrain boundaries and gliding on {110} planes during an incubation period which lasts for 41 hours. They report that edge dislocations are deposited on interfaces, and regardless of the temperature and stress, the incubations last until a critical strain of about 2-3x10^{-4} is accumulated. The creep curve is inverted, showing no primary or steady state transient. They also report a threshold stress for deformation in the range of 160 - 190 MPa. They find no shearing of the γ' precipitates during creep at these stresses and dense edge dislocation arrays which build up with time at the γ/γ' interfaces.

At 857°C and 414 MPa for Mar-M-200 single crystals, a creep curve with a continuously increasing creep rate is observed (Curve 3, Figure 1.1). Extensive networks of a/2< 110 > dislocations at the γ/γ' interfaces are present during steady state creep, and Leverant et.al., suggest that the rate of creep deformation is controlled by shearing of the γ' precipitates by a< 110 > dislocations [66].

For SC PWA 1444 at 899°C - 380 MPa, Giamei [34] finds that during primary creep (0.2% creep strain) multiple {111}< 110 > systems are operating, producing a

homogeneous distribution of dislocations and no lattice rotation. There is no mention of the dislocation structure during steady state creep, so it is not clear whether the precipitates are being sheared in this case.

In polycrystalline IN100 Dennison, Holmes, and Wilshire [26] report a high density of matrix dislocations which are bowing around the γ' precipitates at 900°C and stresses greater than 200 MPa. At lower stresses they observe sliding grain boundaries and deformation in zones adjacent to grain boundaries. They find this to be the reason for the different stress exponents and activation energies in the high and low stress regimes, as shown in Table 1.1. In all cases they observed regular three stage creep curves.

The microstructure of IN738 consists of a bimodal distribution of 1μm cuboids and 90 nm spheroids. In polycrystalline IN738 at 850°C and stresses below 300 MPa, Stevens and Flewitt [14] see no evidence of dislocations cutting either the cuboids or spheroids, but report that the spheroids are bypassed by a combined climb/glide process. Raising the stresses to 400 MPa leads to shearing of both the spheroids and the cuboids. They find no Orowan loops in either case. Unlike Dennison et. al., they attribute the rise in the stress exponent from (n=6.1 to 9.6) to be due to this change in mechanisms. In other work on IN738LC (carbon reduced from 0.17% to 0.12%), Jianting et.al. [25] observe Orowan looping at 850°C - 307 MPa in a range where the stress exponent is n=8.8, and they also postulate that the decrease in stress exponent to 4.9 is due to the transition to a climb process. Henderson and McLean [35] heat treated DS IN738LC to obtain only irregular cuboids, with no small spheroids. After creep at 850°C - 270 MPa there is a high density network of dislocations associated with the γ/γ' interface. They find that the density of the dislocations continues to increase throughout the creep test [23], and also assume that the dislocations are

climbing around the precipitates. Unfortunately no stress exponents are reported for the DS alloy.

There is very little agreement in observations even among the single crystal alloys in this temperature and stress range, and even less agreement on polycrystalline alloys (in particular IN-738). This seems to be in part due to the fact that the dislocation densities are very high, making it difficult to interpret the TEM micrographs.

1.3.3 High Temperatures / Low Stresses

At temperatures above 950°C, the γ' precipitates are unstable and quickly form rafts during creep. This is widely observed in single crystal alloys [3,8,10,11,12,21,22,36]. The shape changes of the precipitates will be discussed in more detail in section 1.5.

At these high temperatures almost all of the dislocations are associated with the interfaces. They are always observed to be of the $a/2< 110 >$ type [10,36,60]. Alloys with higher levels of misfit have more closely spaced networks at the interfaces at these temperatures [37], indicating that these organized networks must be retained to relieve the γ/γ' misfit.

Caron and Khan [10] observe shearing of the rafts by pairs of $a/2< 110 >$ dislocations during steady state creep at 1050°C - 120MPa. Nathal and Ebert [21] also observe shearing of the rafts during steady state creep at 1000°C and 148 MPa for NASAIR 100. For the rest of the single crystal alloys, this aspect of the problem is not investigated. In general there is much information about the shape changes of the precipitates, but very little information about the dislocation structures following creep at these temperatures.

Samples of Alloy MMT143 prerafted at 1038°C - 207 MPa show improved creep properties at 899°C - 414 MPa [8], while recent experiments on prerafted samples of NASAIR 100 (1000°C - 148 MPa) showed degraded creep properties at 760°C and

stresses of 793 and 600 MPa [7]. While it has usually been accepted that the rafted structure is beneficial to the overall creep resistance, this is obviously not true in all situations. The reasons for this are unclear.

1.4 The Creep Equation and Creep Models

From the previous discussion it seems clear that the present understanding of the creep process in nickel base alloys is incomplete. In *pure materials and single phase alloys* the experimentally established correlation of the activation energy of creep with that for diffusion [28] and the common creep stress exponents [40] has provided motivation for the form of the creep equation known as the Dorn equation:

$$\dot{\varepsilon}_{ss} = A\frac{\mu b}{kT}\left(\frac{\sigma}{\mu}\right)^{n} exp\left(\frac{-Q}{RT}\right) \tag{2}$$

where all of the parameters have their usual meaning.

As a result of a more recent compilation of creep data, Brown and Ashby [53] propose that there is a further correlation between A and n of the form

$$A = (C_o)^{n-2.70} \tag{3}$$

this changes the steady state creep equation to:

$$\dot{\varepsilon}_{ss} = A'\frac{\mu b}{kT}\left(\frac{\sigma}{\mu/C_o}\right)^{n} exp\left(\frac{-Q}{RT}\right) \tag{4}$$

Since μ/C_o is approximately equal to the yield stress, the equation can be written:

$$\dot{\varepsilon}_{ss} = A'\frac{\mu b}{kT}\left(\frac{\sigma}{\sigma_o}\right)^{n} exp\left(\frac{-Q}{RT}\right) \tag{5}$$

This form of the equation is then much like the familiar Norton Law:

$$\dot{\varepsilon}_{ss} = \dot{\varepsilon}_o\left(\frac{\sigma}{\sigma_o}\right)^{n} \tag{6}$$

where $\dot{\varepsilon}_o$ is a reference strain rate and σ_o a reference stress.

Ideally, using representative dislocation models of the hardening and diffusion controlled recovery processes which are likely to occur during high temperature creep, a creep equation which agrees with the above stress and temperature dependence can be formulated. In the case of pure materials and solid solution alloys, there have been attempts [41-45], but no widely accepted explanation for even the steady state creep equation. Variables which account for changes in isotropic deformation resistance [46] or internal stresses due to the characteristic inhomogeneous dislocation arrangements [47-50] have been used to explain transient behavior and the value of the creep stress exponent.

With nickel base alloys, the power law creep exponents and activation energies are much higher than observed for pure materials and single phase alloys, leaving some doubt as to whether the mechanisms of creep deformation are the same in these microstructurally very different materials. In spite of this, some attempts at identifying rate limiting mechanisms and formulating creep equations for nickel base alloys have been made, and these will be briefly discussed.

The common approach to describing creep in nickel base alloys is to assume that it is a diffusion controlled process which can be represented by:

$$\dot{\varepsilon}_{ss} = A\left(\frac{\sigma_e}{\mu}\right)^n exp\left(\frac{-Q}{RT}\right) \tag{7}$$

where σ_e is the effective stress driving the creep process. There are then various representations for σ_e, and also different interpretations justifying each form.

Carry and Strudel [33] propose that $\sigma_e = \sigma_a - \sigma_i$ where σ_a is the applied stress and σ_i is the average internal stress in the material. The internal stress is given as

$$\sigma_i = \alpha\sigma_a + \sigma_c \tag{8}$$

with σ_a and σ_c equal to the applied and threshold stresses respectively, and α a con-

stant. The change in internal stress with applied stress is given by σ_i' ($=\partial\sigma_i/\partial\sigma_a$) and the change in internal stress with temperature is σ_i^* ($=\partial\sigma_i/\partial T$). The resultant apparent (measured) stress exponent and activation energy in terms of effective (calculated) parameters are:

$$n_a = n_e \frac{\sigma_a}{\sigma_e}(1-\sigma_i') \tag{9}$$

$$Q_a = Q_e - RT^2 n_a \frac{\sigma_i^*}{\sigma_a(1-\sigma_i')} \tag{10}$$

where the subscripts a and e represent apparent (measured) quantities and effective (calculated) quantities, respectively. Using positive misfit single crystals, stress dip experiments during creep were performed as described in [50] to determine σ_i' and σ_i^*. The effective stress exponent was calculated to be n_e = 1 - 2 (n_a = 11) and the effective activation energy was Q_e = 251 kJ/mol, reduced from Q_a = 565 kJ/mol. The internal stresses were attributed to walls of edge dislocations which aggravate the misfit on the faces of the precipitates parallel to the applied stress. The climb of these edge dislocations is proposed to be the strain producing and rate controlling mechanism of creep. The high stress exponents are then due to the combined effect of a temperature dependent threshold stress due to the presence of the precipitates, and the internal stresses due to the walls of edge dislocations, while the high activation energies are caused by the variation of the internal stress with temperature.

Dennison, Holmes and Wilshire [26] also performed stress dip experiments on polycrystalline IN100 to determine a parameter σ_o. Their resulting creep equation is:

$$\dot{\varepsilon}_{ss} = A\,(\sigma-\sigma_o)^p\, exp\left(-\frac{Q_c'}{RT}\right) \tag{11}$$

Again, σ_o varies with temperature and applied stress and plotting $\sigma - \sigma_o$ as a function of steady state creep rate gives p=4 and an Q_c' = 320 kJ/mol, which would be

comparable to expected values for a single phase material. In this analysis there is no effort to assign a physical significance to the levels of σ_o. (In similar work using this approach [14,54] the parameter σ_o is said to be the threshold stress for bypass climb of dislocations around the precipitates, however these models appear to be only applicable for the case of very low volume fractions of γ'.) The remaining "effective stress" is then thought to be acting on a three dimensional network of dislocations as described by Friedel [51]. (In the Friedel model the dislocation links in a three dimensional network must diffusionally lengthen in order to act as dislocation sources. The model predicts a stress exponent of 3, while the effective stress exponent here is 4.) The gradual increase in creep rate (as in Curve 2, Figure 1.1) is attributed to precipitate coarsening.

Along slightly different lines Henderson and McLean [35] interpret stress dip data by fitting it with the expression:

$$\sum \Delta t = \frac{(\mu b)^2}{K}[(\sigma_R - \sigma_o)^{-2} - (\sigma_a - \sigma_o)^{-2}] \tag{12}$$

where $\sum \Delta t$ is the cumulative incubation time following stress dips, σ_R is the stress remaining after the load reduction, σ_a is the original applied stress, and σ_o is the friction stress. In contrast to other work, they find σ_o to be independent of the initial applied stress and only slightly temperature dependent. Henderson and McLean explain σ_o as the threshold stress for dislocation climb. Instead it is determined that K increases significantly during creep. They find this to be a confirmation of increased recovery kinetics, and the reason for the gradual increase in the creep rate. The parameter K comes again from the Friedel theory and is equal to:

$$K = \left(\frac{D\mu b^3}{kT}\right) C_j \tag{13}$$

where C_j is the concentration of jogs, and D is the self diffusion coefficient. Along with

the increase in K ("recovery kinetics") they find an increased density of dislocations at the γ/γ' interfaces, which they find consistent with their explanation of increased recovery kinetics.

It is obvious that the interpretation of stress dip data is not straightforward, and there have been questions about the validity of assigning physical meaning to the parameters measured [29,52]. A better understanding of the creep process in high volume fraction γ' alloys will be necessary before a consistent physical model of the steady state creep process can be agreed upon.

1.5 High Temperature Creep and Rafting

As discussed earlier, during high temperature creep testing the γ' precipitates are unstable. This is not surprising since an aging heat treatment in the temperature range of 980 - 1080°C is used to develop the two phase structure. It has been widely observed that in alloys with a significant amount of misfit that the precipitates will directionally coarsen during a creep test. Since most useful alloys have negative misfit at high temperatures, it is very common to observe "rafts" developing in a direction normal to the applied stress [3,8,10,12,19,21,22,36,38] during tension creep. The rafts are described as broad, flat plates with their faces *normal to the applied tensile stress* [22,55]. The rafts have {100} type faces, but as the precipitates become large, the interface is not clearly planar as it usually is for the precipitates in their aged condition.

When a negative misfit single crystal is deformed in compression, then a different arrangement of the precipitates is observed. Tien and Copley [55] show rods aligned parallel to the direction of compression for testing of Udimet 720 at 954°C and 155 MPa. For NASAIR 100 at 1000°C after 18.3 hours [11] Nathal and Ebert observe long rafts of γ' *parallel to the compression direction.* However, unlike Tien and Copley the plane normal to the compression axis shows two orthogonal sets of rafts, implying

that there are two different sets of broad plates with faces parallel to the compression axis. Although there are many reports of "rafting", the usual method of reporting the change in precipitate shape is to show only a {100} face which is parallel to the loading axis, so it not possible to conclude with certainty what three dimensional shapes the precipitates assume.

Some additional interesting observations have been made by Nathal, MacKay and Ebert on various negative misfit single crystals [3,12,19]. The thickness of the rafts during primary and steady state creep remains essentially unchanged from the original γ' diameter. The raft length increases quickly, with well formed rafts present during primary creep at strains of less than 0.005. However, the thickness and the interlamellar spacing of the rafts is reported to remain constant. This seems to imply that there is a volume fraction change. There have been no reports to confirm that the volume fraction γ' does remain constant. Rafts are also observed to form much more quickly in microstructures which initially have small γ' and no interfacial dislocations than in those which have larger γ' plus interfacial dislocations. An apparent activation energy for the rate of development of rafts in a Ni-Al-Mo-Ta alloy at 179 MPa is found to be 380 kJ/mol. From the limited data presented, it appears that the activation energy is stress dependent, since higher stresses lead to more rapid formation of the rafts.

For single crystals with positive misfit at temperature, the opposite tension / compression behavior is reported. Miyazaki, Nakamura and Mori [56] performed tension and compression experiments on Ni-15Al (δ_{RT}=.00563) at 750°C. The initial precipitate size was 70 nm, and although the volume fraction Ni_3Al was not measured, a Ni-Al phase diagram estimate gives $V_f \approx 0.27$. In this case, rods form *parallel to the tension axis, but normal to the compression axis.* At longer annealing times under stress, plates rather than rods were present. Rods and plates were also observed for

annealing under no stress, but with no preferential orientation. (Interestingly, raft-like structures are reported for annealing under no stress for a higher volume fraction Ni-6.25Cr-16.25Al-2.5Ru γ/γ' alloy [57].) In another recent study on Ni-Al-Mo single crystals [58] with volume fractions of γ' near 0.10, two alloys which had 0% and -0.1% misfit at 750°C, retained spherically shaped γ' under creep and aging conditions at 750°C. Conversely, an alloy which had a misfit of +0.4% at this temperature formed plates whose long edges were perpendicular to the direction of applied compressive stress (250 MPa). In both of these Ni-Al alloys the plates were only on the order of 0.2-0.5μm in length, contrasting with the rafts that form in the negative misfit alloys, which are often observed to be on the order of 10-20μm in length. Also in these two studies there is no mention of the dislocations which must certainly be present during creep.

It should be noted that since the level of the misfit is low and changing with temperature due to differences in thermal expansion in the two phases [59], it is not always easy to determine with confidence the misfit. This has been until recently a source of confusion, since some reported values of misfit change sign from room temperature to testing temperature [55] , or a wrong sense of the positive/negative aspect is assigned when measuring dislocation spacings after aging. It is also not likely that the misfit is completely relieved when aging at high temperatures. An informative comparison of several methods of measuring misfit in these alloys has recently been completed [60], and some of these issues are addressed.

Attempts have been made to explain the rafting behavior by determining what shape of an ellipsoidal inclusion would minimize the elastic strain energy under the influence of a tensile or compressive stress [56,61]. This is done by the Eshelby method of considering an inclusion in an infinite matrix, where the total elastic energy per

unit volume is due to the energy of the misfitting inclusion, the energy due to the interaction between the external stress and the elastic strain field of the inclusion, and the energy due to the differing elastic constants. The correct sense of inclusion orientation with respect to sense of applied stress is predicted, but the applicability of this approach has been in question since in reality there are high volume fractions of elastically anisotropic precipitates with overlapping strain fields and creep and/or misfit dislocations present.

An alternate explanation for the directional coarsening process has been offered by Carry and Strudel [33]. They propose that edge dislocations deposited on the interfaces during the early stages of creep aggravate the misfit on faces of the precipitates parallel to the applied stress, and relieve the misfit on the faces normal to the applied stress. This causes a supersaturation of Ta, Al in the vertical matrix channels, which then leads to a net flow of material toward the horizontal matrix channels, where there is an increased tendency for growth of the normal faces. While there is not any experimental evidence to support this model, it is interesting in that it addresses the potentially important role of the dislocations present during the rafting process, and the possibility of bulk flow of material.

Chapter Two

EXPERIMENTAL MATERIALS AND PROCEDURES

2.1 Nickel Base Single Crystal Material

The superalloy single crystals used in this experimental program were all grown in the < 001 > orientation. The material was donated by the Allison Gas Turbine Division of General Motors. The single crystals were in rod form, 5/8" in diameter by approximately 7" in length. They were received in solution treated form, and were all cast from a single heat of material. All of the bars were within 7° of the < 001 > orientation.

The single crystal alloy is identified as CMSX-3, which is a single crystal derivative of Mar-M-247 developed by the Cannon-Muskegon Corporation. The composition of CMSX-3 is listed in Table 2.1. The compositions of the individual phases as determined by phase extraction [10] are listed in Tables 2.2 and 2.3.

Figure 2.1 shows the microstructure of the bars in the solution treated form. The section transverse to the growth direction, Figure 2.1(a), shows evidence of the dendritic growth process. Since the dendrites grow along < 100 > directions, the bars can be easily aligned along these directions visually. In the interdendritic areas there are networks of darkly etched "lines", as indicated by the arrows in Figure 2.1. These lines are associated with irregularly shaped γ' particles, which are just visible optically at 1000X. In Figure 2.1(b) it is clear that there is also some degree of microporosity in the microstructure. The volume fraction of these micropores is very low (<0.5%),

and they also are associated with the interdendritic areas.

The final microstructure is produced by a series of heat treatments in which the irregular gamma prime present following the casting process is solutioned and re-precipitated as regularly distributed cuboidal particles. The solution and aging treatments, all done in vacuum, are as follows:

Solution Treatment

- 1293°C - 2 hrs. + 1298°C - 3 hrs.
- gas fan cool

Aging Treatment

- 1080°C - 4 hrs.
- furnace cool below 600°C in less than 2 minutes.
- 870°C - 20 hrs.
- furnace cool

2.2 Creep Specimens and Creep Testing

Creep test specimens were machined from the single crystals by Metcut Research Associates, using low stress grinding procedures to prevent recrystallization on the sample surfaces. The buttonhead specimens were $2\frac{7}{16}$" in length. The cylindrical gauge section was 1.5" in length and 0.140" in diameter. Some samples were further ground down to have square gauge sections by removing 0.001" per pass, resulting in 0.100" square cross sections with {100} faces. The samples were hand polished with 600 grit paper and 30μm diamond paste and then electropolished in 20% sulfuric acid and methanol prior to testing.

Testing was done in a lever loading creep machine which was equipped with a Centorr vacuum furnace. Using appropriately designed springs, the creep machine can be used as a constant stress or a constant load machine, but since very small strains were the usual case in this experimental program, testing was done with constant loads. The vacuum was maintained at pressures better than $2x10^{-6}$ torr. Loads were applied smoothly by initially supporting them with a hydraulic jack, and then slowly lowering the jack until the load was fully applied, in a time period of about 15 seconds.

The furnace was equipped with tungsten heating elements, and temperatures were monitored with thermocouples welded to the surface of the samples. The samples were mounted in slotted TZM grips. The grips were water cooled, and this leads to a temperature gradient of 5°C along the specimen. To prevent thermal transients in the grips following the application of the loads, stainless steel washers were used to improve the contact between the loading rods and grips.

Strains were measured by four LVDTs mounted on a plate attached to the loading rod just outside the furnace. This is necessary due to the limited space inside the vacuum furnace. In this configuration, the LVDTs are approximately four inches away from the specimen. To be certain that no spurious strains were being measured, a sample which was identical to the test specimens, except with no reduction at the gauge section, was loaded under the usual test conditions. Applying loads in the range of 65 - 100 lbs. in the temperature range of 800 - 1000°C (the ranges used in the creep tests), and holding for extended periods of time produced no deflections except for elastic extension and extension of the load train during the initial loading process. LVDTs with two different sensitivities were used, with scale factors of 52 V/in. and 208 V/in. Strain resolution of $3x10^{-5}$ was possible with this system.

2.3 Stress - Strain Tests

The stress - strain tests were done in compression using an Instron Model 1350 servo-hydraulic machine. Use of a logarithmic function generator allowed a constant true strain rate to be maintained, and also permitted a strain rate change at a pre-determined level of strain. The Instron machine was equipped with a Research Inc. radiant heating furnace.

Cylindrical specimens 0.200" in diameter were made by centerless grinding of a 5/8" bar to this diameter. The bar was then sliced into pieces which were ground flat and parallel to a final length of 0.300". A 4:1 mixture of 1990 glass and boron nitride powder was used for lubrication between the specimens and the TZM platens. Tests were conducted at a constant rate of 1.4×10^{-4}/s and strain rate jump tests started with this strain rate and jumped to 1.0×10^{-3}/s and 1.0×10^{-2}/s, respectively. Following testing the samples were unloaded and quenched in water within 3 seconds of unloading.

2.4 Transmission Electron Microscopy

Foils for microscopy were prepared by initially cutting 0.015" - 0.020" slices from test bars using a Buehler Isomet low speed diamond saw. An Isomet type blade 0.012" in thickness was used. These slices were then polished to 0.007" using 600 grit paper. Following this they were reduced to 0.005" using 1μm diamond paste. Circular 2.3mm or 3.0mm diameter disks were punched from the polished material. The samples were then thinned electrolytically using a Fischione twin jet polish unit. A solution of 10% perchloric acid, 9% distilled water, 13% buthyl cellusolve, and 68% methanol was used under conditions of -30°C, 10V, and a current of 20ma. Thinning typically required approximately 5 minutes, and since the γ' precipitate diameter was on the order of the desired foil thickness, the yield of useful specimens was usually fairly low.

Two different microscopes were used in the course of these investigations; a Phillips

EM 300 at an accelerating voltage of 100kV, and a JEOL 200CX at 200kV. Stereo imaging required the use of double tilting holders, and when 2.3mm samples were imaged, they were sandwiched between copper grids.

Stereo pairs were obtained by maintaining a two beam condition (constant g and s) and tilting 10 - 20° (depending on the magnification) with the aid of Kikuchi lines. Nearly all of the stereo pairs were made with photographs taken on opposite sides of the $< 001 >$ zone axis. Pictures were printed with the film emulsion side up. To view the images as if looking down on the specimen as it was oriented in the column, the pictures should be oriented with the tilt axis vertical and the g vectors pointing away from the center of the stereo pair.

In-situ annealing observations were made with the use of a Gatan single tilt heating stage, with a maximum temperature capability of 1300°C. Samples were held between Ti or Ta grids to prevent welding to the furnace, which also serves as the specimen holder. Since the thermocouple is welded to the outside of the furnace, it was necessary to calibrate the heating stage for a more accurate estimate of the actual temperature of the foil. Samples of Al in a carbon coated Cu grid, Ge in a Ti grid, and Ag in a Ni grid were melted to compare their melting points with the temperature registered by the furnace thermocouple. The specimen/grid combinations were chosen to avoid interdiffusion between the grids and samples at high temperatures. The melting points Al, Ge, and Ag are 660°C, 937°C, and 960°C, respectively. A comparison between actual melting temperature and the temperature measured by the heating stage thermocouple is shown in Figure 2.2.

Measurement of changes of dislocation density during the *in-situ* annealing experiments were made by selecting an area for observation and recording a series of micrographs of the same area over a period of time. To calculate the total dislocation

density, an image analyzer program which records lines in a micrograph, reduces them to a single pixel in width, and then gives a measurement of total line length was used. Foil thickness was estimated from a stereo pair using the cube edges of the precipitates as a reference for measurement. The densities were then corrected to account for the dislocations that were invisible under the given diffraction conditions.

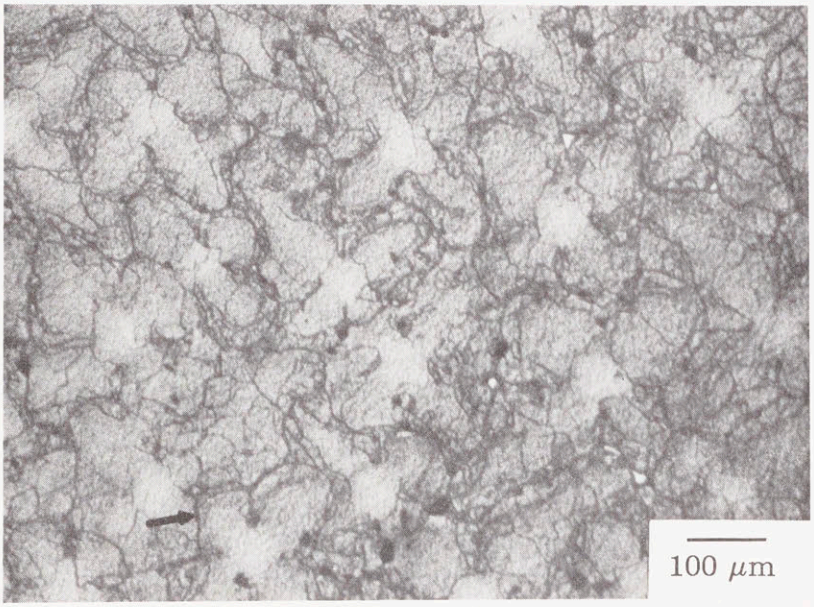

(a)

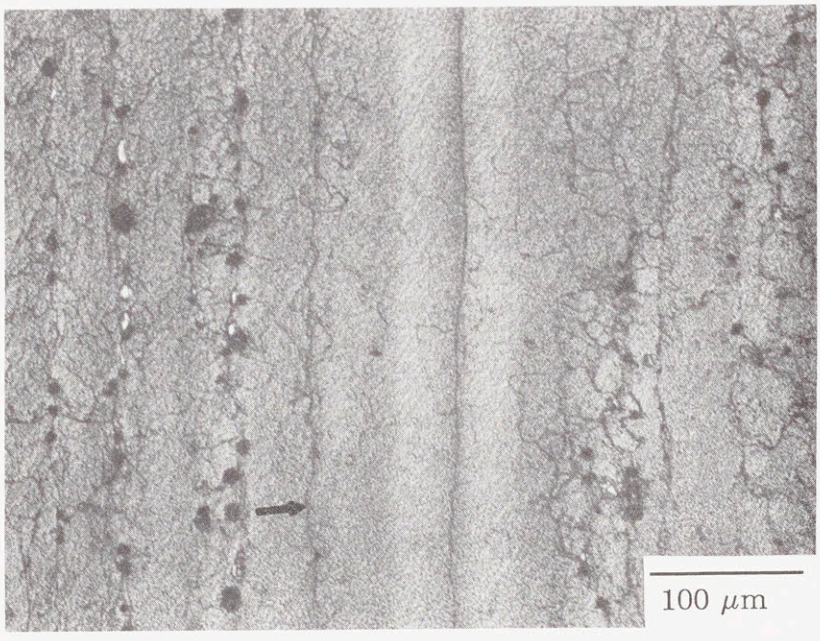

(b)

Figure 2.1 (a) Low magnification micrograph of CMSX-3 solution treated bar. Section transverse to the growth direction.
(b) Longitudinal section of CMSX-3 solution treated bar.

Table 2.1 Nominal chemical composition of CMSX-3

Element	Weight percent	Atomic percent
Cr	7.9	9.1
Co	4.6	4.7
Mo	0.5	0.3
W	8.0	2.6
Ti	1.0	1.1
Al	5.6	12.4
Ta	6.0	1.9
Hf	0.11	0.03
Ni	Bal.	Bal

Table 2.2 Chemical composition of the matrix phase in CMSX-2 (10).

Element -	Weight percent	Atomic percent
Cr	18.8	21.6
Co	7.3	7.4
Mo	0.9	0.5
W	9.4	3.0
Ti	0.4	0.5
Al	2.0	4.4
Ta	0.1	0.04
Ni	61.1	62.4

Table 2.3 Chemical composition of the γ' in CMSX-2 (10).

Element	Weight percent	Atomic percent
Cr	2.0	2.3
Co	3.2	3.2
Mo	0.3	0.2
W	7.3	2.3
Ti	1.3	1.6
Al	7.6	16.7
Ta	9.2	3.1
Ni	69.0	71.1

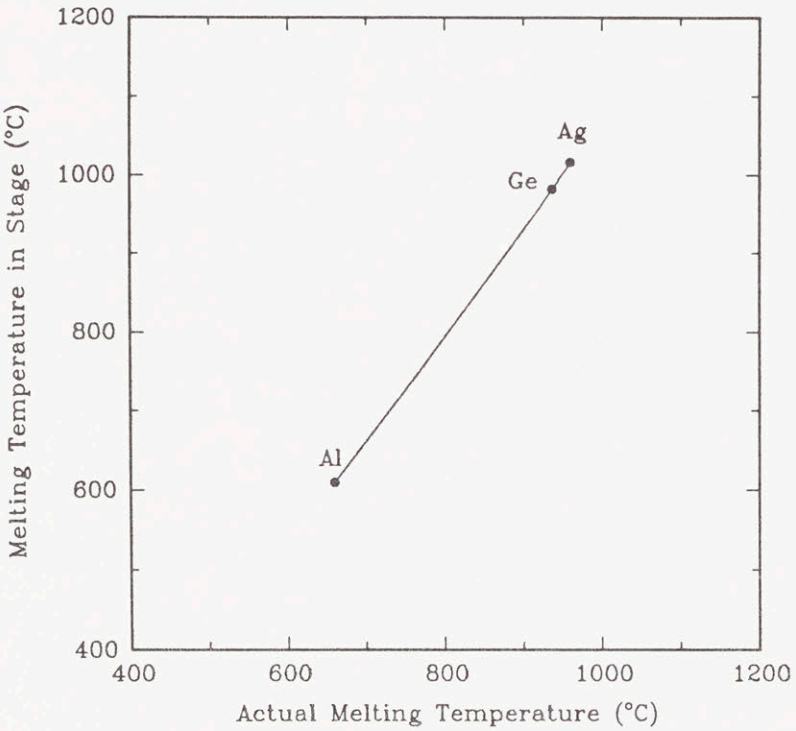

Figure 2.2 Heating stage temperature calibration.

Chapter Three

MECHANICAL TESTS

3.1 Steady Creep Experiments

To establish creep stress exponents and activation energies, creep tests covering the temperature range of 800°C - 900°C and stress range of 450 MPa - 650 MPa were completed. Table I lists the testing conditions and summarizes the results covered by this experimental program. Under the conditions covered here, the creep curves show a brief primary transient resulting in less than 0.5% strain, followed by a period of minimum creep rate (which will for convenience be referred to as "steady state" creep), and a rather extended period of slowly accelerating tertiary creep. Figure 3.1 shows a representative curve at 850°C and 552 MPa, where the test was run to fracture. In general the tests were not run to completion; once the steady state creep rate was established, the tests were interrupted for the purpose of preserving the samples for microscopy. Additional creep curves are shown in Appendix B. From the data in Table 3.1 in this limited temperature and stress range, a creep stress exponent, $n=\partial ln\dot{\varepsilon}_{ss}/\partial ln\sigma$ can be calculated and is equal to 7.1. As can be seen in Figure 3.2, the modulus compensated activation energy is 495 kJ/mole, which is rather high compared to the activation energy for self diffusion in nickel, which is 280 kJ/mole. These values are similar to those reported for other nickel base single crystals.

Figure 3.3 shows the early stages of the creep curves at 552 MPa at the temperatures of 800°C, 850°C, and 900°C. (Note that there is a different time scale for the 800°C data.) There is no instantaneous plastic straining upon application of the load;

only extension of the load train and elastic strains are recorded. Close inspection of the curves shows incubation periods prior to the onset of the primary transient at 800°C and 850°C. At 800°C the incubation period lasts for $1.6x10^4$ seconds, while at 850°C the incubation is only about 600 seconds in length, and at 900°C it is apparently immeasurably short. For a constant stress the incubation periods increase in length with decreasing temperature, and similarly, for a constant temperature a lower stress will lead to a longer incubation time, with a time of 4500 seconds for 850°C - 450 MPa. From this data an activation energy of 658 kJ/mole can be calculated for the incubation period. However, since only a limited number of tests have been completed here and incubation period was not exactly reproducible from sample to sample at 850°C, these reported incubation times and activation energy may not be completely representative of the process.

3.2 Non-Steady Creep Experiments

To determine the effect of static recovery on the mechanical response of the material in the creep regime, a sample was loaded and allowed to creep until the steady state creep rate was established at 850°C - 552 MPa. At this point the sample was unloaded by 90% and permitted to rest at 850°C for varying amounts of time. The sample was then reloaded for observation of the reloading transients. Successive rest periods of 180, $1.8x10^3$, $1.62x10^4$, and $1.62x10^5$ seconds all gave similar results with respect to the reloading transient. In Figure 3.4 the results for the sample annealed for $1.62x10^4$ seconds (4.5 hours) are plotted, showing the reloading transients to be very slight, resulting in less than 10% of the strain accumulated during the primary transient.

Stress jump and drop tests were conducted at 850°C on a sample which was initially creeping at a steady rate at 552 MPa. Starting with 0.87% accumulated creep strain Figures 3.5 and 3.6 show the results of a stress jump from 552 to 605 MPa and the

following drop from 605 MPa back to 552 MPa. Upon increasing the load, there is an instantaneous elastic extension giving a strain of 6.1×10^{-4}. This extension is very close to the expected elastic extension calculated by using the dynamic modulus for the $< 001 >$ orientation in DS Mar-M-247. It is also exactly equal to the contraction upon removing the 50 MPa load. Following the elastic extension there is a brief transient and a new steady state creep rate is quickly established. Using the new steady state creep rate, a steady state creep exponent of n=7.3 is obtained. Unloading back to 552 MPa, the original creep rate at 552 MPa is reestablished. Figures 3.7 and 3.8 show the transients immediately after the load changes in more detail. As can be seen in Figure 3.7, following the stress jump there is a transient which lasts only about 300 seconds before the new rate of deformation is established. Using the rate of deformation immediately following the application of the extra load, an instantaneous stress exponent of n=28.3 can be calculated for the transient process. When dropping from 605 to 552 MPa, there is a period of zero creep which lasts for 535 seconds, as shown in Figure 3.8. Again, these transients are brief compared to the primary transient, as shown by Figure 3.9, where the creep rates normalized by the steady state creep rates are shown as a function of time.

3.3 Stress-Strain Experiments

In order to probe the material behavior under different loading conditions, constant true strain rate and strain rate jump experiments were performed. The results for compression of a sample at a constant rate of 1.4×10^{-4}/sec. at 800°C are shown in Figure 3.10. At this imposed rate, the 0.2% yield strength is 950 MPa, which is approximately twice the magnitude of the stresses imposed during the creep tests. Note also that the flow stress continues to rise during the test.

Figure 3.11 presents the results for a strain rate jump to 1×10^{-3}/sec. after approx-

imately 2% deformation at $1.4x10^{-4}$/sec. From this a stress exponent can again be calculated and is n=36.2, which is very high compared to the steady state creep exponent of 7.1, but in the same range as the exponent calculated from the instantaneous rate of deformation following the stress jump during creep. The slight downward decay in the stress level following the strain rate jump cannot definitely be attributed to softening since the motion of the actuator at these slow rates is not always completely smooth. For a strain rate jump from $1.4x10^{-4}$ to $1x10^{-2}$/sec. the stress exponent is n=38.7.

Table 3.1 Experimental test conditions and results for creep in CMSX-3 single crystals.

Temperature (°C)	Stress (MPa)	Total Strain	Minimum Creep Rate (s^{-1})	Sample ID
850	552	.147	$2.5x10^{-8}$	R13-2
850	552	.0073	$2.4x10^{-8}$	AF12-1
870	625	.0566	$1.8x10^{-7}$	C101-4
870	500	.022	$3.6x10^{-8}$	AM13-2
800	552	.0078	$2.6x10^{-9}$	AD13-1
900	552	.107	$3.0x10^{-7}$	AM13-1
850	450	.012	$5.9x10^{-9}$	A100-3
850	650	.046	$3.4x10^{-7}$	L101-10

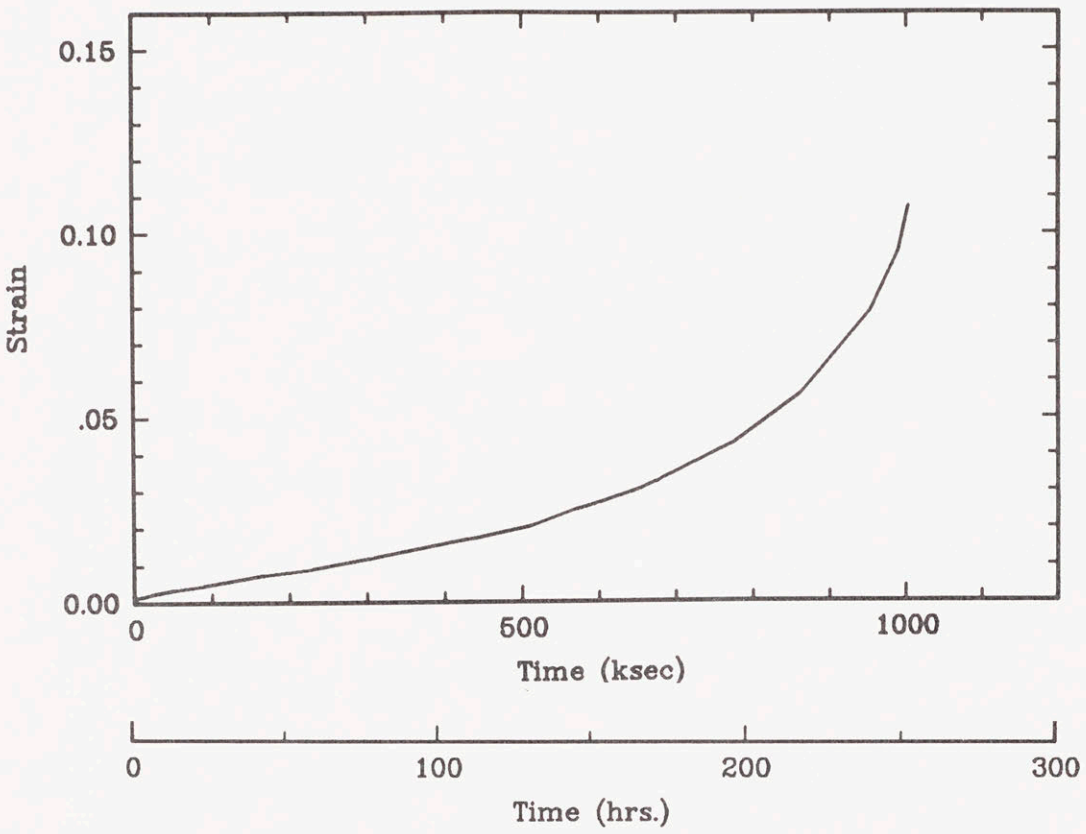

Figure 3.1 Full creep curve for $< 001 >$ CMSX-3 at 850°C and 552 MPa. Fracture occurred at 273 hours.

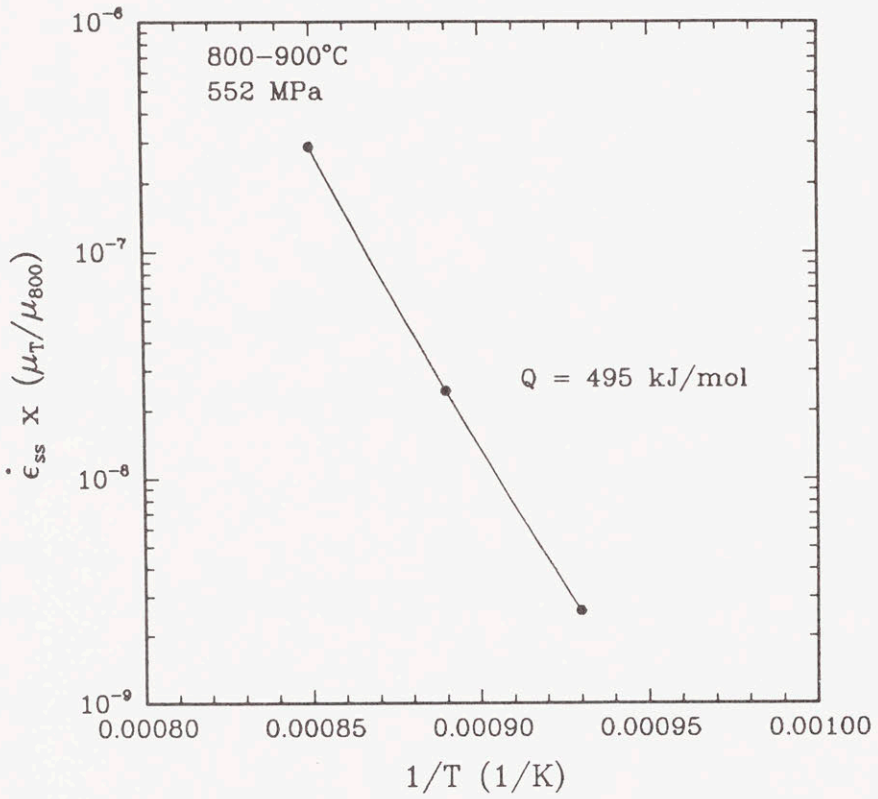

Figure 3.2 Activation energy for creep in CMSX-3 at 552 MPa.

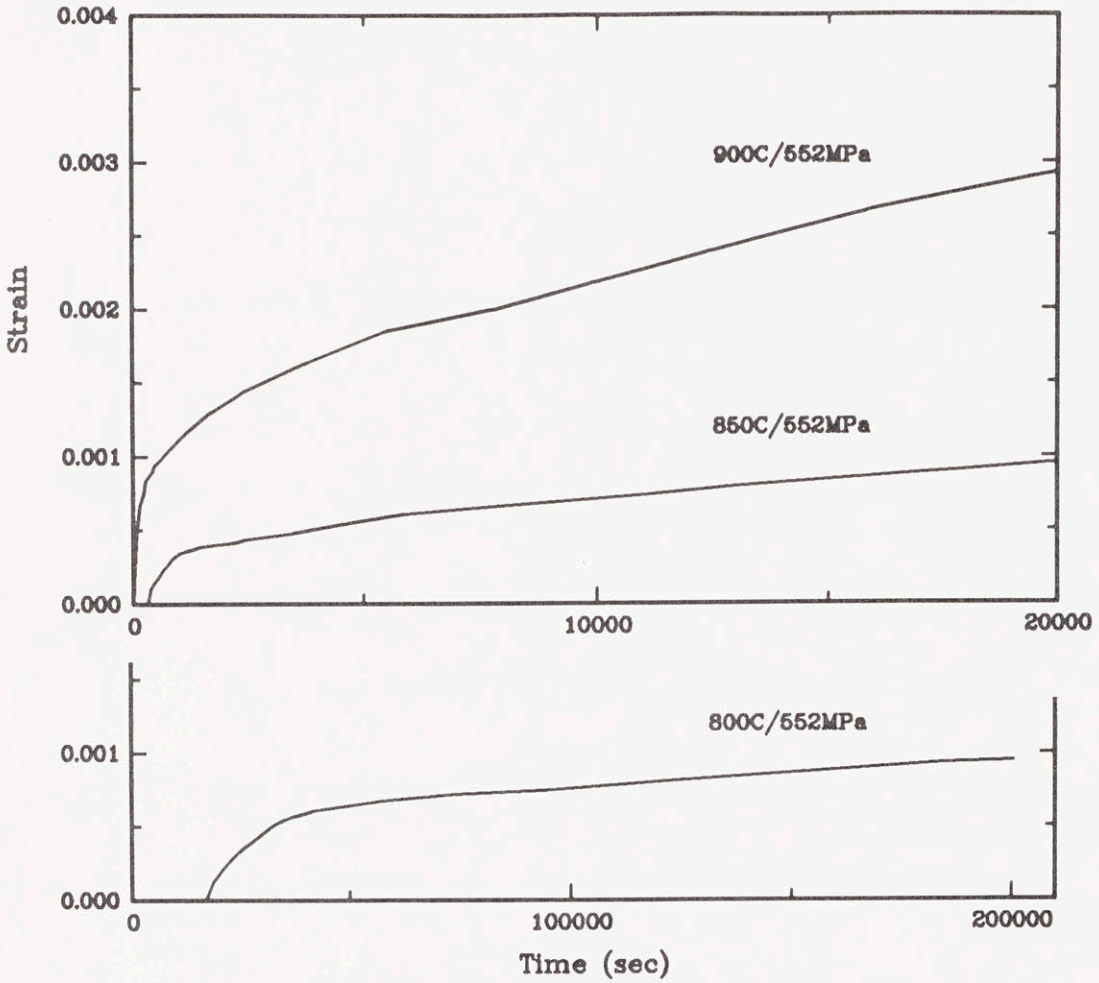

Figure 3.3 Small strain creep behavior of CMSX-3. Note the change in time scale for the 800°C data.

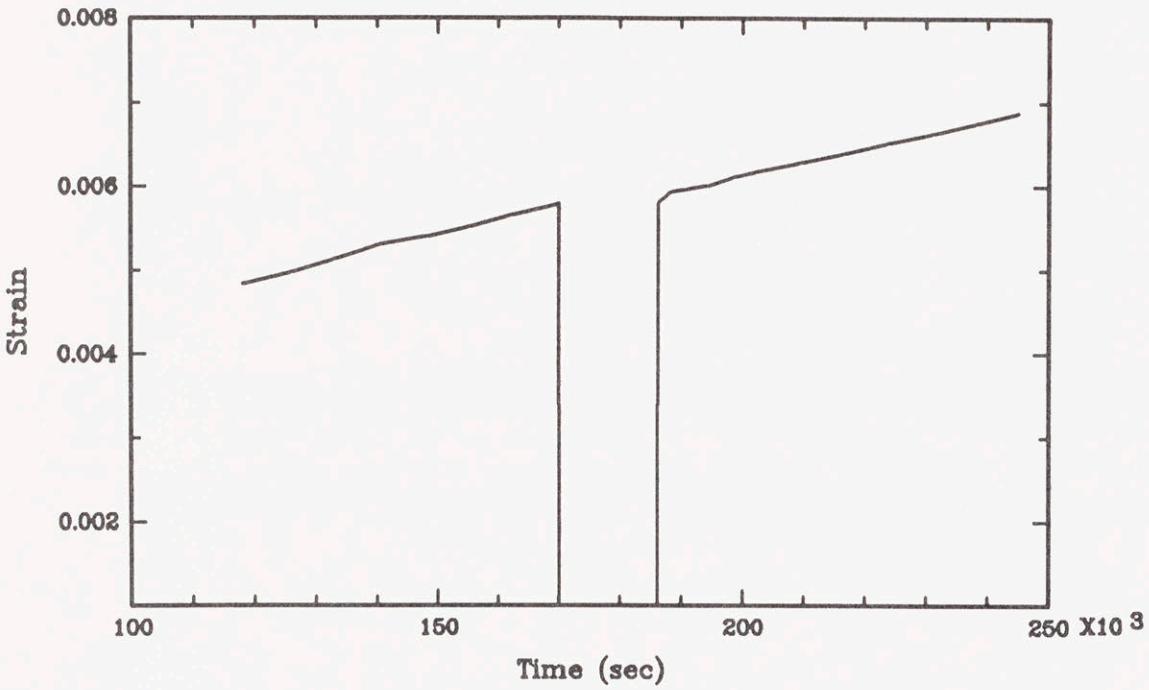

Figure 3.4 Reloading transient following a 90% load reduction during steady state creep.

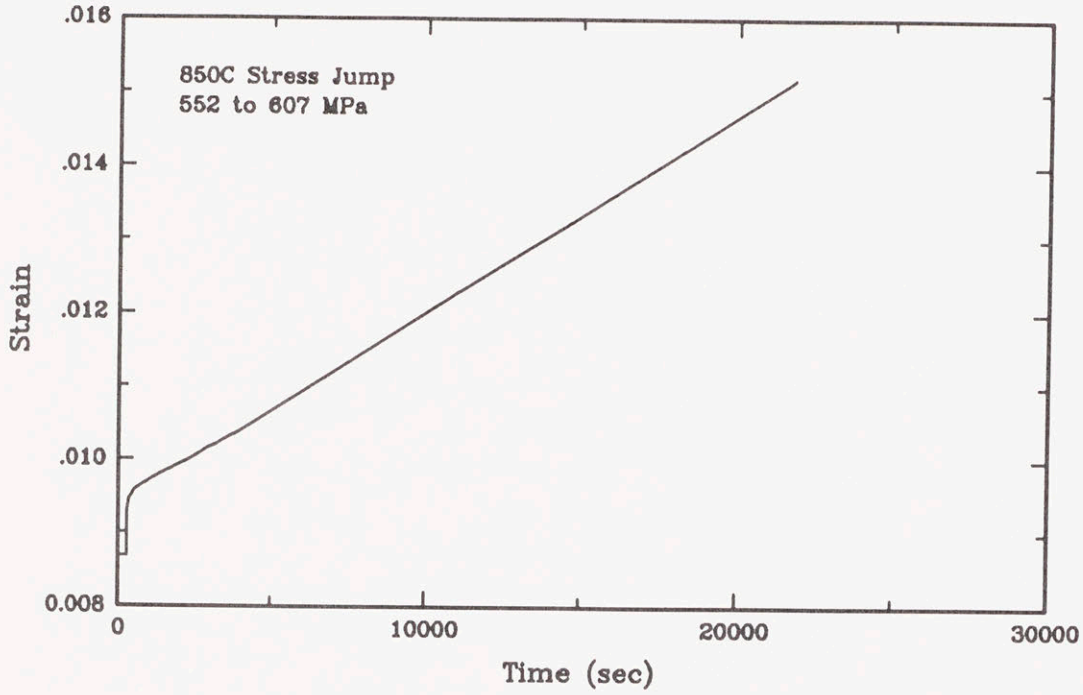

Figure 3.5 Stress jump during steady state creep from 552 to 607 MPa.

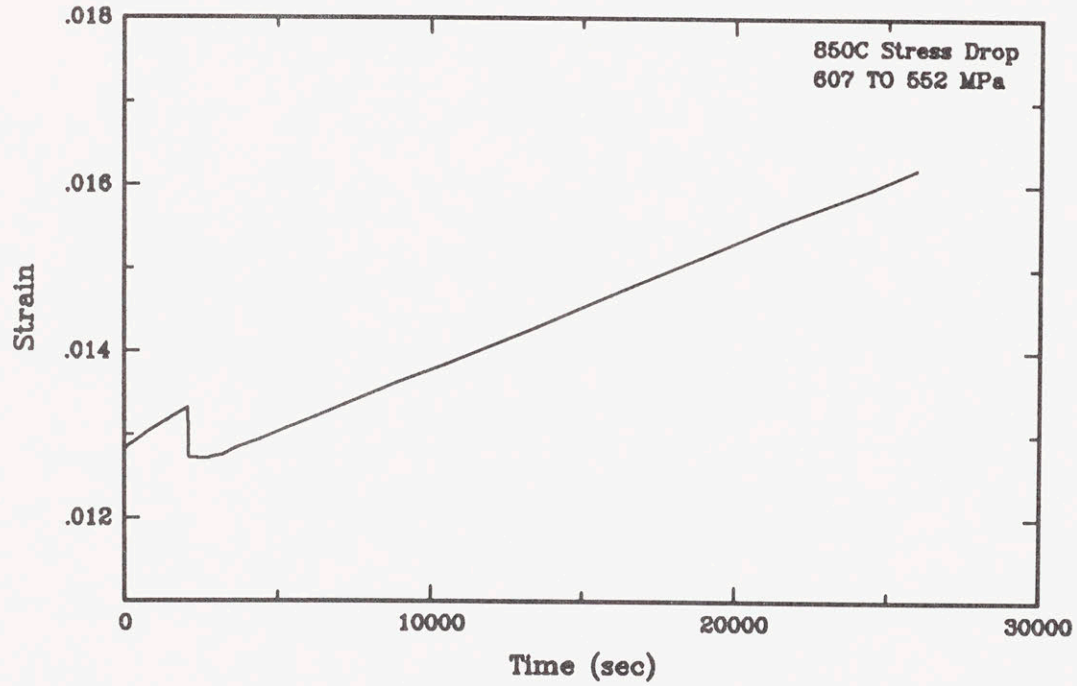

Figure 3.6 Stress drop from 607 MPa back to the original 552 MPa.

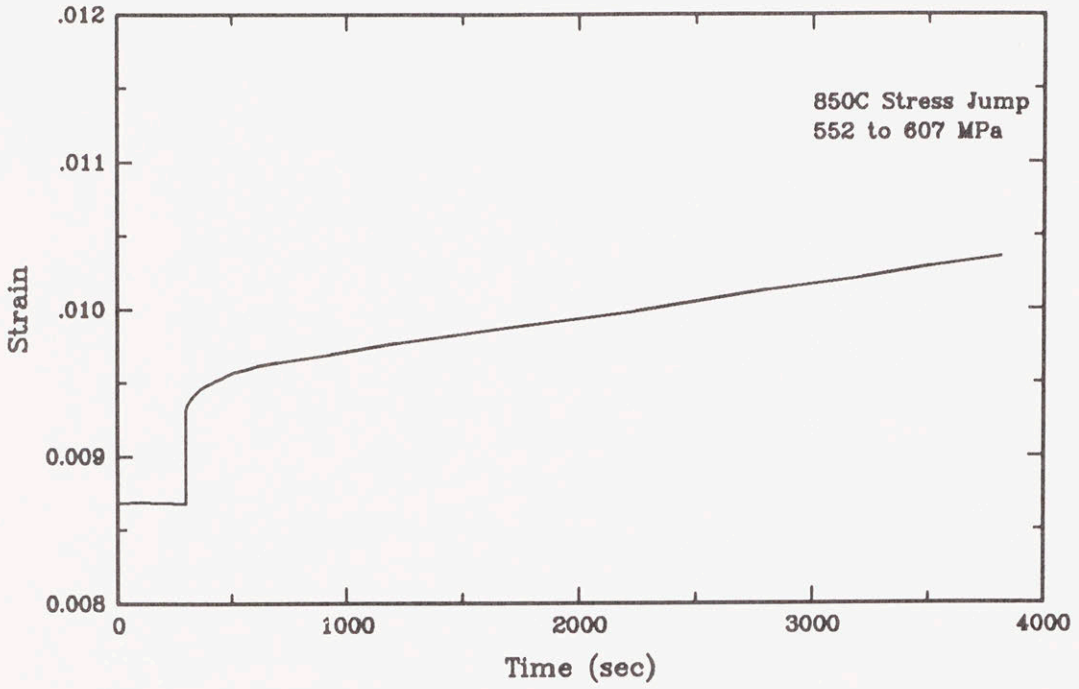

Figure 3.7 Transient behavior immediately following the stress jump from 552 to 607 MPa.

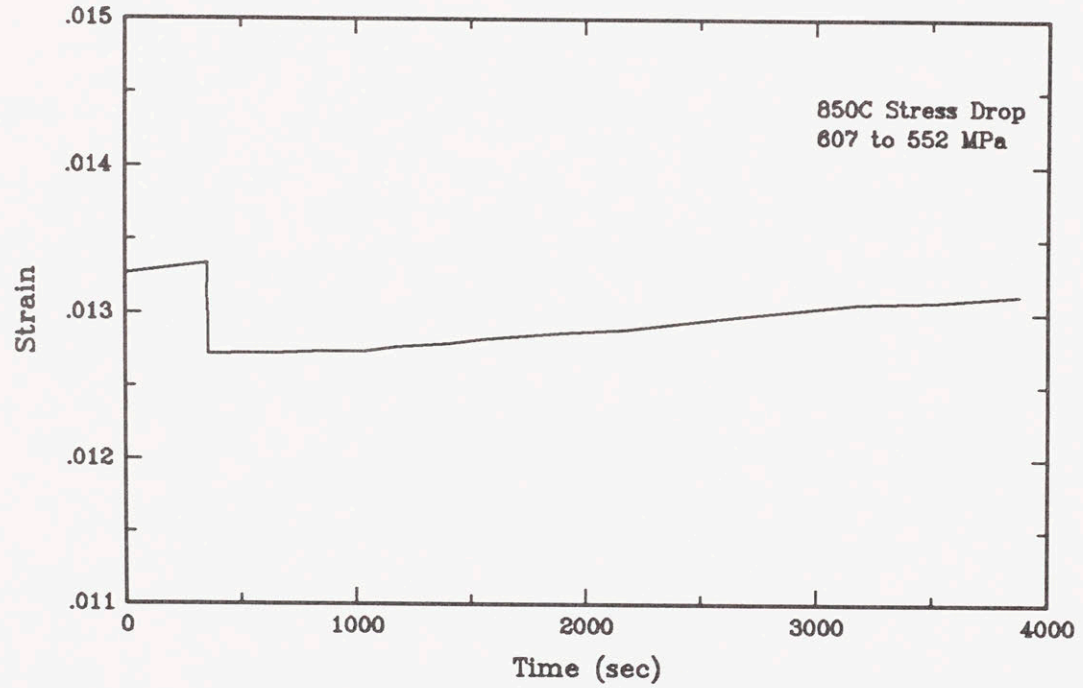

Figure 3.8 Recovery period following the stress drop from 607 MPa back to the original 552 MPa.

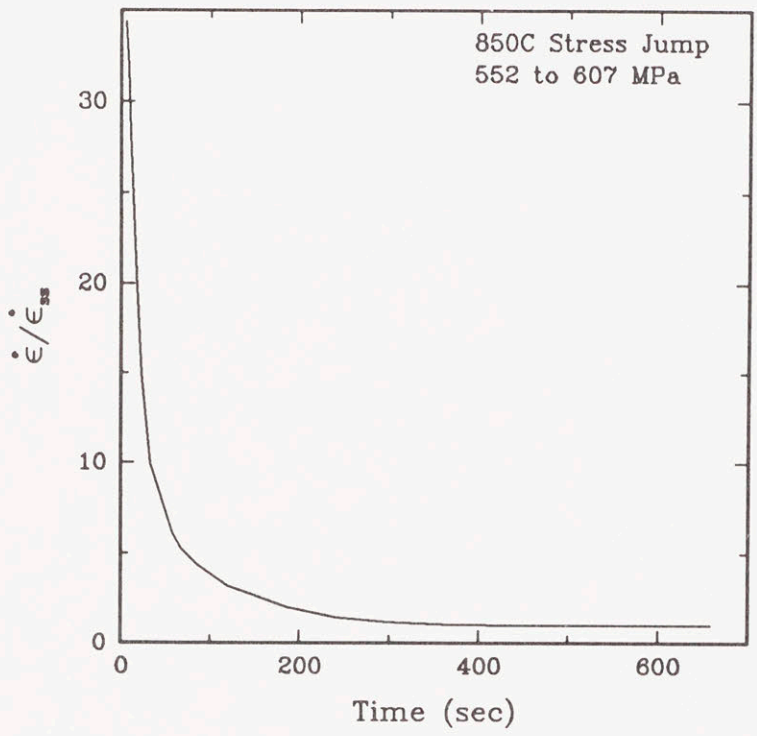

(a)

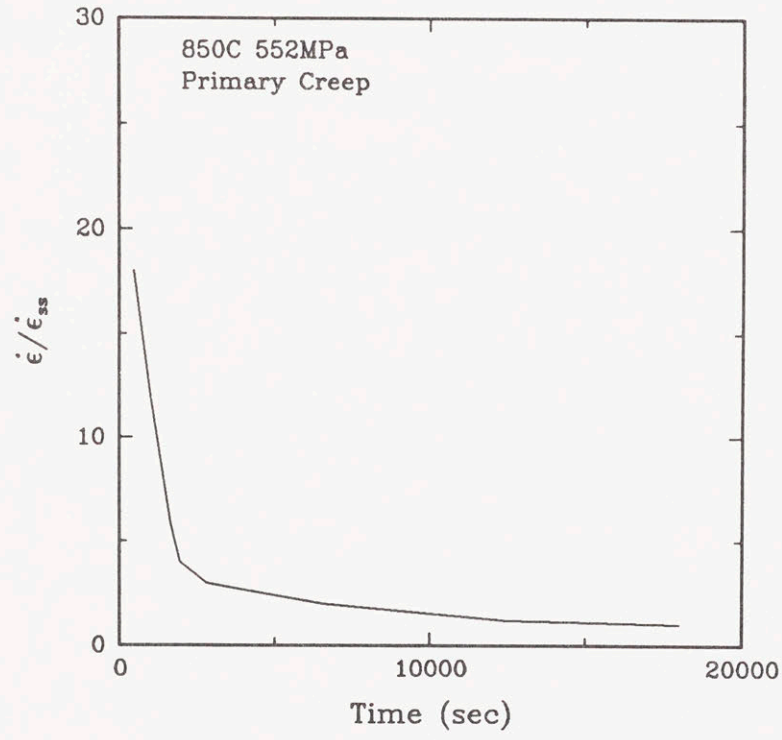

(b)

Figure 3.9 Comparison of the transients for the 552 to 607 MPa stress jump (a), and primary creep at 552 MPa (b).

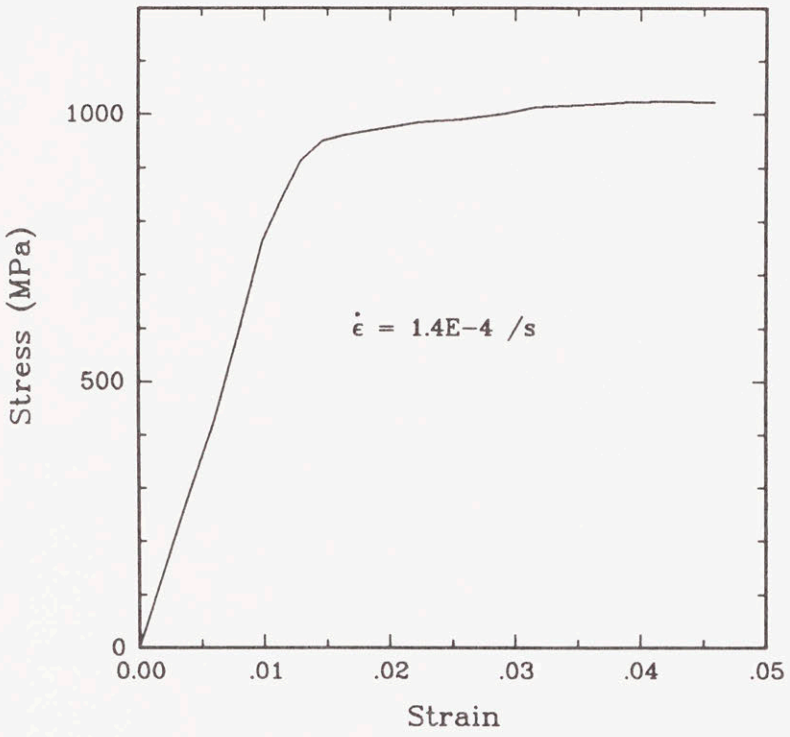

Figure 3.10 Constant true strain rate compression test at 800°C.

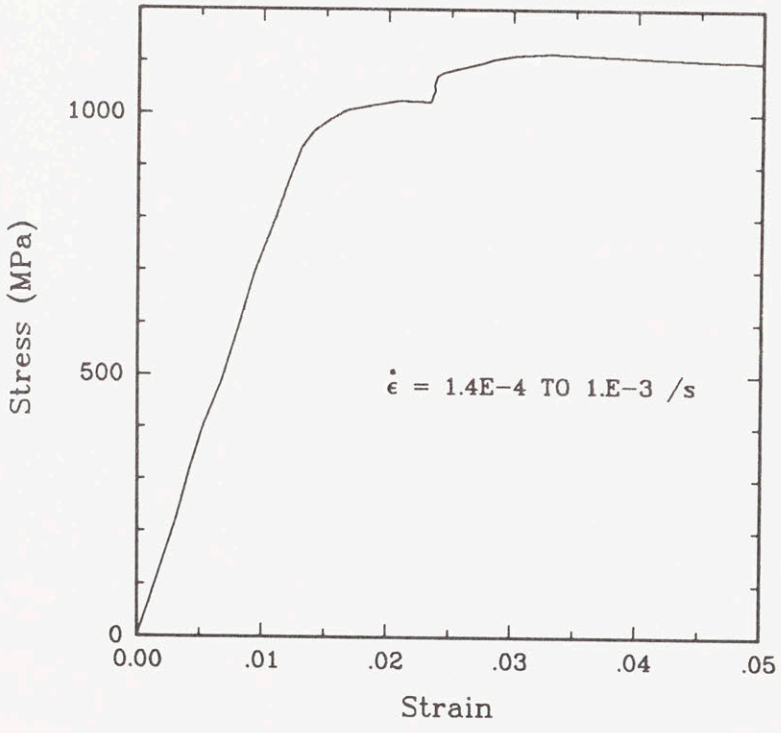

Figure 3.11 Compression strain rate jump test at 800°C.

Chapter Four

TEM OBSERVATIONS

In this chapter, observations of dislocation structures in the aged material as well as arrangements during the incubation period, primary creep transient, and steady state creep will be discussed. The results of *in-situ* annealing experiments will also be presented.

Since stereo-imaging techniques were used, three dimensional arrangements of the dislocations will be described. The spatial arrangement of the dislocations is key in understanding the creep processes in this two phase material, and important in providing information which is needed for modeling of the creep processes.

All TEM foils were taken from creep specimens which were cooled under load to preserve the arrangements. No rearrangements of the dislocations were ever noted during the ambient temperature observations. Due to the cuboidal nature of the precipitates the foil thicknesses could be estimated from the stereo pairs. Foils were typically 0.4-0.6μm in thickness, containing through the thickness either one precipitate surrounded by two layers of matrix material, two precipitates with a single layer of matrix in between, or occasionally a single precipitate extending through the entire thickness of the foil.

4.1 The Aged Material

The aging heat treatment produces cube shaped γ' precipitates which on average have a cube edge length of 0.45μm. The matrix passage thicknesses are an average of 60 nm, giving a volume fraction of γ' of 0.68. The precipitates are coherent with the

matrix, with only an occasional dislocation seen at the matrix/precipitate interface, as shown in Figure 4.1. No coherency strain contrast is seen in the aged material, and this is probably due to the fact that the misfit at room temperature is very low. Also, the matrix passages are very narrow giving overlapping strain fields, which would give contrast which is different than that observed for widely spaced γ' precipitates [74].

The micrograph in Figure 4.1 is representative of the structure over very large areas in the aged material. However, areas of "grown in" dislocations associated with irregularly shaped γ' are occasionally seen in the aged material. One such area is shown in Figure 4.2. These areas are widely spaced and appear to be associated with the darkly etched "lines" noted in Figure 2.1. These networks of grown-in dislocations all lie in the matrix material. The density of the grown-in dislocations is estimated from the micrographs to be about $10^7/cm^2$. No dislocations are observed inside the γ' in the aged material.

4.2 The Incubation period

The following observations were made on samples taken from a specimen which was tested at 825°C/450 MPa, where an incubation period of reasonable length is expected. The test was interrupted and the specimen cooled under load after 2 minutes. No externally measurable strain was accumulated in this time.

Over very large areas the incubation samples resembled the aged samples, showing many coherent cuboidal precipitates with no dislocations present. However, the incubation samples did vary from the aged samples in the regions where the prior "grown-in" dislocations were present. During the incubation period the "grown-in" dislocations serve as sources, and creep dislocations spread from these areas into the clean, coherent areas. In Figure 4.3 the prior dislocations are at the center of the micrograph, and the longer, more straight dislocations are bowing out and spreading

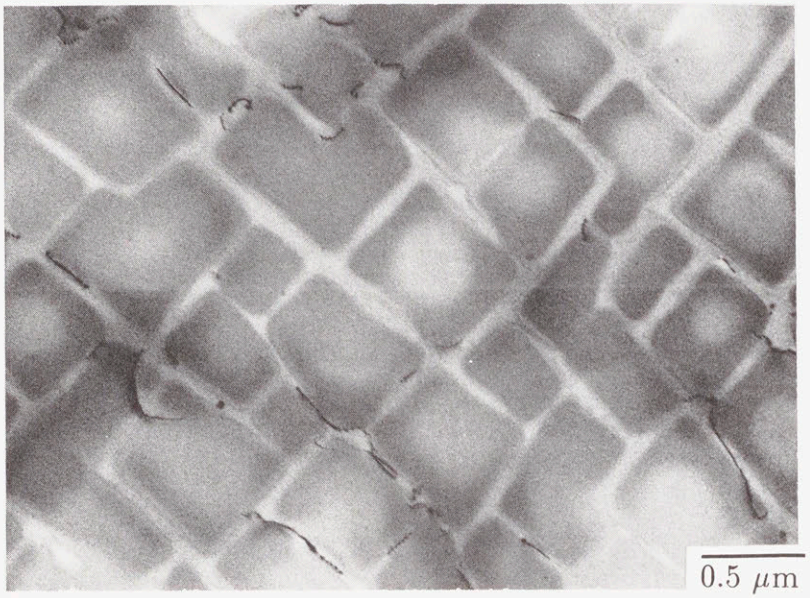

Figure 4.1 TEM micrograph of the γ/γ' structure of the aged single crystal CMSX-3 material.

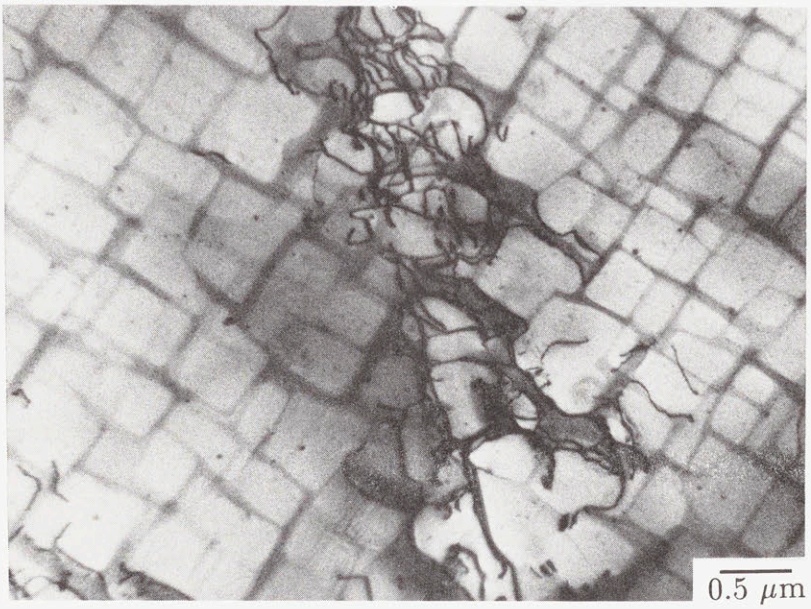

Figure 4.2 Network of "grown-in" dislocations in the aged material.

from the center to the left and right. All of the dislocations are in the matrix, and as a result of their confinement to the narrow matrix passages, the expanding loops assume a very long, narrow shape. In Figure 4.4 dislocations are spreading out from the top left corner. Even in the thin foil, a single loop, such as the one marked "A" in Figure 4.4, may be traced to cross many precipitate diameters. This loop at "A" is contained in a matrix passage parallel to the foil plane. Several leading segments of the bowing out loops, which are pure screw in orientation, are marked in Figures 3.3 and 3.4 by arrows. Stereo pairs show that few of these leading screw segments are held up at the γ/γ' interfaces. Instead they have been captured in the process of slowly moving through the matrix gaps.

A higher magnification view of the bowing dislocations is shown in Figure 4.5. Near the area marked "B" there are several dislocation loops which have taken a 90° change in direction during the process of traveling through the matrix. Stereo pairs show that these dislocations ($\mathbf{b}=a/2[0\bar{1}1]$) have cross slipped from the $(\bar{1}11)$ plane to the (111) plane. In this case the leading screw segments have traveled from "A" to "C", leaving mixed dislocations at the interfaces, and cross-slip has occurred at "B". These cross slip events were frequently observed in the samples, and serve to assist in the systematic spreading of the dislocations into the narrow γ channels. Another mode of dislocation spreading is also obvious in Figure 4.5, as marked by the arrow. As a loop expands through a horizontal matrix gap, multiple vertical matrix gaps will be encountered, and the dislocations also spread into these vertical gaps. At the arrow a dislocation is beginning to expand into the vertical gap, and this is the reason for the periodic wavy segments on the otherwise straight dislocation lines contained in the horizontal matrix channels.

4.3 Primary Creep

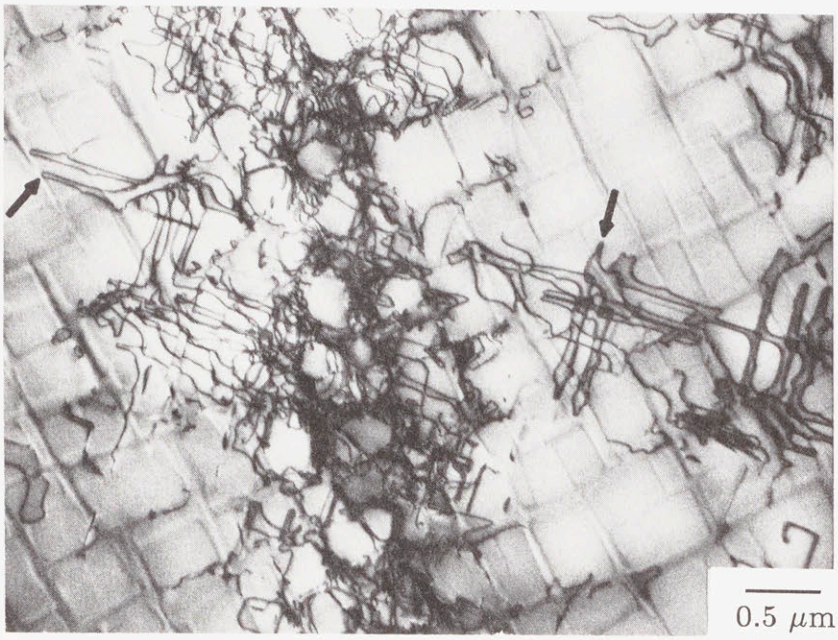

Figure 4.3 Dislocations spreading from the grown-in dislocation network during the incubation period. The network is at the center and the arrows denote the leading screw components of the expanding loops.

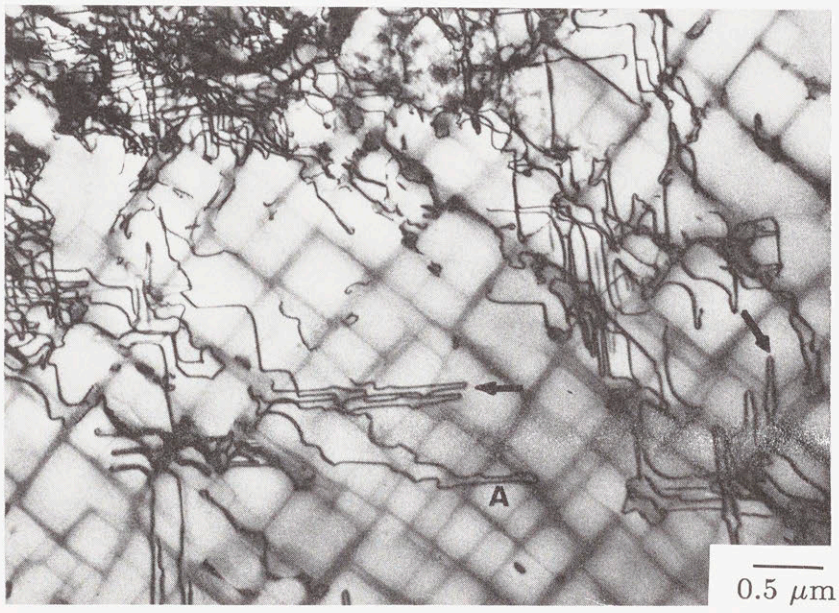

Figure 4.4 Long, narrow dislocation loops spreading through the matrix during the incubation period. These dislocations originated from the network in the upper left corner.

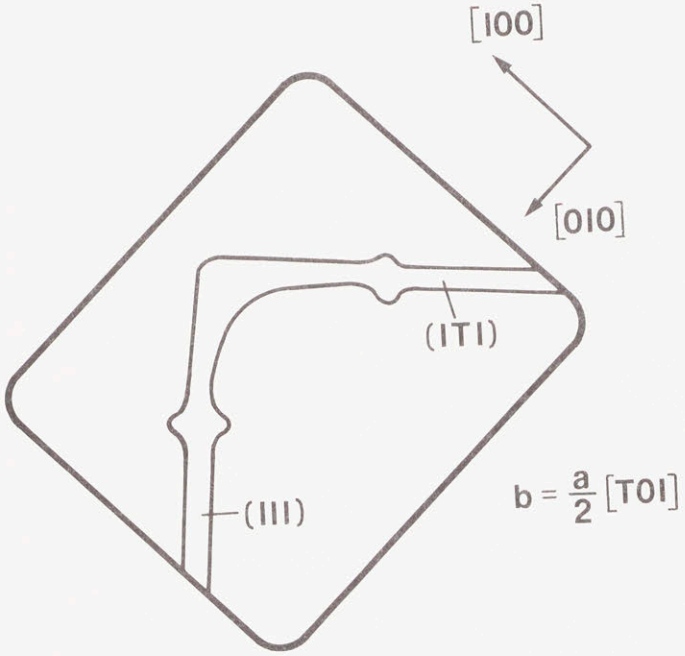

Figure 4.5(a) Schematic of the details of the cross-slipping matrix dislocations corresponding to area (B).

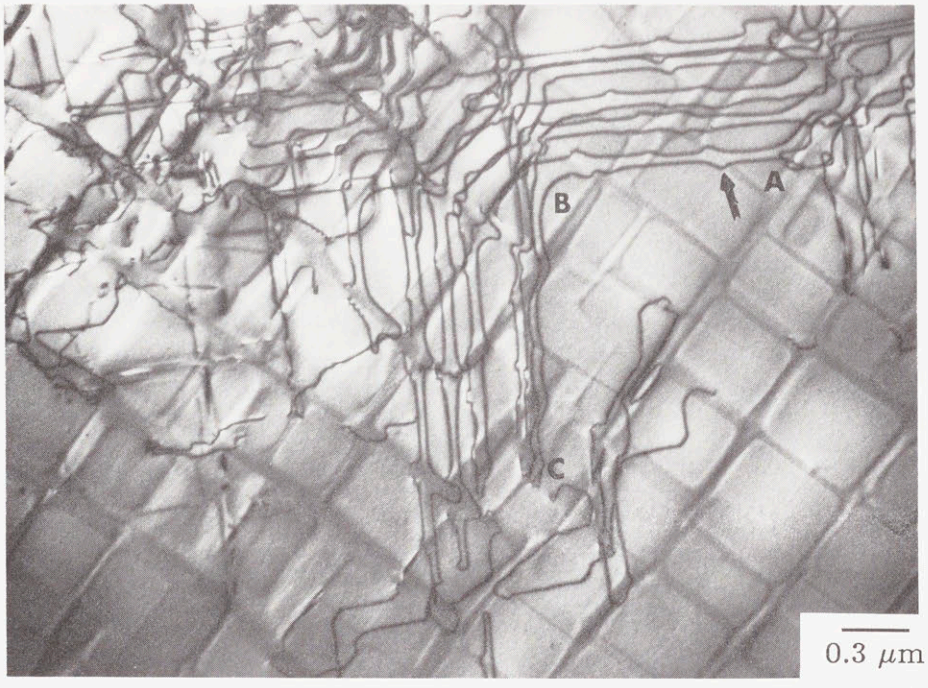

Figure 4.5(b) Cross-slipping matrix dislocations during the incubation period. A bowing out screw segment has progressed from (A) to (C) cross slipping at (B) from the $(1\bar{1}1)$ plane to the (111) plane.

During primary creep the material continues to fill with dislocations. All creep deformation continues to be accomplished by bowing the dislocations through the matrix channels on {111} planes. Figures 4.6 and 4.7 are representative of the dislocation structure after 35 minutes (ϵ=4.6x10^{-4}) and 402 minutes (ϵ=0.001), respectively. In Figure 4.6 nearly all of the dislocations have the same Burgers vector, and many of the matrix passages have not yet filled with dislocations. In comparison, Figure 4.7 shows a higher density of dislocations, with nearly all of the matrix channels containing some dislocations. Close inspection of Figure 4.7 shows that additional dislocations with different Burgers vectors are present locally. These dislocations indicated by the arrow in Figure 4.7 are obvious because of the residual contrast of the non-screw portions of the loops. Figure 4.8 shows this more clearly, where an area is imaged under two different diffraction conditions, showing two sets of dislocations beginning to interpenetrate and react.

Figure 4.9 is a stereo pair of the primary creep structure which clearly demonstrates the characteristic three dimensional arrangement of the dislocations during primary creep. Near the area marked "A" the solid, lighter precipitates extend through the thickness of the foil. In the matrix passage to the left of "A" the dislocations are bowing through the gap vertically, as shown schematically in Figure 4.10(a). Near the area marked "B" in Figure 4.9 the foil contains a matrix passage as well as a precipitate, and the dislocations are bowing horizontally through the gaps as demonstrated in Figure 10(b). Again referring to Figure 4.9, many of the dislocations in the horizontal channel (Area "B", where the channel is normal to the direction of applied stress) are long and straight and lie at an angle of 45 degrees to the cube face. These dislocations are contained in horizontal passages at the γ/γ' interface as a result of loops bowing through the channels on {111} planes. They are mixed in character, with

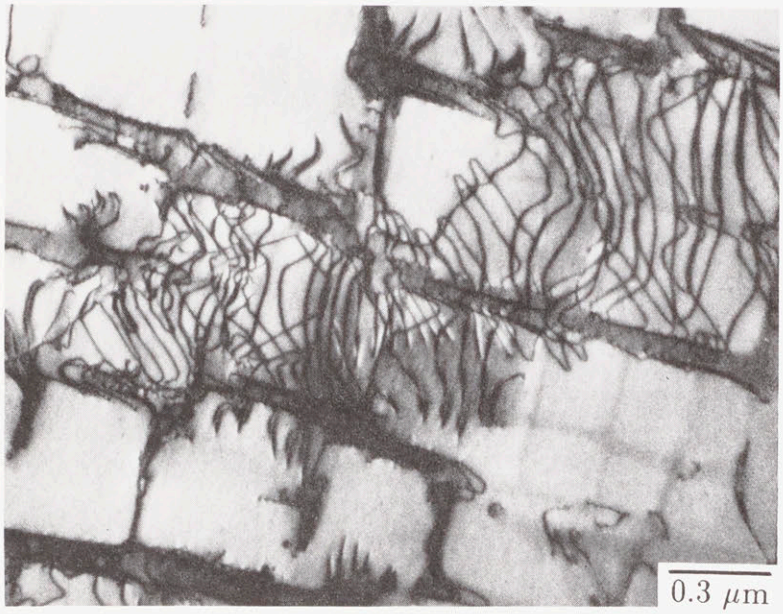

Figure 4.6 Primary creep dislocation structure after 35 minutes of creep, $\varepsilon = 4.6 \times 10^{-4}$. These dislocations all have the same Burgers vector of $\mathbf{b}=a/2\ [011]$.

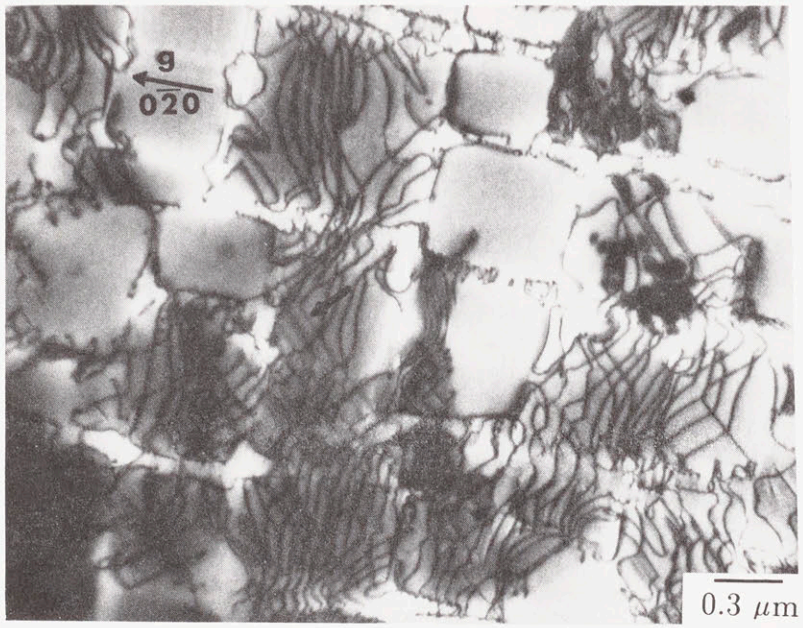

Figure 4.7 Primary creep dislocation distribution after 402 minutes, $\varepsilon = 0.001$. Dislocations with a second Burgers vector are beginning to penetrate locally at the arrow.

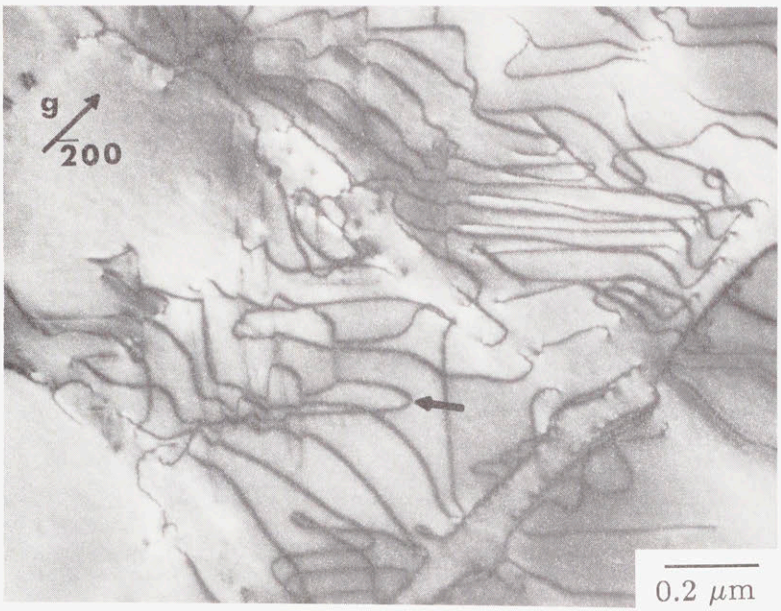

Figure 4.8(a) One of two sets of interpenetrating primary creep dislocations in the matrix material. The arrow marks a common reference point.

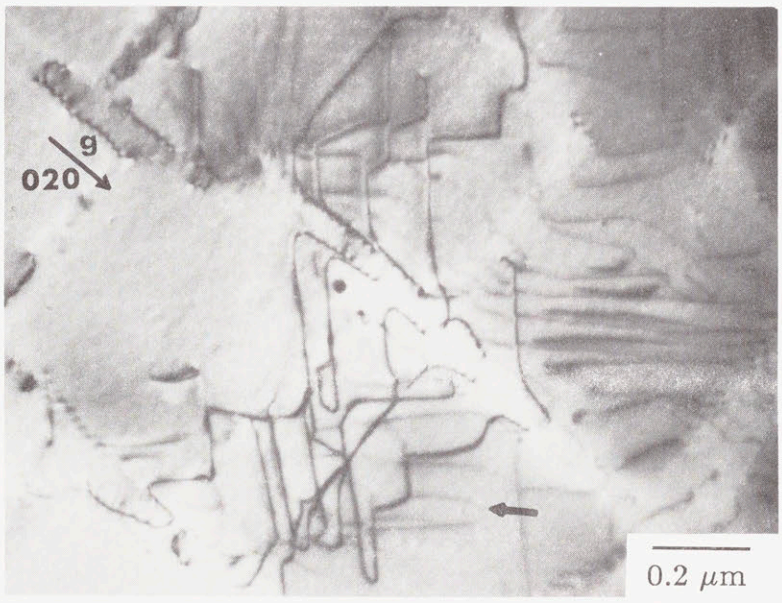

Figure 4.8(b) The second set of the locally interpenetrating dislocations. The arrow marks the common reference point.

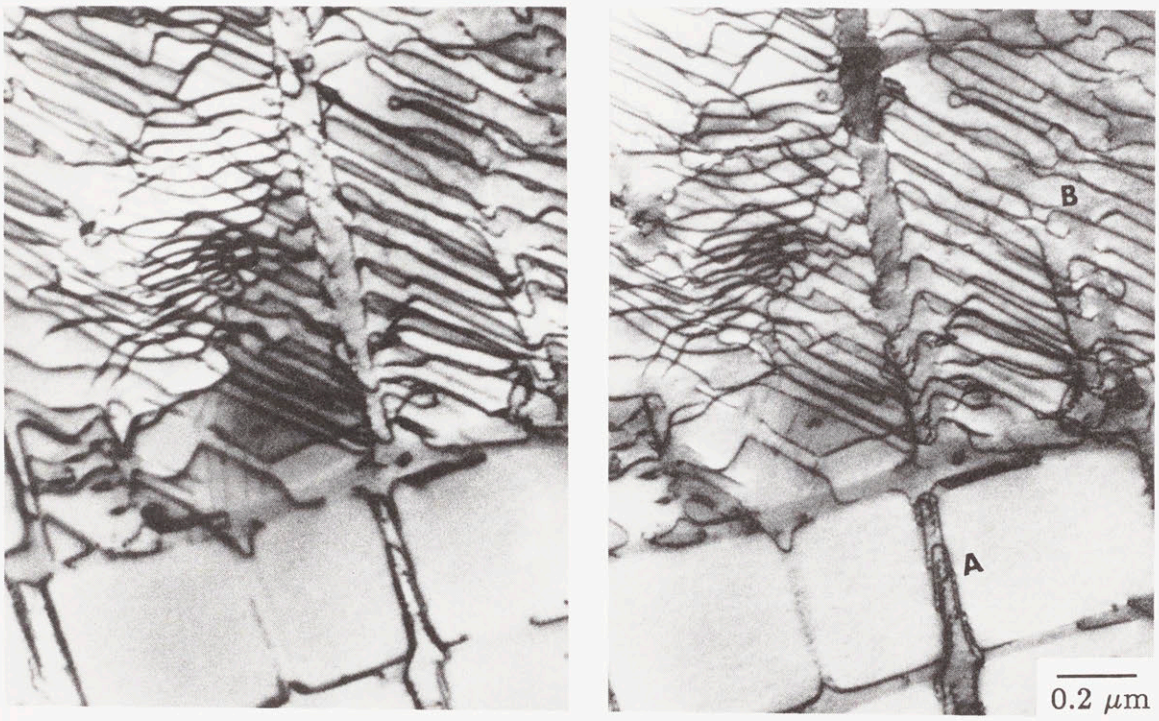

Figure 4.9 Stereo pair of dislocation structure during primary creep. Dislocations to the left of (A) are in a vertical matrix gap. The precipitate at (A) extends through the foil. The dislocations in region (B) are in a horizontal matrix gap which is contained in the plane of the thin foil.

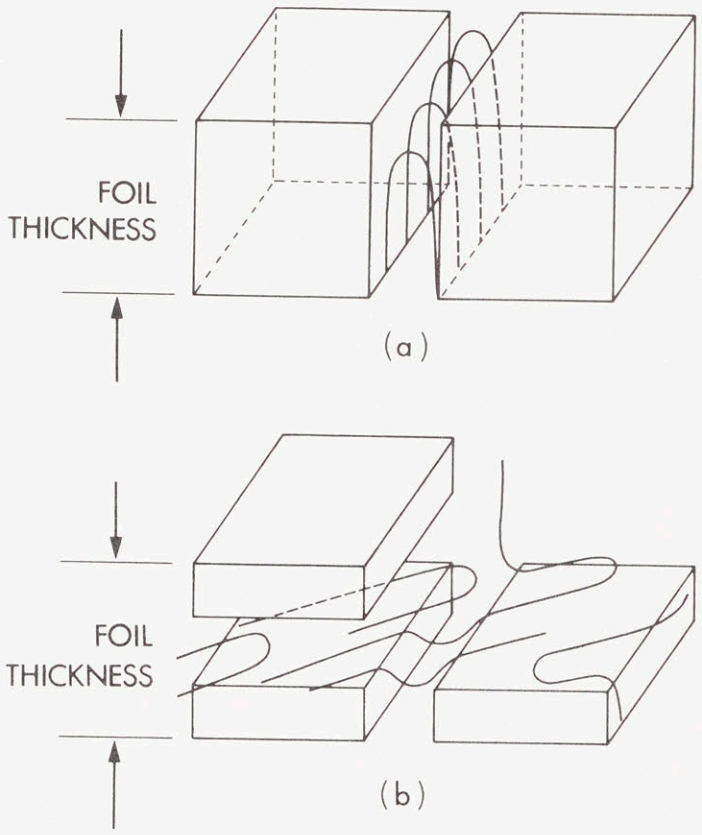

Figure 4.10 Schematic of matrix dislocation arrangements.
(a) Dislocations bowing through vertical matrix channels. This is similar to the arrangement in region (A) in Figure 4.9.
(b) Dislocations bowing through horizontal matrix passages. This is similar to the arrangement in region (B) in Figure 4.9.

their Burgers vectors inclined at an angle of 60°. As a consequence, these dislocations are at least partially relieving the misfit on the horizontal faces during primary creep. The dislocations which are contained in the vertical channels (parallel to the direction of applied stress, and normal to the plane of the foil) are also usually mixed in character, although pure screw dislocations are sometimes found in the vertical interfaces which contain the Burgers vector of the dislocation at the interface. Considering the geometry of the microstructure, it is not possible to relieve the misfit by depositing creep dislocations of edge character on the interfaces during the bowing out process. However, with the operation of multiple slip systems the misfit may be relieved by building up a series of mixed character dislocations at the interfaces. The issue of the relief of the misfit will be discussed in more detail later.

Observations on a large collection of samples taken from specimens at various times during the primary creep transient show that during the early stages of primary creep, locally, all dislocations have the same Burgers vector, but as the end of the transient is approached dislocations from many systems are present. This prevents any signifigant degree of crystallographic rotation, and leads to dislocation reactions and hardening as the strain is accumulated during the primary transient.

4.4 Steady State Creep

Once the "steady state" creep regime is reached the matrix has become completely filled with dislocations, with no matrix gaps left unpopulated. Figure 4.11 shows a low magnification view of the structure after creep at 850°C/552 MPa, giving 2.34% strain. Multiple slip systems are operative during steady state creep and as a result a three dimensional nodal network has built up in the matrix. A significant fraction of the dislocations present in the network form a "cage" around the γ' precipitates. The interfaces are not as sharply defined along the {001} planes as was the case in

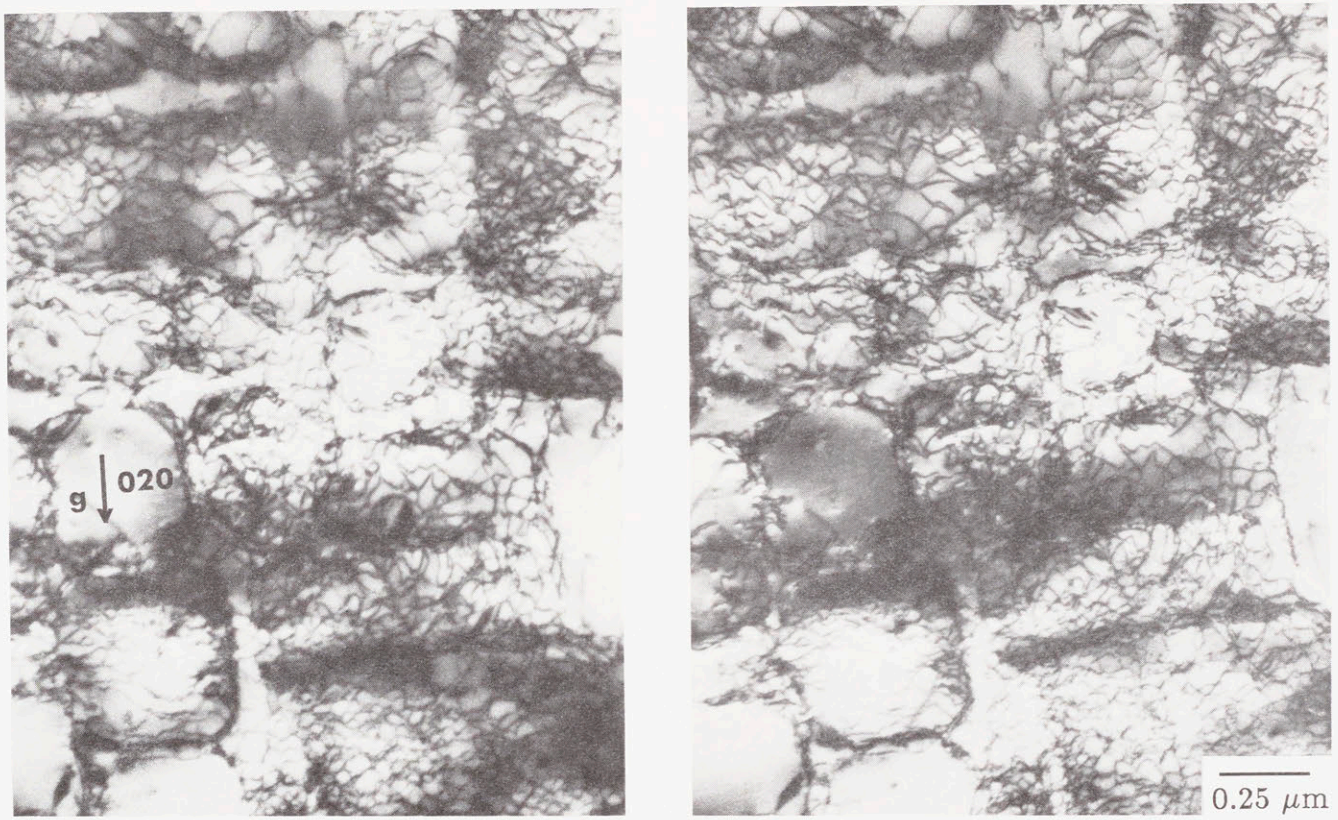

Figure 4.11 Stereo pair of the steady state dislocation structure showing all of the dislocations residing in the matrix material.

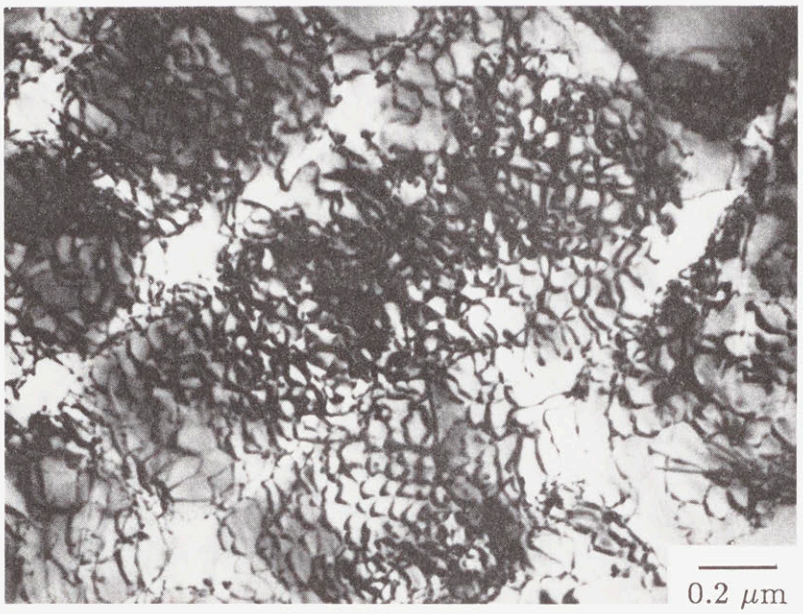

Figure 4.12 Matrix dislocation networks during steady state creep. A very organized three dimensional nodal network is present in the matrix in this particular area.

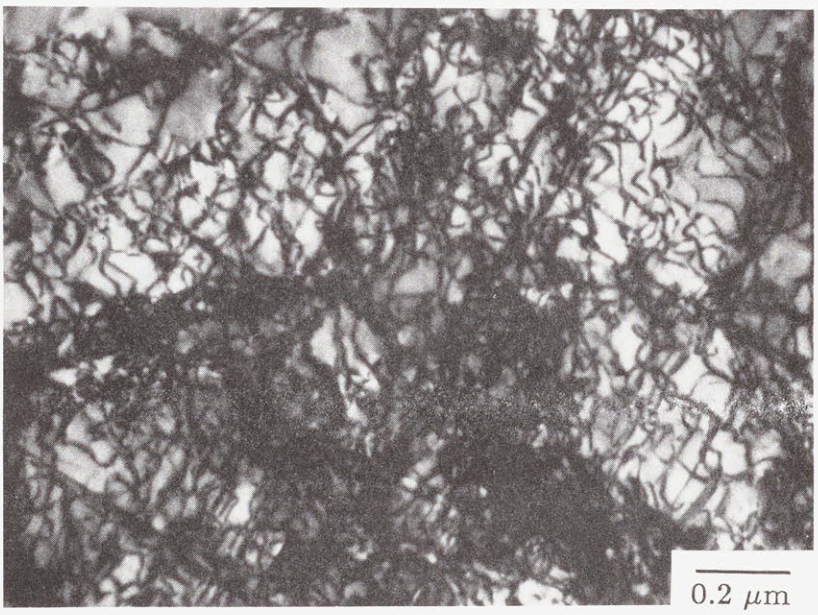

Figure 4.13 A region of locally high matrix dislocation density during steady state creep. The three dimensional network here is much less "organized" compared to other regions.

the early stages of the creep process. There are very few dislocations present which are not associated with the three dimensional network. Figures 4.12 and 4.13 show the network in more detail. It can be seen that in some areas the network is more organized with a large number of the dislocations associated with the interface, such as at the center of Figure 4.12. In other areas the matrix density of dislocations is higher, with more dislocations filling the matrix space, such as at the center of Figure 4.13. There were no noticeable differences in dislocation density for samples which accumulated different amounts of creep strain. Viewing the networks in stereo, it can be seen that the spacing of dislocations in the network is in the range of 50 - 120 nm, with 60 - 80 nm most commonly observed during steady state at 850°C/552MPa. Since the dislocations are present as a result of the creep process, and the network is three dimensional in nature, there are variations in the organization of the dislocations. However, Burgers vector analyses on selected local areas of the networks show them to be composed of three sets of dislocations, which are generally mixed in character. The networks lie in $\{111\}$ planes and the Burgers vectors of the three sets of dislocations are the three coplanar $a/2< 011 >$ type dislocations. Only local areas of the network lie in a single plane. Dislocations with Burgers vectors of $a/2[110]$ and $a/2[\bar{1}10]$ are less frequently observed than the other $a/2< 011 >$ types.

In the later stages of steady state creep and during tertiary creep it is not uncommon for the γ' precipitates to be sheared. Figure 4.14 shows pairs of dislocations shearing through a precipitate during the later stages of steady state creep (ϵ=2.2%). A sample which was tested to fracture at 850°C/552 MPa (273 hrs.) is shown in Figure 4.15. Viewing in stereo, it can be seen that all of the isolated dislocations in the light areas are dislocations lying inside the precipitates. (Since the precipitates have coarsened to some extent, the precipitates are extending through the foil thickness in

Figure 4.14 A precipitate sheared by dislocations in the later stages of steady state creep.

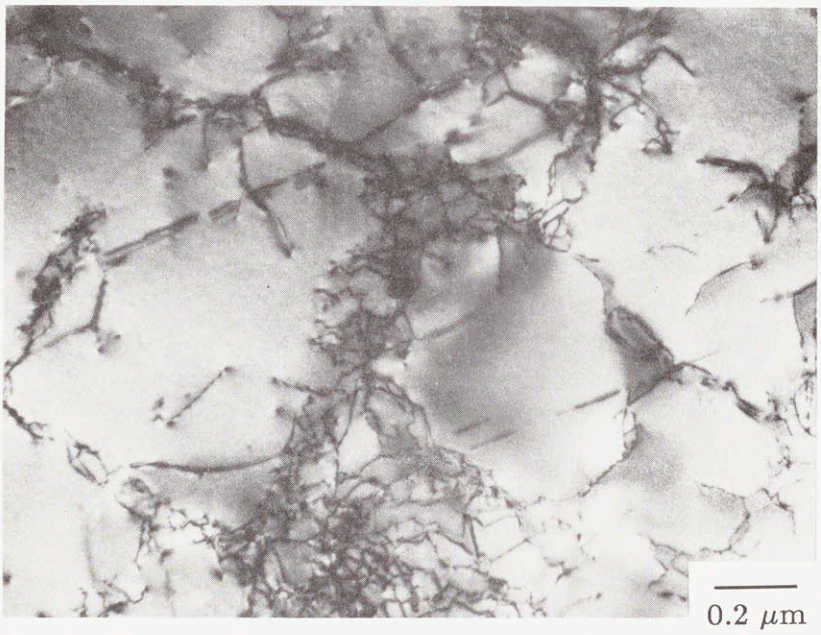

Figure 4.15 Dislocations in the γ' precipitates in a sample tested to fracture at 850°C. In the light areas the precipitates extend through the thickness of the foil, and all the isolated dislocations in these areas are in the γ'.

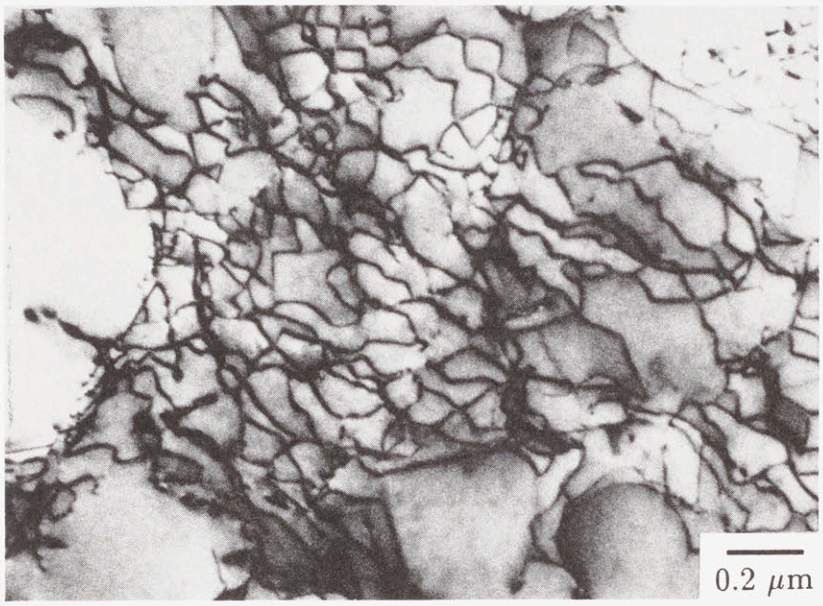

Figure 4.16 Recovered dislocation networks following 750 hours of bulk static annealing at 850°C. The dislocations are largely associated with the γ/γ' interfaces.

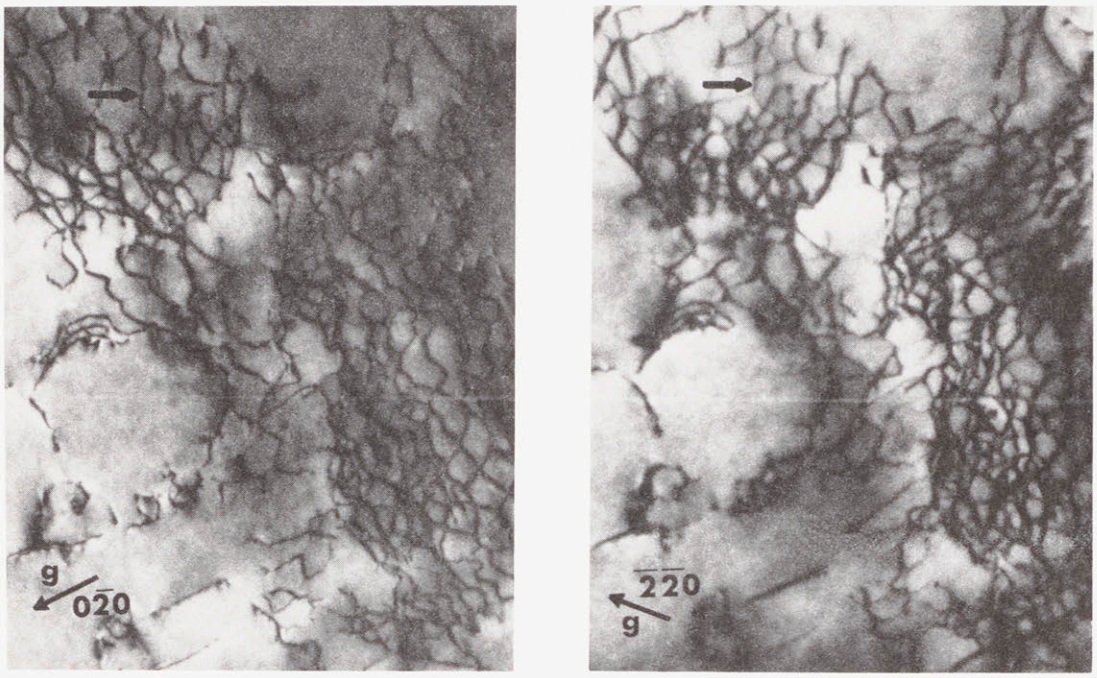

(a) (b)

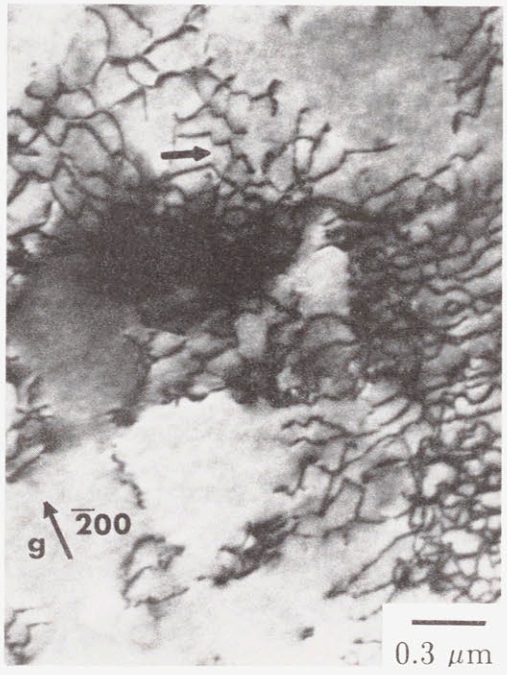

(c)

Figure 4.17 Recovered dislocation networks following 750 hours of bulk static annealing at 850°C. Locally, the networks contain three sets of dislocations. In the area marked by the arrows multiple diffraction conditions show the three sets of dislocations. In this area the dislocations are associated with the γ/γ' interface.

this case.) It appears that as creep deformation is accumulated in the matrix during the later stages of steady state creep and into tertiary creep, the precipitates are more likely to be sheared by dislocations entering from the matrix.

4.5 Recovered Dislocation Structures

In Figure 4.16 the three dimensional network is shown after 750 hours of bulk static recovery at 850°C. This annealing treatment was given to a sample which was crept to steady state at 850°C/552MPa and then cooled under load. Obviously the networks have persisted even after extended periods of annealing. Stereo pairs show, however, that the network is now more organized compared to the steady state network and it has coarsened noticeably from the steady state network, with dislocation spacings in the range of 80 - 100 nm. Compared to the steady state three dimensional network, the recovered network is associated with the γ/γ' interface to a greater degree. Again a Burgers vector analysis shows that locally the network is composed of dislocations with three different Burgers vectors. Figure 4.17 shows the different sets of dislocations imaged under three different diffraction conditions. The Burgers vectors of the three sets of dislocations in the area indicated by the arrow are a/2[011], a/2[101], and a/2[$\bar{1}$10], and this local portion of the network lies on a ($\overline{111}$) plane.

4.6 Structure Following Compression Testing

Figure 4.18 shows the dislocation arrangements following constant true strain rate compression testing at 800°C at a rate of $\dot{\epsilon} = 1.4\text{x}10^{-4}/\text{s}$. After 4.5% strain the sample was unloaded and quenched within 3 seconds. The maximum stress recorded during the compression test was 1024 MPa. Under these conditions the precipitates are easily sheared by dislocations, and isolated pairs of dislocations as well as stacking faults are observed inside the γ' precipitates. The stacking faults are present on multiple {111} planes. The structure obviously indicates a mode of deformation different from that

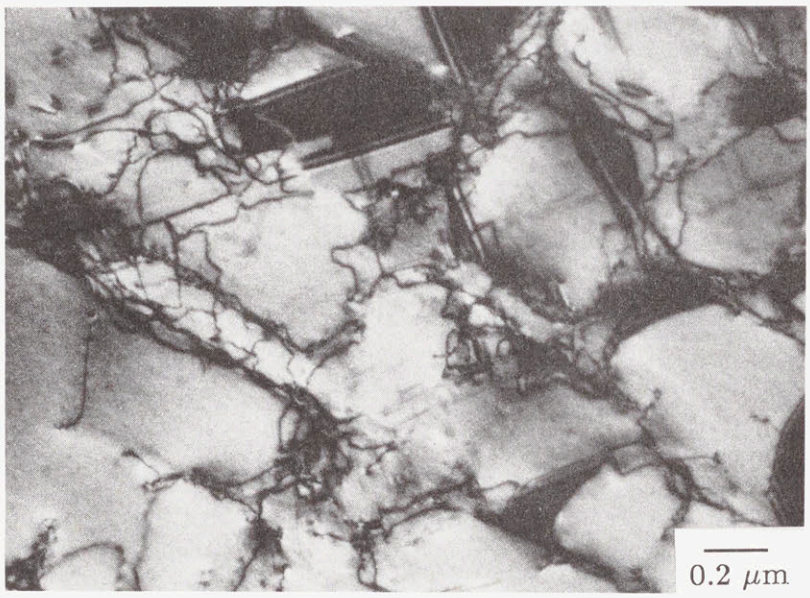

Figure 4.18 Shearing of the γ' precipitates as a result of compression at a rate of 1.1×10^{-4}/s at 800°C. Stacking faults which extend across the precipitates are created by dislocations shearing the γ' on multiple {111} planes.

observed as a result of the slower creep deformation at lower stresses.

4.6 In-situ Annealing Observations

Foils from samples which were pre-deformed to steady state were prepared to observe any dislocation rearrangements during in-situ annealing. The observations were made at temperatures around 850°C since this was the temperature of interest in the creep experiments. At temperatures above 900°C it was difficult to make any observations, since fairly rapid degradation of the sample surfaces occurred. Annealing experiments on six different samples were completed at temperatures near 850°C, with no significant differences from sample to sample. The area of observation was always a horizontal matrix channel contained in the plane of the foil. In one case the matrix channel was enclosed by precipitates on both sides. It is interesting to note that the behavior of this sample was not any different than the others where the matrix material was not isolated from the foil surface by precipitates.

Figure 4.19 shows a fairly low magnification view of the dislocation structure before heating, and after 30 minutes of annealing at 853°C. Due to a slight amount of drift which necessitates slow adjustments in the tilt, the contrast is not always exactly the same from one micrograph to the next. However it is obvious that there are no major rearrangements of the dislocations after annealing the foil for 30 minutes. At 850°C the rearrangements that do occur in the structure take place on a very local scale of the order of the network spacing, such as the area referenced by arrows in the photographs. The changes are fairly smooth, and usually difficult to observe in real time. Occasionally some motion is observed for a single dislocation which glides a short distance and annihilates or leaves through the foil surface, but this is not a common event. The limited static recovery that does occur at this temperature does not appear to be of the jerky type described by Prinz, Argon and Moffatt [67] in pure

metals such as copper and nickel.

In Figure 4.20 is a series of micrographs where the sample was initially held at 845°C for 45 minutes, and then the temperature was increased to 882°C and held. Again a comparison of the structure at the start (a), and after 17 minutes at 845°C (b), shows very little change. However after increasing the temperature to 882°C for 31 minutes (c), noticeable changes in the structure have occurred. The overall density of dislocations has decreased and the network has become very coarse. Again the changes were not due to a collapse of the network, but to more gradual coarsening. From the series of micrographs obtained in this experiment, changes in dislocation density were measured as described in the chapter on experimental procedures. The results are plotted in Figure 4.21 on a logarithmic scale. It is difficult to measure significant changes in dislocation density at at 845°C. However at 882°C there are measurable changes in dislocation density as a result of the static annealing process. The slope of the line through the data in Figure 4.21 is -0.74, and from this the rate of decrease of dislocation density is proportional the density as $d\rho/dt \propto \rho^{2.3}$.

To summarize, it appears that the steady state dislocation structure consists of a very stable three dimensional network of dislocations, with few "extra" dislocations in the structure. Static recovery in this configuration, even in thin foils, is a difficult process. It is likely that the limited dislocation rearrangements observed at 850°C are associated with annihilation of these extra dislocations, and some of these rearrangements are probably aided by the thermally induced stresses caused by heating the foils. In contrast, at temperatures approaching 900°C there is noticeable coarsening of the overall network dislocation structure during static annealing.

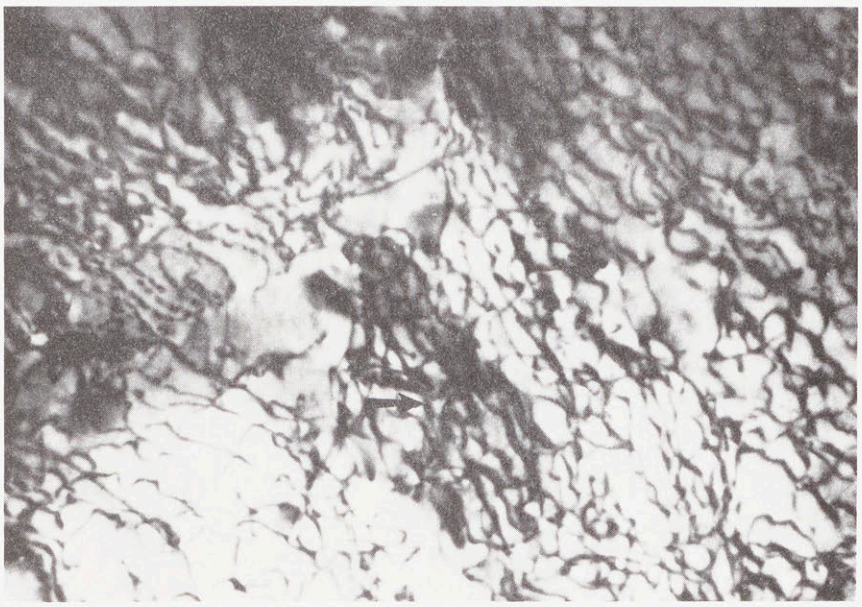

Figure 4.19 (a) Dislocation structure at the start of the 853°C in-situ annealing experiment.

Figure 4.19 (b) Dislocation structure after 30 minutes at 853°C.

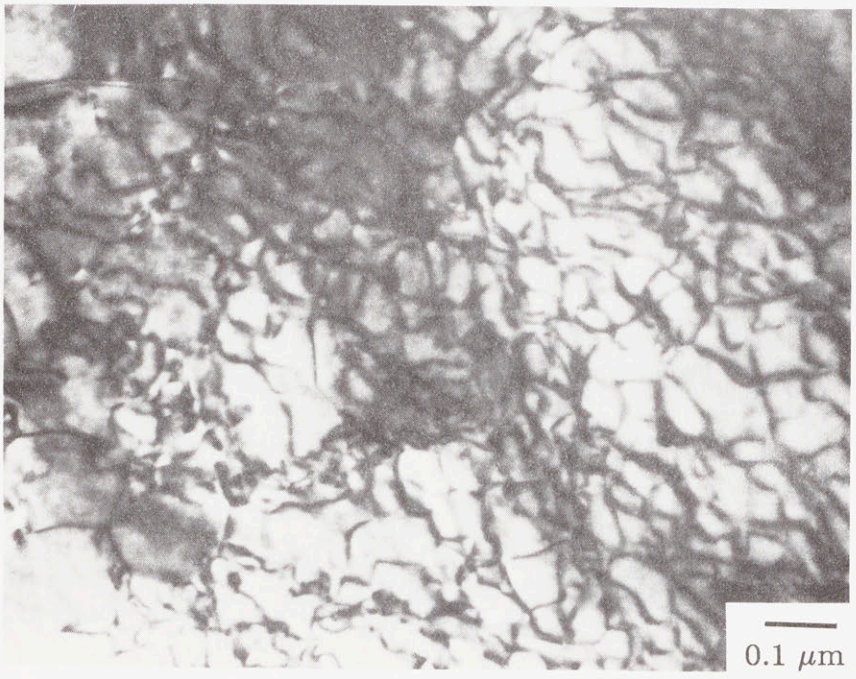

Figure 4.20 (a) Dislocation structure at the start of the 845°C in-situ annealing experiment.

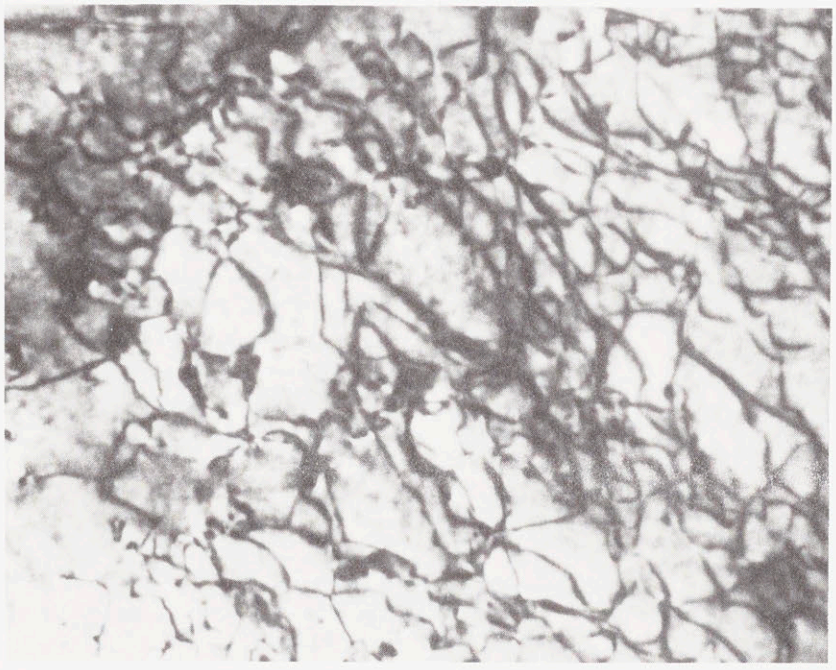

Figure 4.20 (b) Dislocation structure after 17 minutes at 845°C.

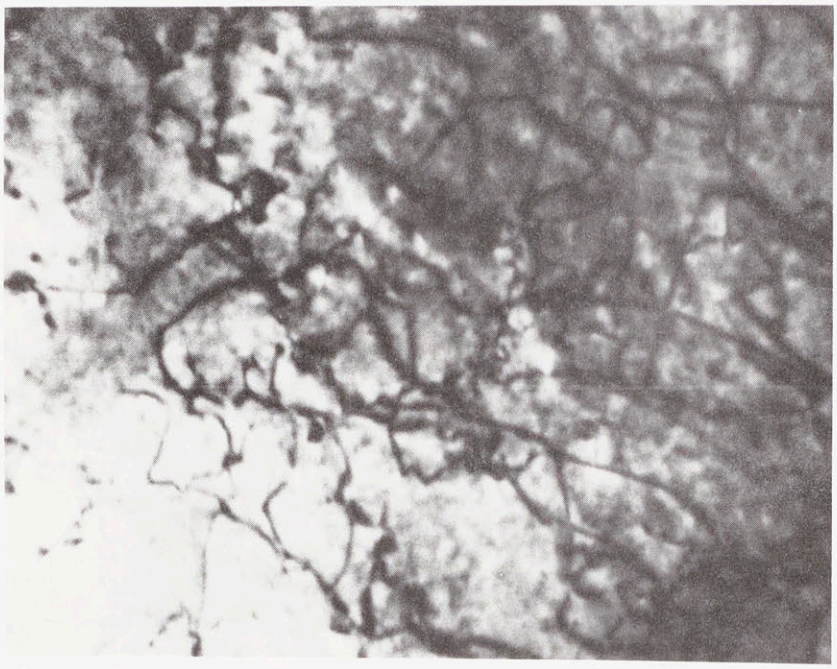

Figure 4.20 (c) Dislocation structure after 845°C for 45 minutes and 882°C for 31 minutes.

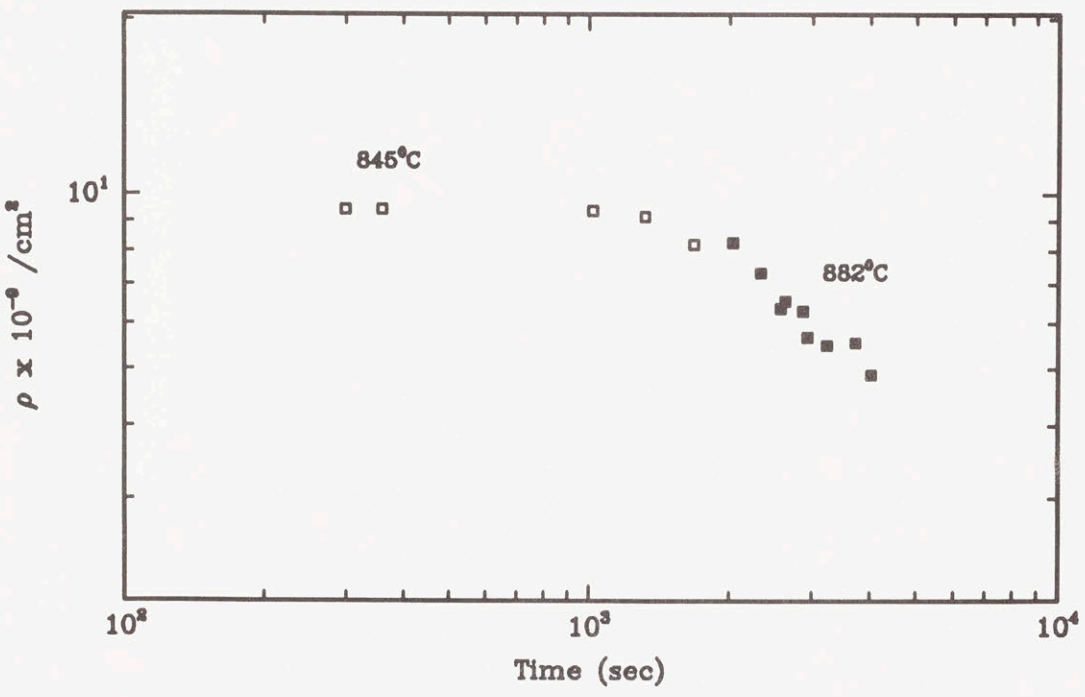

Figure 4.21 Dislocation densities during the 845 and 882°C in-situ annealing experiment.

Chapter Five

CREEP RESISTANCE OF THE TWO PHASE γ/γ' MATERIAL

As discussed in the previous chapter, stereo pairs clearly show that during creep the γ' precipitates remain undeformed and all of the creep deformation occurs in the matrix material. Using this fact, this chapter will address the micromechanics of the creep deformation problem with emphasis on the bulk creep properties of the matrix phase relative to the creep properties of the two phase material. Continuum calculations and a finite element analysis of the γ/γ' deformation problem provides information about the creep deformation process which is complementary to the TEM observations, and consideration of all of this information provides a better understanding of the overall creep resistance of the two phase material.

5.1 The Friction Hill Problem

During creep of the two phase nickel base material there are thin layers of creeping matrix material surrounded by rigid, non-deforming precipitates. This is comparable to the problem of compression of thin disks between rigid platens, first described by Schroeder and Webster [72]. In their analysis, a pressure gradient, or "friction hill", builds up in the deforming thin disk due to frictional sticking between the disk and platens. The pressure gradient increases the average load carrying ability of the material, and as the aspect ratio of the disk is increased, increasingly higher applied loads are required to deform the material. When there is no slipping along the interface, the average applied compressive stress, P, required to deform a disk of material with an

equivalent bulk plastic resistance σ_o gives an average factor of increased load carrying ability $(P/\sigma_o)_{avg}$ of:

$$\left(\frac{P}{\sigma_o}\right)_{avg} = 1 + \frac{2k}{3}\left(\frac{R}{t}\right) \tag{1}$$

where R is the disk radius, t is the thickness, and k is a constant numerically equal to 0.577.

Considering the reverse problem of pulling on a thin disk in tension, there is a *negative* pressure gradient along the length of the disk from $r = 0$ at the center to $r = R$ at the outer edge and:

$$\frac{\sigma(r)}{\sigma_o} = 1 + 2k\left(\frac{R}{t} - \frac{r}{t}\right) \tag{2}$$

where $\sigma(r)$ is now the tensile stress at a distance r and σ_o is the equivalent tensile plastic resistance.

To use the Schroeder and Webster analysis to estimate the net effect of the frictional constraint of the γ' precipitate in the two phase material, it is necessary to consider not only the problem of extending matrix channels normal to the applied stress but also compressing channels parallel to the applied stress. By superposition, the total average increase in load carrying ability is approximately:

$$\left(\frac{P}{\sigma_o}\right)^{tot}_{avg} = 2\left[1 + \frac{2k}{3}\left(\frac{R}{t}\right)\right] \tag{3}$$

The total average increase in load carrying ability of the γ/γ' material over that of the matrix material can then be estimated using the characteristic microstructural dimensions of the γ/γ' material and $R/t = L/(t\sqrt{\pi})$, where L is the channel length and t the matrix channel thickness. For a channel length of 0.45 μm and thickness of 60 nm, $L/(t\sqrt{\pi}) = 4.23$, and the calculated factor of increase in average load carrying ability of the γ/γ' material $(P/\sigma_o)^{tot}_{avg} = 5.34$.

Using creep data from Johnson et. al. [62] for Ni-6W creep tested at 854°C, the nickel solid solution matrix has an equivalent tensile creep resistance of about 35 MPa for a reference rate of 2.5×10^{-8}/s. (This reference rate will be used throughout the chapter.) The experimental tensile creep resistance of CMSX-3 at this rate is 552 MPa. A thin slab of nickel solid solution material with dimensions characteristic of the matrix channels in the γ/γ' material would then have an average creep resistance P = (35 MPa)(5.34)=187 MPa. Or conversely, to support a stress of 552 MPa, the equivalent creep resistance σ_o of the matrix material would have to be (552 MPa)/(5.34) = 104 MPa, which is three times the observed bulk creep resistance of the nickel solid solution material. Considering the bulk creep resistance of the nickel solid solution plus the frictional constraint of the γ/γ' interfaces obviously does not explain the experimentally observed creep resistance. However, for a more thorough analysis of this problem and a comparison to the above Schroeder and Webster solution, a finite element analysis of the γ/γ' deformation problem was performed, and this will be discussed in the following section.

5.2 The Finite Element Model

The finite element model was formulated using generalized plane strain elements. These elements allow uniform displacements in the "thickness" direction of the mesh by allowing displacement of a single node which is fixed to a plane in the third dimension of the model. This permits expansion in the third dimension as well as the development of stresses and uniform strains in this direction.

Utilizing the symmetry of the microstructure, it is only necessary to model one quarter of the γ' precipitate with its adjacent matrix. The mesh is shown in Figure 5.1, where the shaded portion corresponds to the matrix material, and the unshaded area to the precipitate. The matrix channel parallel to the upper boundary in Figure

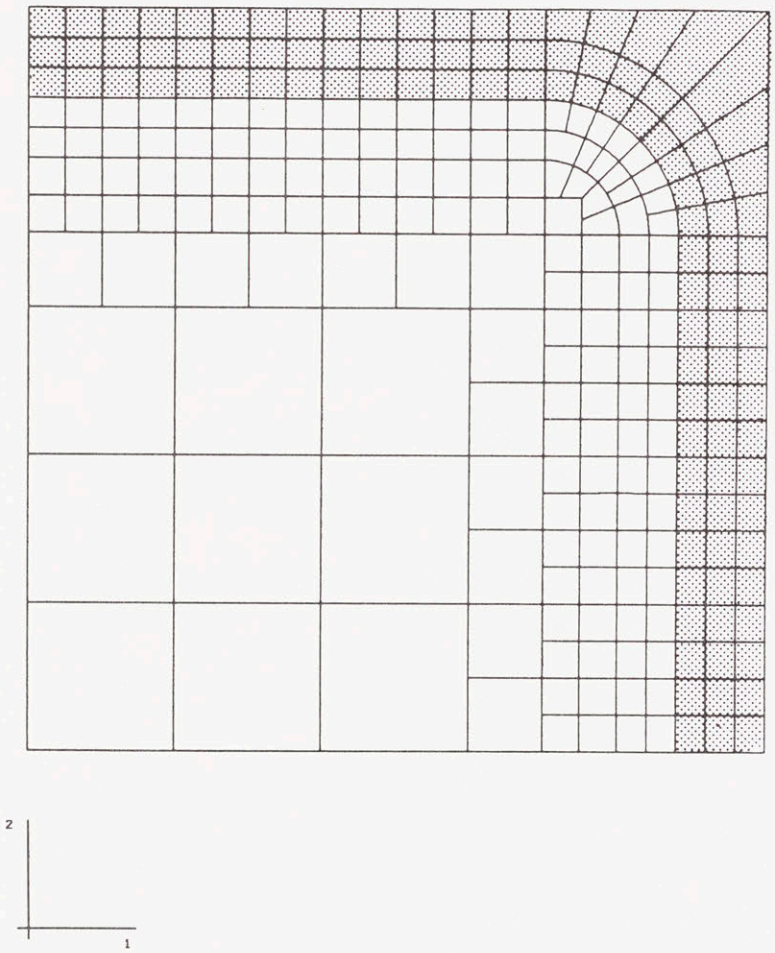

Figure 5.1 Finite element mesh of the γ/γ' problem. The shaded area corresponds to the matrix material.

5.1 (parallel to the 1 direction) will be referred to as the horizontal channel, while the channel parallel to the right border will be referred to as the vertical channel. Loads and prescribed displacements were applied along the 2 direction, normal to the horizontal channel. This direction corresponds to the $< 001 >$ direction in the single crystal, which is the usual orientation of the major loading axis in commercial single crystal components. As can be seen, the model was formulated in a way which would preserve the channel dimensions relative to the microstructure, but since a generalized plane strain analysis is done, the volume fraction of the γ' is somewhat higher here than in the actual material because the matrix channels parallel to the plane of the mesh are neglected.

It should also be noted that the γ/γ' boundary is tied together by common nodes along the boundary, which do not permit sliding. The "coherency" of the precipitate is then effectively enforced by the model. The consequences of this requirement will be discussed later.

Since TEM studies show that the γ' remains undeformed until the later stages of steady state creep, the precipitate is permitted to deform only elastically, while the matrix material may deform by creep. The single crystal elastic constants of the matrix and precipitate materials were estimated from the best available data for similar compositions. For the matrix material, the data for pure nickel from 25 - 487°C listed in Simmons and Wang [68] was extrapolated to 850°C. The resultant constants were nearly identical to those of DS Mar-M-247 [69] at 850°C. For the γ' precipitate, the room temperature constants for Ni_3Al + Ta of Curwick [70] were extrapolated to 850°C assuming the same temperature dependence as the constants for pure nickel. The resulting difference between the elastic constants of the matrix and precipitate was less than 7%, with the matrix being slightly more stiff than the precipitate. The

actual values of the constants can be found in Appendix C in the ABAQUS program listing.

The < 001 > orientation is a multiple slip orientation and no significant crystallographic rotations will occur in the course of creep deformation if all of the systems are active, so a simple isotropic power law relation was used to characterize the creep properties of the matrix:

$$\dot{\varepsilon}_{ss} = A\sigma^n \tag{4}$$

Again, the creep properties for Ni-6W tested at 854°C by Johnson et. al. [62] were used in the analysis, with n=4.8 and the pre-exponential constant, A, equal to $5.4\text{x}10^{-15}$ sec^{-1} $\text{MPa}^{-4.8}$.

Lattice mismatch between the two phases was incorporated by assigning the phases their respective coefficients of thermal expansion. The coefficients for the individual phases were estimated using the data of Grose and Ansell [71]. Assuming that the misfit at room temperature is zero and using coefficients of expansion of $1.63\text{x}10^{-5}/^{o}\text{C}$ and $1.26\text{x}10^{-5}/^{o}\text{C}$ for the γ and γ', respectively, gives a misfit of δ=-$3.05\text{x}10^{-3}$ at 850°C. This value is slightly lower than that reported by Fredholm and Strudel [36] for their measurement of dislocation spacings after aging CMSX-2 at 1050°C, and close to the value measured by high temperature X-ray diffraction at 850°C for a similar alloy [75].

Due to the symmetry of the microstructure, the upper and right boundaries are constrained to remain plane during the analysis. Nodes along the bottom and left boundaries are permitted to move only in the 1 and 2 directions, respectively.

Separate analyses were completed under conditions of displacement control and by applying loads to the upper boundary. For the displacement control analysis, the upper boundary was displaced with respect to the lower boundary to give a macroscopic creep

rate of $2.5x10^{-8}$/s. Load control analyses were completed by imposing a load which is distributed along the upper boundary. All analyses were run using ABAQUS finite element code on a DG MV10 computer.

5.3 Results of the Displacement Control Analysis

With thermal expansion, the initial negative mismatch between the γ and γ' phases is $-3.05x10^{-3}$. The stresses in the plane of the interface are compressive, while the stress normal to the interface is tensile. For the imposed misfit of $-3.05x10^{-3}$ the misfit stresses are rather high, with biaxial compressive stresses of 433 MPa in the plane of the interface, and a tensile stress of 50 MPa normal to the plane of the interface. In the generalized plane strain analysis, this gives equivalent misfit stresses of 456 MPa in the matrix material. These misfit stresses serve as an additional driving force to the creep deformation process at the start of the analysis. (In a separate analysis, these stresses proved to be high enough to partially relax the misfit when the material was held at 850°C under no other imposed stresses or displacements. The equivalent misfit stresses were reduced by 41% after a hold time of $2.56x10^{6}$ seconds.)

Displacing the upper boundary with respect to the lower at a rate of $2.5x10^{-8}$/s. allows for relaxation of misfit stresses in approximately $1.54x10^{4}$ seconds (4.28 hours), during which equivalent creep strains of $5.78x10^{-3}$ accumulate in the matrix. As the creep progresses from this point there is a buildup of negative pressure in the horizontal channel and positive pressure in the vertical channel. These pressures build up monotonically from the corner of the precipitate to a maximum at the channel center, as shown in Figure 5.2. The equivalent stresses are also shown in Figure 5.3. The pressures continue to build until the ratio of the maximum negative pressure to the equivalent stress reaches about 10 in the horizontal channel.

As the creep process proceeds, the material adjacent to the γ/γ' interface begins to

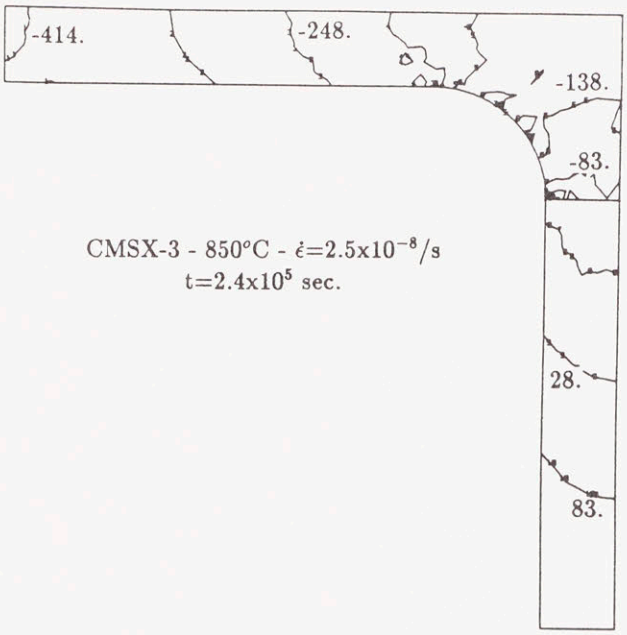

Figure 5.2 Pressure gradients (MPa) in the matrix material during steady

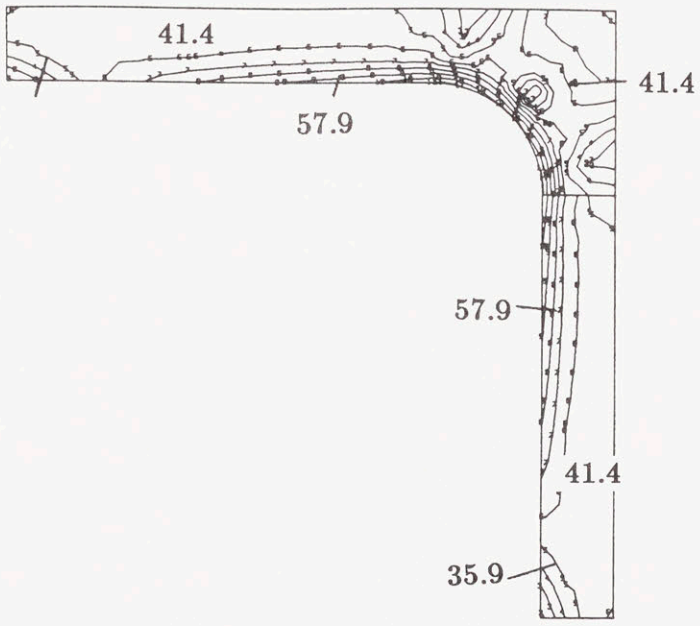

Figure 5.3 Equivalent stress contours (MPa) for the matrix during steady state creep, t=2.4x10^5 sec.

shear along the interface, showing a tendency to flow from the vertical channel toward the horizontal channel. This is shown in a displaced plot of the mesh in Figure 5.4. Although the ratio of the maximum pressure to the equivalent stress remains constant, there is a gradual increase in the matrix equivalent creep resistance, and therefore the absolute level of pressure rises gradually at very long times in the analysis. The equivalent stresses in the matrix are 32, 35.6, and 40.8 MPa at times of $1.75 \text{x} 10^5$, $2.07 \text{x} 10^5$, and $2.41 \text{x} 10^5$ seconds, respectively.

Since the precipitate does not deform by creep, the stresses inside the precipitate continue to rise with increasing matrix creep deformation. In Figure 5.5 the contours of equivalent stress are shown at times of $1.1 \text{x} 10^5$, $4.3 \text{x} 10^5$ and $7.7 \text{x} 10^5$ seconds. The maximum equivalent stresses at these times are 262, 965, and 1655 MPa, respectively. Compared to the experimentally measured value of the 0.2% yield strength at 850°C, these stresses are fairly low in the early stages of the analysis, but become much higher than the yield stress of the two phase alloy at longer times. It is expected that at some critical point the precipitate would be sheared by dislocations as the stresses inside the precipitate rise to high enough levels. It is interesting to note that dislocations are found to shear the γ' precipitates by entering at the same location in Figure 4.14 as the finite element results show to be the most highly stressed location in the precipitate.

5.4 Comparison of Finite Element Results with the Schroeder and Webster Analysis

For the displacement control analysis discussed in the last section, values of $(P/\sigma_o)_{max}$ and $(P/\sigma_o)_{avg}$ can be compared to those calculated by the Schroeder and Webster analysis. In the finite element analysis at a time of $2.41 \text{x} 10^5$ seconds $(P/\sigma_o)_{max} = 11.0$ and $(P/\sigma_o)_{avg} = 6.55$. The Schroeder and Webster calculation gives $(P/\sigma_o)_{max} = 8.67$ and $(P/\sigma_o)_{avg} = 5.34$. Looking at the finite element mesh in Figure 5.1, it is clear

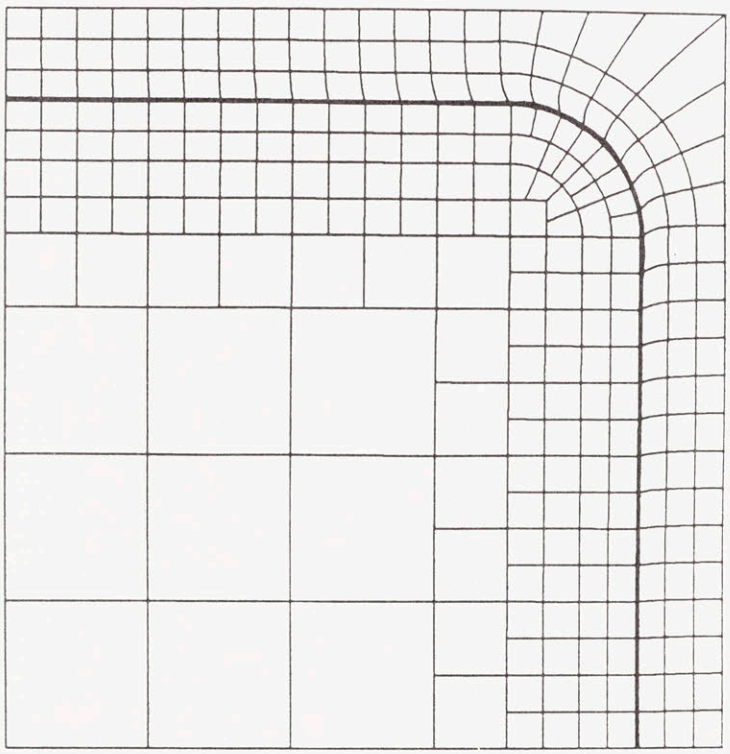

Figure 5.4 Displaced plot of the finite element mesh after creep.

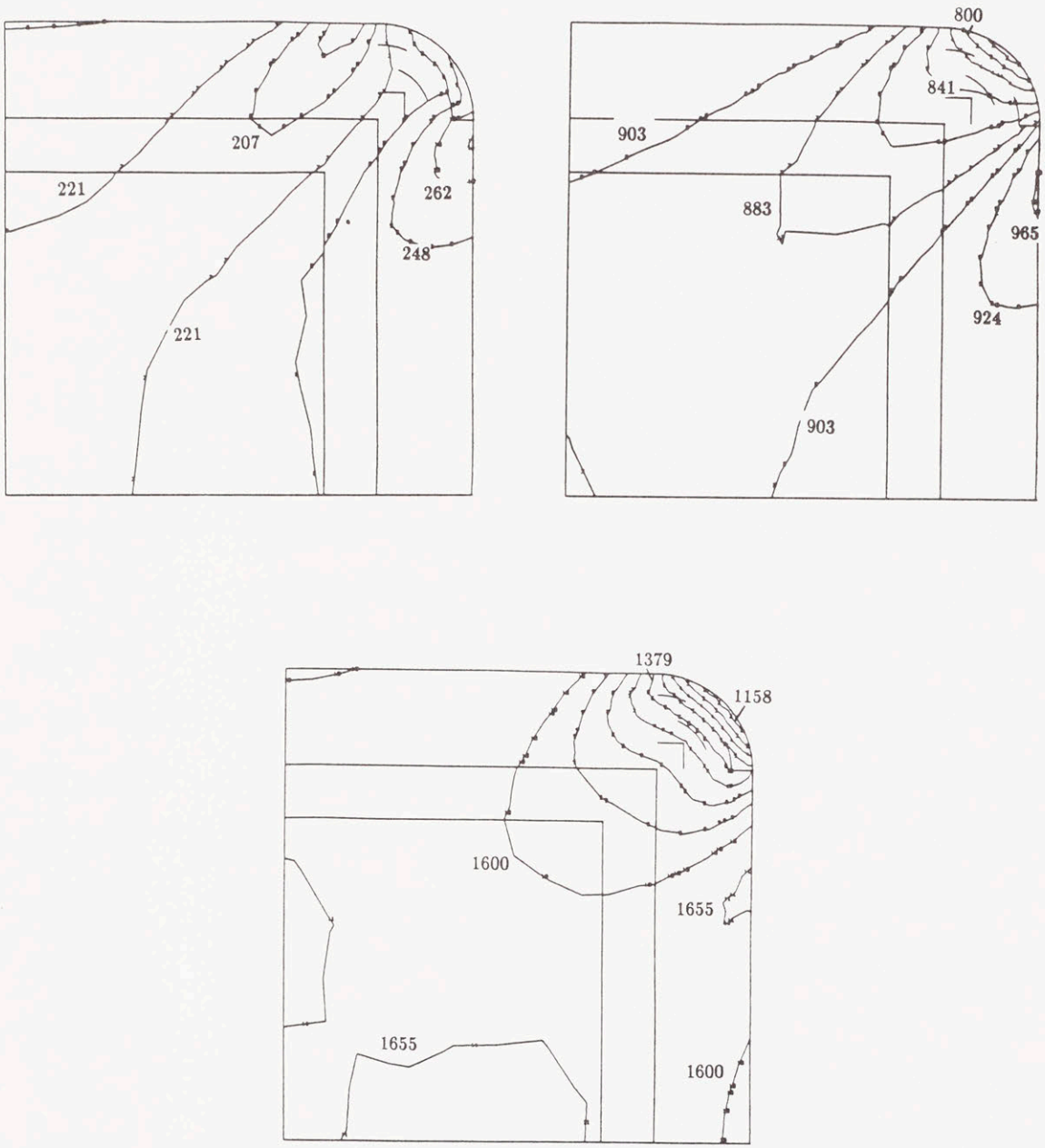

Figure 5.5 Contours of equivalent stress in the precipitate at times of (a) 1.1×10^5 sec, (b) 4.3×10^5 sec, (c) 7.7×10^5 sec.

that the material at the corner of the precipitate (upper right) is not included in the Schroeder and Webster calculation. If it is included, effective length of the horizontal channel is increased, giving the Schroeder and Webster values of $(P/\sigma_o)_{max} = 9.24$ and $(P/\sigma_o)_{avg} = 5.52$. These values are slightly lower than the finite element values, but still reasonably close. In Figure 5.6 the pressure gradients along the horizontal matrix channel are plotted for the finite element analysis and the Schroeder and Webster solution. It can be seen that the magnitude of the buildup of the negative pressure along the horizontal channel is the same for both analyses, but the difference is the starting level of (P/σ_o) at end of the horizontal channel. This difference is likely to be due to the fact that there is additional constraint at the ends of the channel in the γ/γ' microstructure compared to a thin disk where the free surfaces at the ends of the disk are not required to remain plane.

From this it is clear that the frictional constraint to deformation in both the horizontal and vertical matrix passages provided by the precipitate leads to the buildup of large pressure gradients during the creep process. In the Schroeder and Webster analysis the constraint is due to frictional sticking of the "platens" to the deforming sample, while in the finite element analysis it is caused by the coherent interface, along which the nodes are "pinned" together. The net result is a large increase in load carrying ability of the nickel solid solution material.

To further check this comparison between the "friction hill" and the pressure gradients in the matrix of the two phase material, two additional analyses were completed. First, a new mesh was generated to give a simple γ/γ' thin disk for a direct comparison to the Schroeder and Webster solution. Using the same material properties as in the displacement analysis, the γ was again allowed to creep, as shown by the displaced plot of the mesh in Figure 5.7, and pressure gradients again were present. The level

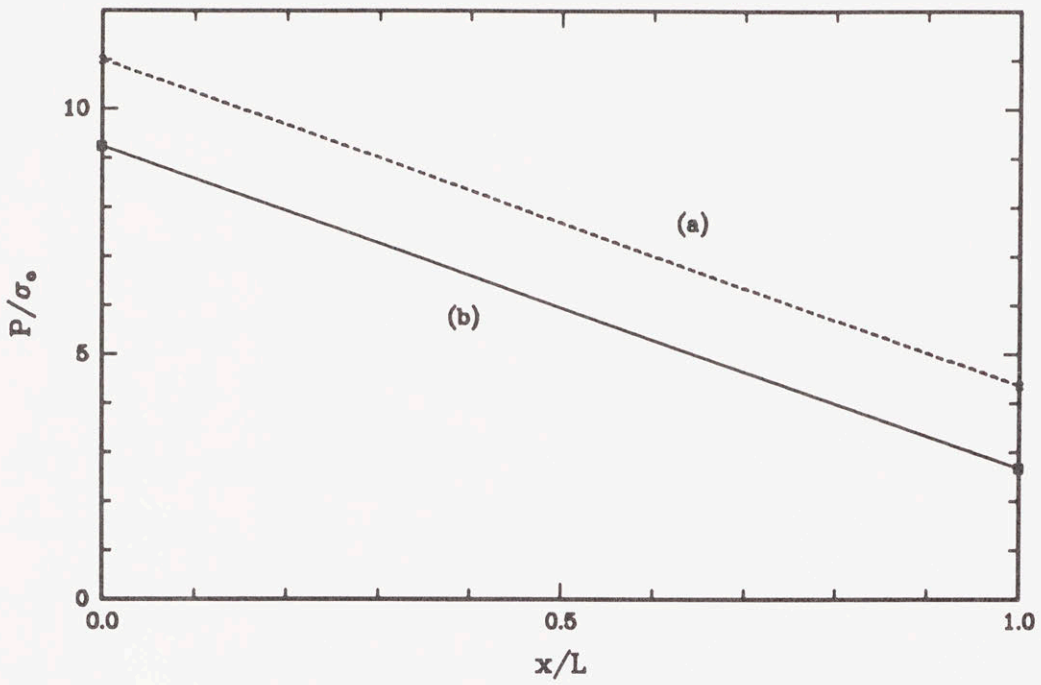

Figure 5.6 Comparison of normalized pressure gradients in the horizontal matrix channel for (a) the finite element analysis and (b) the Schroeder and Webster solution. The results are plotted as the fractional distance from the center of the channel, with x/L = 0 the center, and x/L =1 the outer edge.

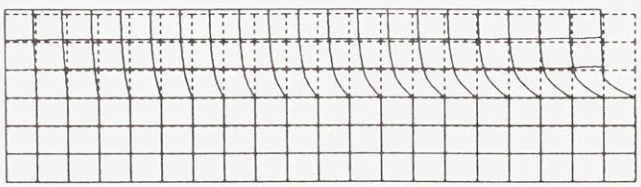

Figure 5.7 Displaced mesh of the γ/γ' thin disk model.

of $(P/\sigma_o)_{avg}$ for the finite element analysis in this case was only 10% higher than the Schroeder and Webster solution for a single thin disk (no superposition required). In addition, an analysis was run in which the right boundary of the γ/γ' mesh (Figure 5.1) was not required to remain plane. Without this constraint, no pressure gradient builds in the vertical channel, leaving only the horizontal channel to build up a negative pressure gradient. In this case the values of $(P/\sigma_o)_{max}$ and $(P/\sigma_o)_{avg}$ were again only about 10% higher than the Schroeder and Webster analysis for a single thin disk and essentially the same as found for the simple γ/γ' thin disk (Figure 5.7). So the agreement between the Schroeder and Webster analysis and the finite element analysis for a single thin disk is very good, and the Schroeder and Webster superposition problem gives a reasonably good estimate of the pressure gradients for the full γ/γ' problem.

5.5 Load Control Analyses

With the same boundary conditions and material properties as the displacement control analysis, several analyses were run with uniform loads applied to the upper boundary of the model. In these analyses, the macroscopic creep rate is calculated from the displacement rate of the upper boundary with respect to the lower.

Similar to the displacement control analysis, loading at 552 MPa gives an initial transient during which the misfit stresses are relaxed. This is followed by a gradual buildup of negative and positive pressure gradients in the horizontal and vertical channels, respectively. The precipitate is also increasingly stressed with accumulating creep strain in the matrix. However, the major difference between the displacement and load control analyses is that for the application of 552 MPa the development of the pressure gradients occurs in a shorter amount of time; $(P/\sigma_o)_{max} = 9.82$ at t=1170 seconds compared to $(P/\sigma_o)_{max} = 9.44$ at t=1.38x10^5 seconds in the displacement con-

trol analysis. At long times ($\approx 10^5$ sec), the creep rate for the application of 552 MPa is also higher than experimentally observed, at 6.4x10^{-7}/s. Since the experimental steady state creep rate of CMSX-3 loaded at 552 MPa is 2.5x10^{-8}/s., it is obvious that the actual creep resistance of the two phase alloy is much higher than can be accounted for by the continuum calculations here. Using the results of the displacement control analysis, the average equivalent stresses in the matrix at a macroscopic creep rate of 2.5x10^{-8}/s. are 35.9 MPa. Since $(P/\sigma_o)_{avg}$ ranges from 5.40 to 6.55, then uniaxial stresses of only 194 to 235 MPa can be supported at a reference rate of 2.5x10^{-8}/s. (The range of stresses supported arises from the fact that a true steady state level of equivalent stresses and pressures does not develop in the displacement control analysis.) This is only about half the experimentally observed creep resistance of CMSX-3. To confirm this, additional analyses run with applied stresses of 159 and 276 MPa. The applied stresses gave steady state creep rates of 1.14x10^{-9}/s. and 9.13x10^{-8}/s. respectively. This gives a creep stress exponent of $ln(\dot{\varepsilon}_2/\dot{\varepsilon}_1)/ln(\sigma_2/\sigma_1) = 7.9$ for the two phase deformation problem, compared to the creep stress exponent input for the matrix material of 4.8. In addition, this gives a creep resistance of 233 MPa for a steady state creep rate of 2.5x10^{-8}/s, which agrees with the calculated load support from the displacement control analysis. It is interesting to note that the presence of pressure gradients may elevate the creep stress exponent.

5.6 Discussion

It is clear from the finite element analysis that the γ/γ' creep deformation problem is not purely a continuum problem of creep deformation in a solid solution matrix constrained by coherent non-creeping precipitates. In order to completely characterize the creep resistance of the material it is necessary to consider the results of this analysis in combination with the TEM observations of the process of spreading dislocations

through the material so that it becomes fully creeping.

Most commercial nickel base single crystal alloys have a small negative mismatch at elevated temperatures, which increases in magnitude as the temperature increases due to differences in thermal expansion of the two phases. The equivalent misfit stresses for even a small mismatch of δ = -3.05x10^{-3} are high enough (456 MPa) to cause partial relaxation of the misfit. However, as seen in the TEM micrographs of the aged structure, dislocation sources are very widely spaced and spreading them uniformly throughout the structure is a difficult process at temperatures as low as 850°C. In fact, the CMSX-3 aging treatment of 870°C for 20 hours does not produce any relief of the misfit. Aging for extended periods at higher temperatures (1050 – 1100°C) where the misfit is higher and the deformation resistance lower does produce some relief of misfit [36,60]. The resultant effect of the misfit at the lower temperatures is only to provide an additional driving force for creep during the primary transient.

In the finite element analysis, accounting for the bulk creep resistance of the matrix material and the buildup of negative pressure, the maximum continuum creep resistance of the γ/γ' material is 233 MPa at a reference rate of 2.5x10^{-8}/s. The Schroeder and Webster analysis predicts a creep resistance of 184 MPa. Both of these estimates are far short of the experimentally observed resistance of 552 MPa.

5.6.1 Microstructural Considerations

From the TEM observations of the primary creep process, it is obvious that the local problem of bowing dislocations through the narrow matrix channels must give an additional resistance which is not accounted for in the finite element analysis. The resistance to bowing out through the channels is simply given by the Orowan stress:

$$\tau_{or} = \frac{\mu b}{l} \tag{5}$$

where μ is the shear modulus, b the Burgers vector, and l the channel spacing in the

{111} plane along the < 110 > direction. For μ = 48.2 GPa, b=0.254 nm., and $l = 60\sqrt{2}$ nm., the Orowan stress is 144 MPa. For the total shear resistance, the shear resistance of the nickel solid solution must be added to the Orowan stress giving 144 + 14.3 = 158.3 MPa. Dividing by the Schmid factor gives a uniaxial resistance of 388 MPa. This would give a factor of increased load carrying ability of

$$\left(\frac{P}{\sigma_o}\right)^{tot}_{avg} = \frac{552MPa}{388MPa} = 1.42 \tag{6}$$

for the combined problem of thinning vertical channels and thickening horizontal channels. Doing the Schroeder and Webster superposition problem in reverse gives $(P/\sigma_o)_{avg}$ = 1.22 for the single thin disk problem. This no longer corresponds to the case of infinite friction at the interface, but rather to the case where there is some sliding along the interface. In this case the Schroeder and Webster solution to the problem is:

$$\left(\frac{P}{\sigma_o}\right)_{avg} = \frac{2}{C^2}(e^C - C - 1) \tag{7}$$

where

$$C = \frac{2\eta L}{t\sqrt{\pi}}$$

and η is the coefficient of friction, and all the other constants have the same meaning as earlier. From this a coefficient of friction of η = 0.059 is found, and this corresponds to the coefficient of friction for the γ/γ' interface. Rather than an infinite friction interface (or completely coherent interface even after large amounts of creep deformation) this gives a more realistic explanation of some finite displacement between the γ and γ', which would occur for screw dislocations moving along the interface. The TEM observations do indeed show dislocations along the interfaces, reinforcing the fact that the γ/γ' interface does not have infinite friction, as it is necessary to assume with

the finite element calculation. Since there is interfacial sliding, the level of pressure support is lowered from the predicted 200 MPa to about 164 MPa.

To summarize, even the low level of γ/γ' misfit gives fairly high misfit stresses of 456 MPa. The misfit stresses provide a driving force above that of the applied load, resulting in initially higher stresses in the horizontal channel. As the creep process proceeds, the frictional constraint of the interface causes pressure gradients to build in the matrix channels. The finite element model predicts higher pressures than are actually present since the nodes along the interface in the model are pinned, and in reality dislocations on the interface can provide some amount of "sliding". The total creep resistance is then composed of the resistance to Orowan bowing between the γ' precipitates, the solid solution resistance, and the pressure gradients which build in the matrix channels. Since the precipitates are elastic, they become increasingly stressed as creep deformation accumulates in the matrix, and this may lead to eventual shearing of the precipitates.

Chapter Six

HIGH TEMPERATURE RAFTING

6.1 Introduction

As noted in Chapter 1, there is very little information on the directional coarsening process in positive misfit alloys, and in the two cases where there is some information, [56,58] the alloys contain very low volume fractions of γ' precipitates. For the negative misfit alloys, there are many reports of rafting of the precipitates at high temperatures accompanied with SEM micrographs only in the plane parallel to the loading axis. There is also very little information pertaining to the presence of dislocations, and their role in the process. This preliminary investigation of high temperature creep behavior was aimed at filling some of these gaps in information about the rafting process.

Both positive and negative misfit alloys with high volume fractions of γ' were utilized in these experiments. The negative misfit alloy was CMSX-3, which was the subject of the lower temperature investigations here. For the positive misfit alloy, a composition was constructed such that there would be both a high volume fraction of γ' and positive γ/γ' misfit. Since Ta and Ti are both observed to increase the lattice parameter of Ni_3Al [59] and volume fraction of γ', an alloy of composition Ni-15Al-2Ta-2Ti (a/o) was cast in single crystal form. A heat treatment of 1340°C for 6 hours put a large fraction of the γ' into solution and a regular distribution of cuboidal γ' about 0.6μm in diameter reprecipitates as shown in Figure 6.1. The volume fraction

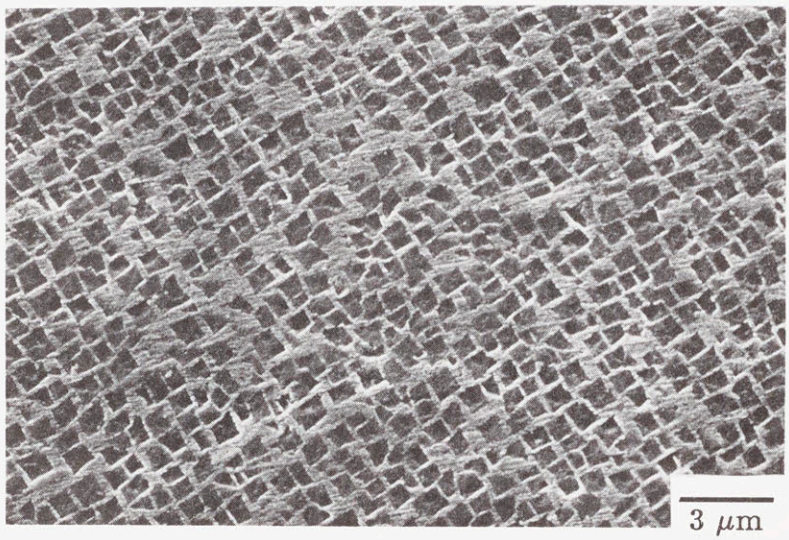

Figure 6.1 PMA alloy showing cuboidal γ' precipitates following solution treatment.

of γ' estimated from SEM micrographs is about 0.5. The absolute level of the misfit was not measured, but since Ni-15Al [56] has positive misfit at high temperature, Ti and Ta both tend to make the misfit more positive, and since cubes are present after cooling from the solution treatment, it is certain that there is a significant positive misfit at test temperature, and it is likely to be greater than 0.3%.

6.2 Rafting in Negative Misfit Single Crystals

With the CMSX-3 single crystals, a series of experiments were conducted in an effort to separate the creep processes from the rafting processes. As already reported, the aged crystals have very few dislocations and the Orowan stress for bowing them out from the grown-in areas is quite high. A sample was loaded at 850°C and 130 MPa for 228 hours, at stresses where no creep should occur, but at a temperature where limited linking of the precipitates has been observed at long times. For reference, Figures 6.2 and 6.3 show the precipitate distribution at 850°C but at at a stress of 552 MPa after 8 and 114 hours respectively. At 8 hours at 850°C and 552 MPa there is no change from the aged structure, but at 114 hours there is some linking of the precipitates, with part or all of the vertical matrix channels gone in some areas. (The plane shown is parallel to the loading axis, and the loading axis would be vertically oriented on the page.) After 228 hours at the lower stress of 130 MPa there is no evidence of any linking of the precipitates, and the structure looks very much like that shown in Figure 6.2. There was no creep observed in this time period.

Increasing the temperature to 900°C at a stress of 110 MPa again produced no signs of rafting or creep after 158 hours. At 950°C and 95 MPa there was a small amount of creep in the first few hours following the loading of the sample, and then no further creep was observed. A total creep strain of about 10^{-4} was accumulated. As can be seen in Figure 6.4, there are still no signs of a rafted structure. TEM micrographs

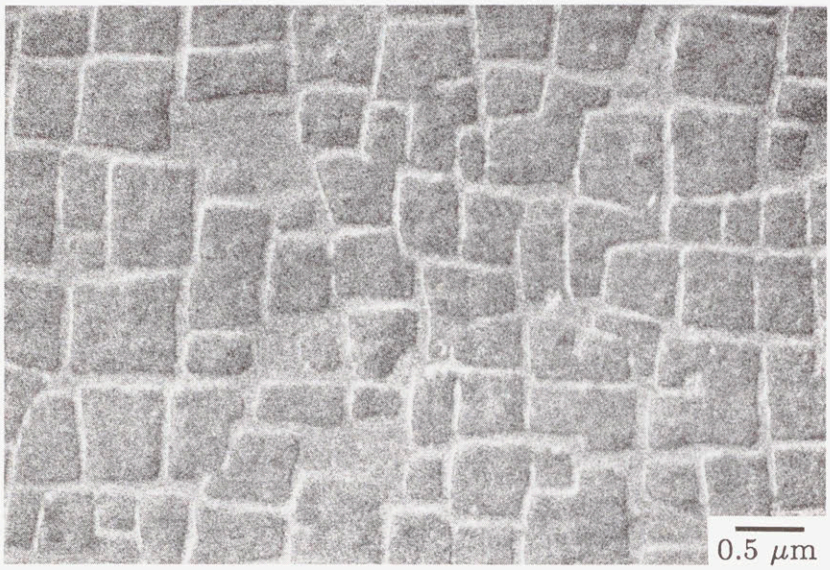

Figure 6.2 Precipitate morphology in CMSX-3 after 8 hours of creep at 850°C and 552 MPa. Tension axis is vertical.

Figure 6.3 Precipitate morphology in CMSX-3 after 114 hours of creep at 850°C and 552 MPa. Tension axis is vertical.

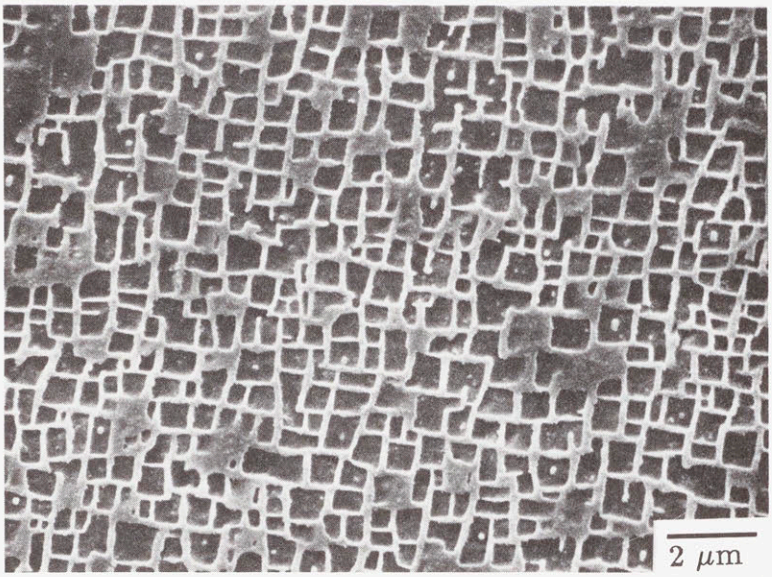

Figure 6.4 γ' precipitates (dark) in CMSX-3 after 950°C and 95 MPa for 158 hours. Tension axis is vertical.

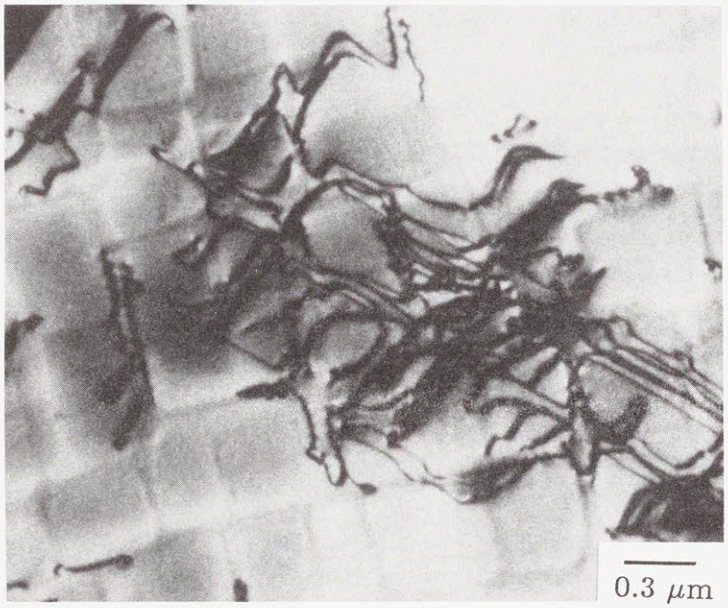

Figure 6.5 TEM micrograph of isolated dislocations after 950°C and 95 MPa for 158 hours. Tension axis is normal to the plane of the micrograph.

revealed some creep dislocations widely distributed in the matrix, as shown in Figure 6.5, but only a very small fraction of the matrix channels are populated by dislocations. Finally, at 1050°C and 50 MPa there was creep deformation, and along with that some rafts were observed to be developing with their long axis *normal* to the tension loading direction. Table 6.1 summarizes the testing conditions and observations covered for the CMSX-3 samples.

After creep strains of 0.0051 accumulated at 1050°C and 50 MPa in 48 hours in a CMSX-3 single crystal, the test was interrupted so microstructural observations could be made. Figures 6.6 and 6.7 are SEM micrographs of the precipitate morphology in two different areas of the sample viewed on a plane parallel to the loading axis. In some areas the rafted structure appeared to be fairly well developed, while in others the precipitates still appeared to be cuboidal in shape. TEM micrographs on foils taken from this sample also showed some interesting variations in precipitate morphology. These micrographs are now taken from a plane normal to the loading axis. In Figure 6.8 there is a "raft" in the lower portion of the micrograph which appears to be about 2 to 3 precipitate diameters in thickness and 3 to 4 precipitate diameters in length, extending through the thickness of the foil. There are no dislocations in the γ' material, but there are several that appear to be trapped in the prior γ/γ' interface. Note that there are creep dislocations adjacent to the raft. The raft could be roughly described as a plate with its broad face normal to the tension axis. Figure 6.9 shows a much different structure in the same sample, where the precipitate interfaces are still very well defined. In addition to there being very little shape change, it is interesting to note that there are very few creep dislocations present in the vicinity. Figures 6.10 and 6.11 show two additional views of the rafted structure, again in a plane normal to the loading axis. The rafts appear to be more irregular in shape in Figure 6.10, and

Table 6.1 Summary of CMSX-3 rafting experiments and observations.

Temperature (°C)	Stress (MPa)	Time (Hrs.)	Creep strain	Rafting
850	130	228	no creep	no
850	552	114	ϵ=0.022	limited
900	110	158	no creep	no
950	95	113	$\epsilon=10^{-4}$	no
1050	50	48	ϵ=0.0051	yes
1060	138	64	ϵ=0.0084	yes

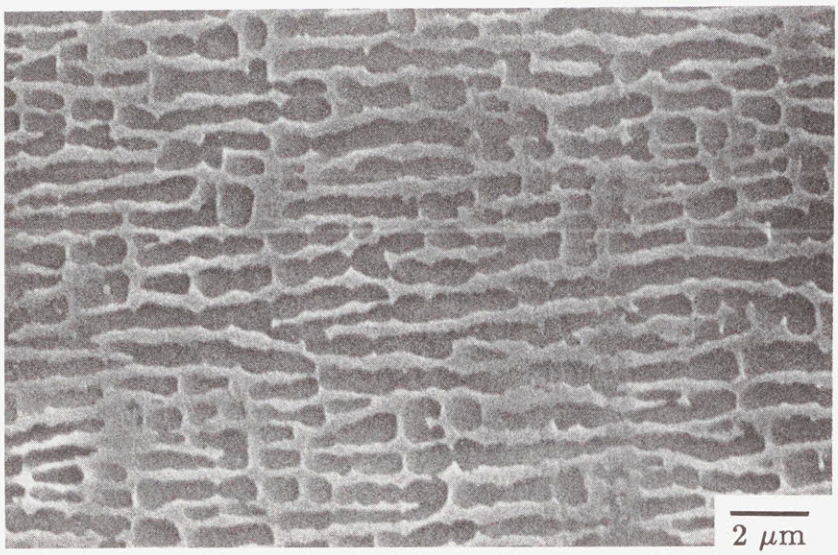

Figure 6.6 γ' precipitates following creep at 1050°C and 50 MPa for 48 hours. Tension axis is vertical.

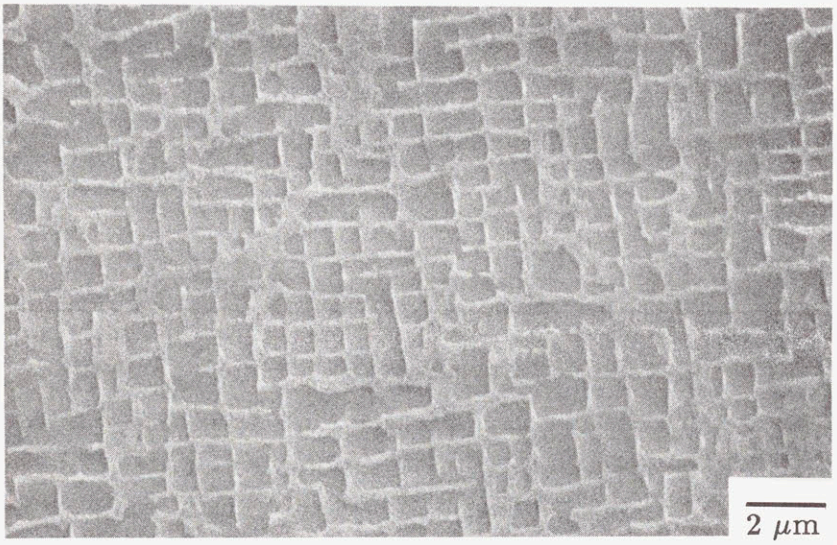

Figure 6.7 γ' precipitates following creep at 1050°C and 50 MPa for 48 hours. Tension axis is vertical.

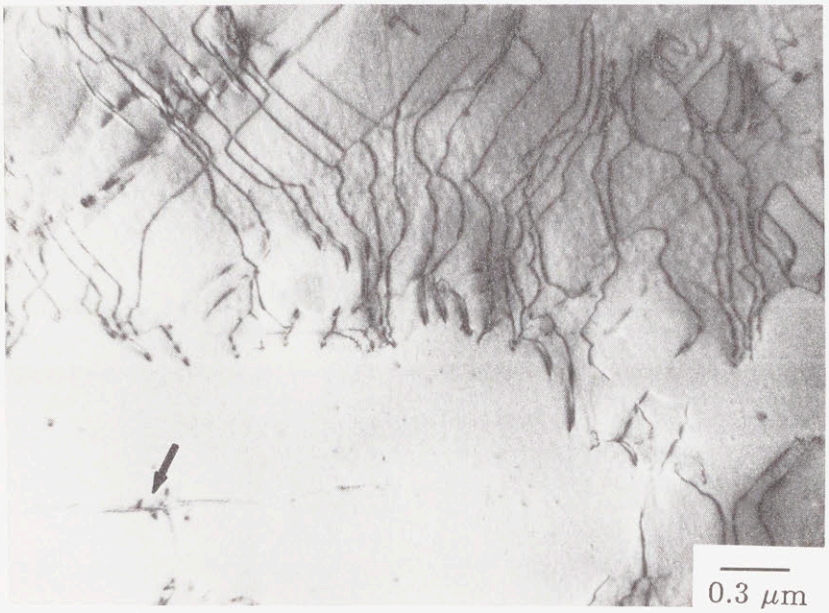

Figure 6.8 TEM micrograph of the rafted structure following creep at 1050°C and 50 MPa for 48 hours. Several dislocations are trapped at the interface of the rafting cuboids.

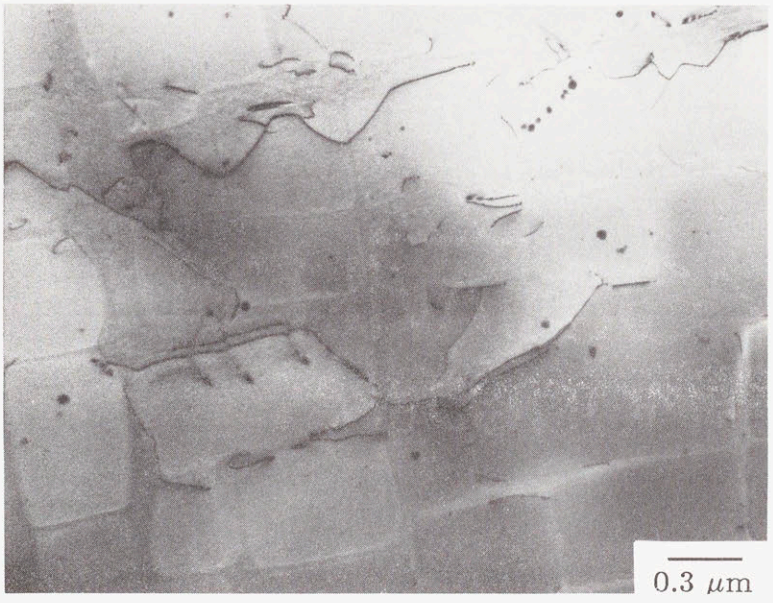

Figure 6.9 TEM micrograph of γ' precipitates in an "unrafted" area of a sample following creep at 1050°C and 50 MPa for 48 hours. Note the absence of creep dislocations in the general vicinity.

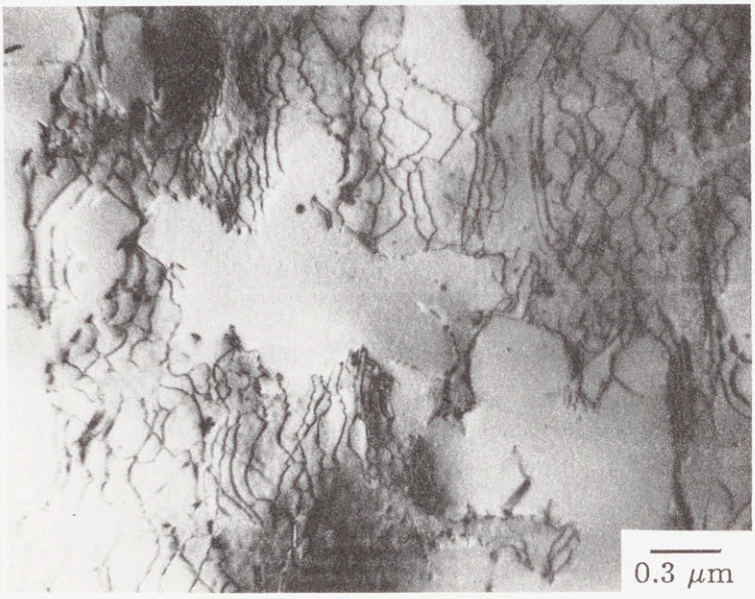

Figure 6.10 Rafted structure in a plane normal to the loading axis following creep at 1050°C and 50 MPa. The shape of the rafts is irregular in this plane.

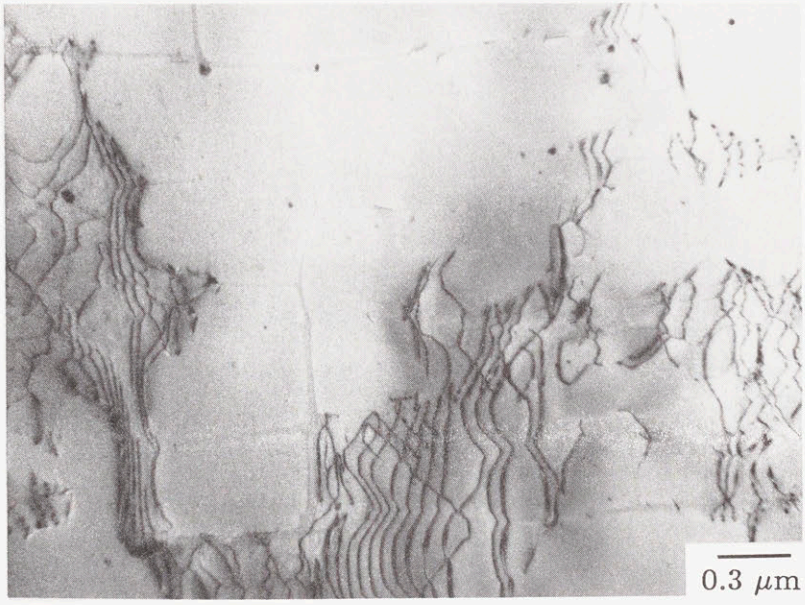

Figure 6.11 TEM micrograph of rafted structure in a sample following creep at 1050°C and 50 MPa for 48 hours. Note the absence of dislocations at the merging γ' interfaces, indicating that the misfit has not been relieved.

the face of the plate near the center of the micrograph appears to be much like the irregular shape shown in SEM micrographs of the rafted structure in the plane normal to the loading axis for IN100 [22]. Again in Figure 6.11 there appears to be a large rafted area extending through the foil thickness. Looking closely at this micrograph, it appears as though it has formed by the merging of γ' cubes which have retained their original shape, as defined by the thin layers of matrix material still present between the precipitates. Again as in the previous micrographs, creep dislocations are found adjacent to the large rafts. It should also be noted that there are very few or no dislocations contained in the matrix material between the merging cuboids.

6.3 Rafting in Positive Misfit Crystals

Two experiments on the positive misfit alloy were done in tension at 1050°C, at stress levels of 50 and 150 MPa. In both cases the sample was held at temperature for an hour prior to loading to establish the equilibrium volume fraction of precipitates. In Figure 6.12 (a) and (b) the precipitate distribution in the shoulder of the sample is compared to that in the reduced section of the sample, subjected to 50 MPa. A creep strain of 1.4×10^{-3} has accumulated after 68 hours at 1050°C. Comparing these micrographs, there is occasional linking of 2 to 3 precipitates in the stressed section of the sample in a direction *parallel* to the loading direction. Figure 6.13 makes the same comparison for a sample undergoing creep at 1050°C and 150 MPa. The linking of the γ' precipitates is now more noticeable, and again they are joining in a direction parallel to the loading direction, which is opposite of the case of the negative misfit material. The creep curve for this test is in Figure 6.14. A very large amount of primary creep preceded the establishment of a steady state where the steady state creep rate was 7.7×10^{-9}/s. The rafts established in this case are obviously much less regular than those seen in the negative misfit alloy.

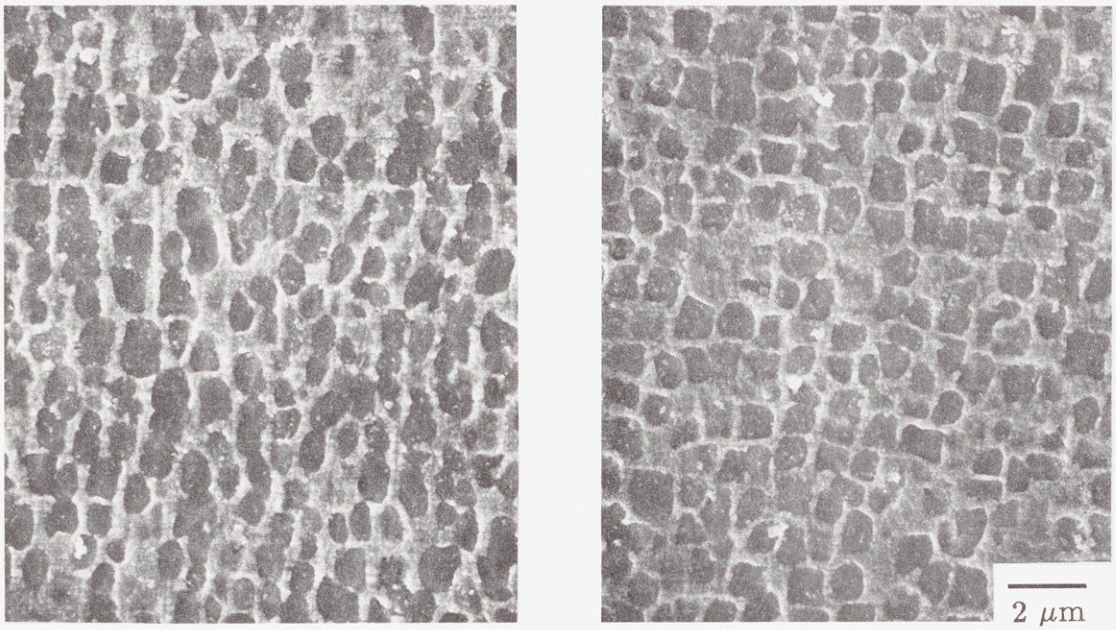

(a) (b)

Figure 6.12 Precipitates in a sample of PMA following creep at 1050°C and 50 MPa for 68 hours. Precipitates in the gauge section are shown in (a) and an area from the specimen shoulder is shown for comparison in (b). Tension axis is vertical.

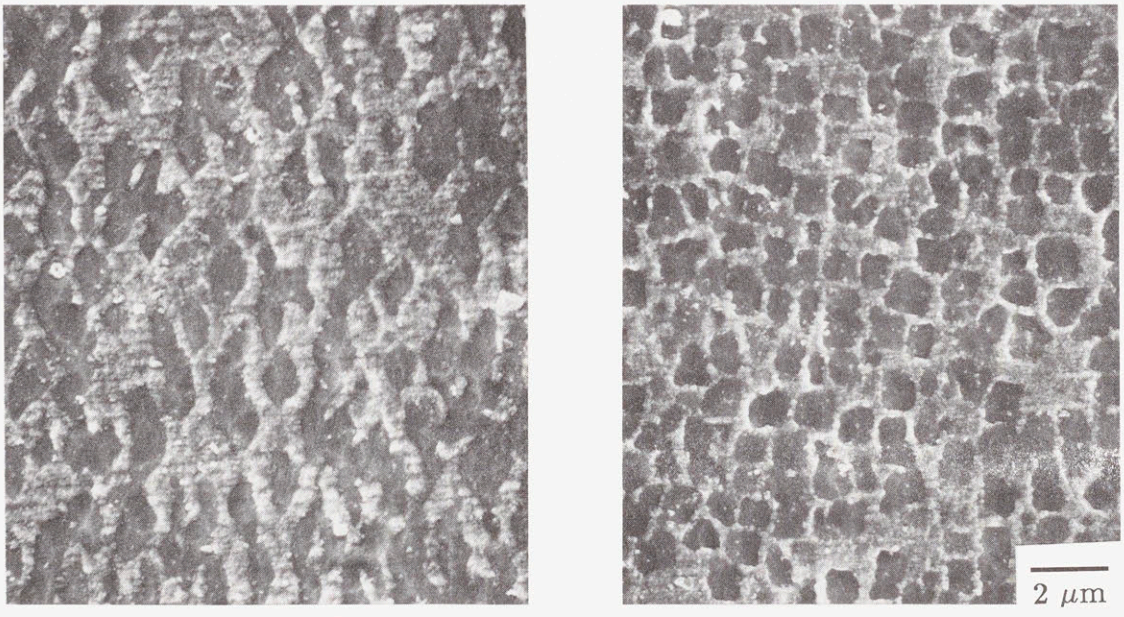

(a) (b)

Figure 6.13 Precipitates in a sample of PMA following creep at 1050°C and 150 MPa. Precipitates in the gauge section are shown in (a) and for comparison an area from the shoulder of the sample is shown in (b). Tension axis is vertical.

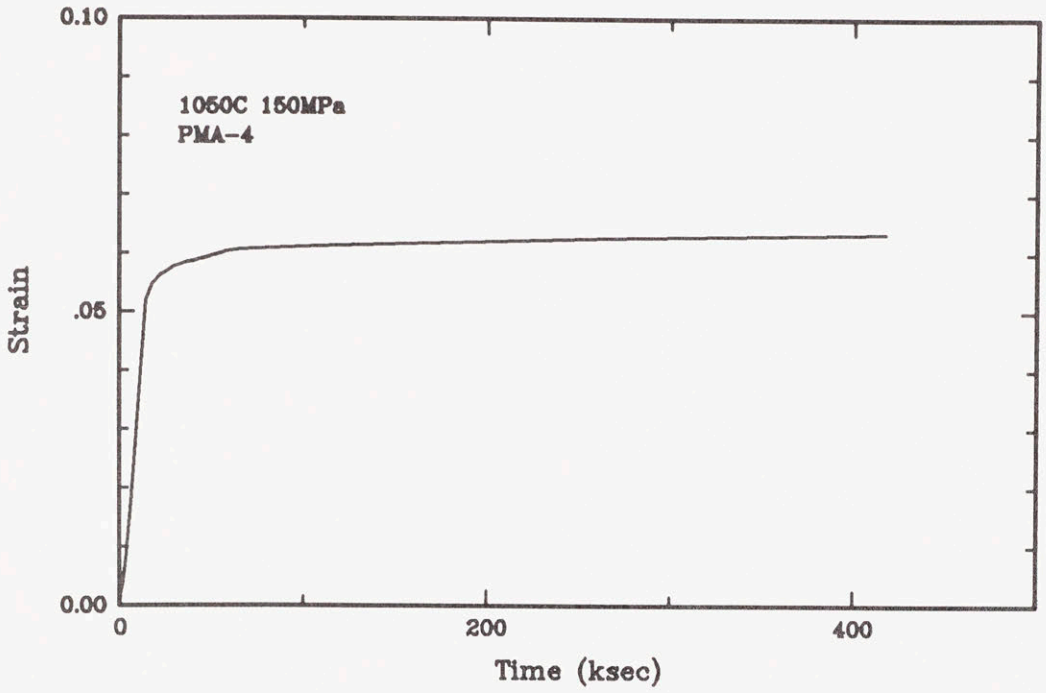

Figure 6.14 Creep curve for the PMA alloy at 1050°C and 150 MPa.

6.4 Discussion

For creep testing in tension, the positive and negative misfit alloys develop rafts which are parallel and normal to the direction of the applied stress, respectively. If the rafting process were a bulk flow process set up by pressure gradients in the matrix material (shown by the finite element analysis) it would be expected that the rafts would develop normal to the axis of the applied stress regardless of the sense of misfit, since the misfit is relieved early in the creep process. This is experimentally shown here not to be the case. In fact, the misfit is not relieved by the creep dislocations in the places where the rafts are developing, as is clear in Figures 6.10 and 6.11. Since the misfit is not relieved as the rafts are formed, the possibility of directional flow of material due to the fact that the misfit is relieved on some faces of the precipitate and "aggravated" on others, as proposed by Carry and Strudel [33] could not be responsible for promoting the rafting process. It thus appears that the driving force for the direction of alignment of the rafts is reduction of the elastic energy due to the sense of the misfit. An elastic model should then be able to answer the question of what is the most favorable orientation for a misfitting raft (an assemblage of individual precipitates which have joined together). The elastic calculations using the Eshelby approach do appear to be able to answer this question, but an exact numerical calculation which makes no assumptions with respect to elastic isotropy, shape or distribution of the precipitates would be a better confirmation of this. The reduction of elastic energy is certainly not the only driving force, since the merging of the precipitates eliminates significant amount of γ/γ' interfacial energy. The shape changes here appear to occur by a merging of cubes which are not changing their shape to any great degree, rather than a classical coarsening process where a single precipitate grows larger at the expense of smaller ones.

The larger problem is then in determining how this process of merging occurs. By simply removing matrix material from vertical passages and replacing it in horizontal passages, thereby allowing two γ' precipitates to merge, would require a strain of about 11%. On the other hand, rafts are experimentally observed to be well developed after as little as 0.5% strain. Apparently the application of stress at high temperatures promotes some instability which allows the rafting to be accomplished in an inhomogeneous manner. The role of the creep dislocations in this process is not clear, since some plastic flow always accompanies the development of the rafts. The geometric and kinetic aspects of this problem will obviously require much more attention before a complete understanding of the rafting process is developed.

Chapter Seven

DISCUSSION AND CONCLUSIONS

7.1 The γ' Precipitates

Detailed TEM stereo observations of dislocation arrangements during creep have shown that creep deformation is confined to the γ matrix phase unless very high stresses are imposed on the material, as in the compression tests. The resistance of the γ' precipitates to shearing during the creep process is key to the development of the exceptional creep resistance shown by these two phase single crystal materials. Here it has been shown that the precipitates resist deformation during creep at applied stresses as high as 552 MPa. This is in contrast to the single phase Ni_3Al material which will deform rapidly at these stresses at 850°C. In a recent study [64] the creep properties of single crystals of Ni_3Al alloyed with Cr, Ti, W, Mo and Co (so that their composition would resemble the composition of γ' in two phase nickel base alloys) were established at 900°C. At the slightly lower temperature of 850°C these γ' single crystals would have a creep resistance of 150 MPa for a reference strain rate of 2.5×10^{-8}/sec. At this rate in the two phase CMSX-3 material, the precipitates remain undeformed. One of the important differences between the bulk material and the precipitates in the two phase material is one of scale. In the bulk material there are initially dislocations present and there is no unusual constraint on spreading the dislocations through the single phase material. But in the two phase material there are only isolated domains of Ni_3Al material which are all dislocation-free. In order to deform the γ' it is necessary to

initiate the deformation by pushing a dislocation or pair of dislocations into the ordered precipitate from the surrounding γ phase. Once in the precipitate, the dislocation or pair of dislocations will presumably easily cross the precipitate, but then pass back into the matrix material, and the difficult process of pushing the dislocations into the precipitate must be repeated. A calculation for the stress required to push a single dislocation or pair of dislocations into a precipitate will follow.

The activation energy required for penetration of a pair of dislocations into the γ' under the influence of an applied shear stress τ, assuming an activated configuration of the dislocations as shown in Figure 7.1(a) is:

$$\Delta G = \mathcal{E}_{sd}(2R\theta) - \mathcal{E}_{2d}(L) - 2\tau bR^2(\theta - \frac{sin2\theta}{2}) \tag{1}$$

where R and θ relate to the geometry of the bowing dislocations as shown in Figure 7.1 (a), and $\mathcal{E}_{sd}$ and $\mathcal{E}_{2d}$ are the energies per unit length, respectively, of the superdislocation in the γ' and the two edge dislocations pushed up against the interface before entering the γ'. These energies are:

$$\mathcal{E}_{sd} = \frac{\mu b^2}{2\pi(1-\nu)}\left[2ln\frac{R'}{r} - ln\frac{\Delta}{er} - \frac{2+\nu}{6}ln\frac{\delta}{er}\right]$$

$$\mathcal{E}_{2d} = \frac{\mu b^2}{2\pi(1-\nu)}\left[ln\frac{R'}{r} + ln\frac{R'}{\xi} - \frac{2+\nu}{6}ln\frac{\delta}{er}\right]$$

where δ is the equilibrium stacking fault width, Δ is the equilibrium antiphase boundary width, ln(e)=1, and ξ is the stress dependent equilibrium separation between the two dislocations (of the same Burgers vector) at the interface. All other terms have their usual meaning. The energy of the superdislocation is given assuming that the equilibrium APB separation is greater than the stacking fault separation; only an interaction between the two unextended dislocations is included. This seems to be a reasonable assumption since in most superalloys the partial dislocations cannot be

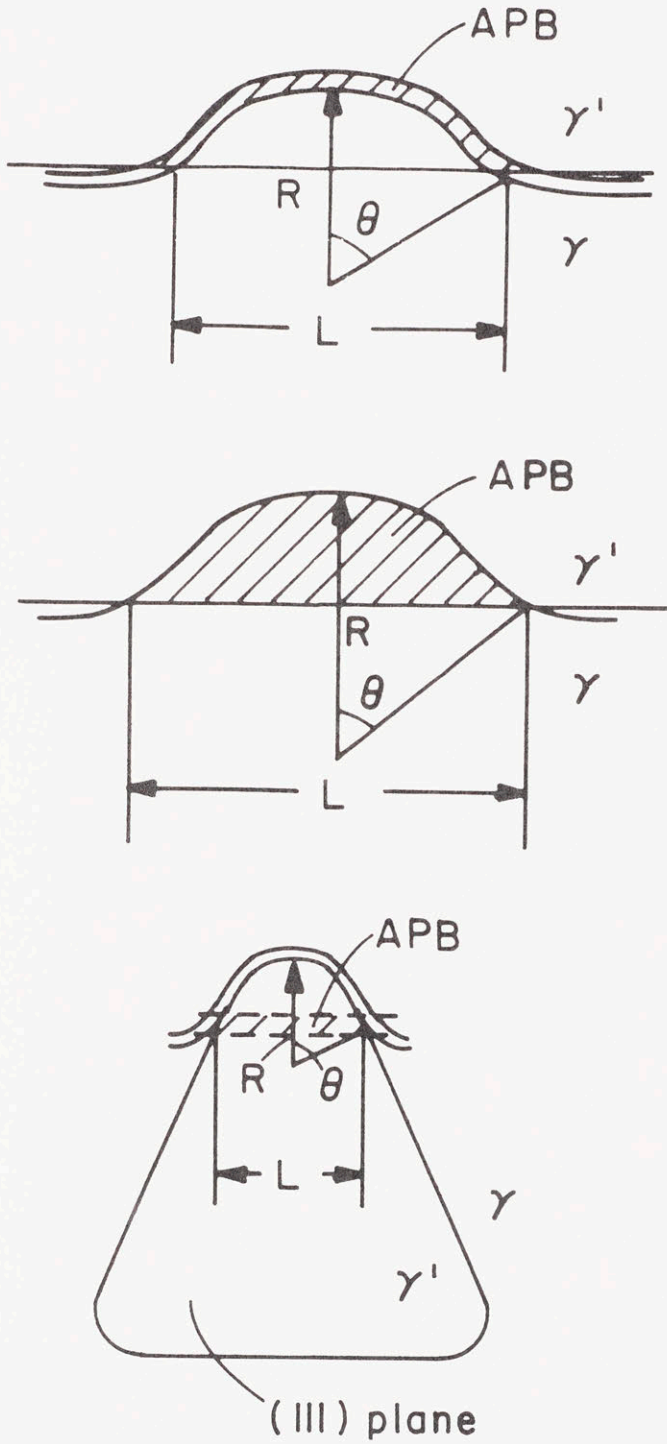

Figure 7.1 Configurations for penetration of dislocations into the γ'. In (a) two dislocations enter at a flat interface, in (b) a single dislocation penetrates leaving a continuous APB and in (c) two dislocations initially wrapped around the corner of a precipitate on a {111} plane enter the γ'.

resolved by weak beam microscopy, while the APB coupled pairs are easily resolved [76,77]. However, for this reason, an accurate measurement of the stacking fault energy of CMSX-3 is not available. Assuming that the partial separation is just at the limit of the resolution of the weak beam technique, a stacking fault energy of 90 mJ/m^2 would be a reasonable estimate. This is about 30% lower than the stacking fault energy of pure nickel, and gives δ = 1.5nm. The APB energy for Ni_3Al has been reported by Veyessiere [78] to be 111 mJ/m^2, giving Δ = 6.9 nm. Other values used are μ=48.2 GPa, ν=0.33, b=0.254 nm.

The mechanical threshold stress τ_s, or the stress at which the precipitates are sheared with no thermal assistance is determined by evaluating equation (1) for various values of the applied stress until the level at which there is no energy barrier is determined. It is necessary to do this numerically because the estimate of a small angles of bowing, θ, which would normally be employed is not generally valid for the case of pushing a pair of dislocations into a small precipitate. The results at various stress levels for R=50 nm are shown in Figure 7.2. In the plots of ΔG as a function of L, for a given R, there is a minimum θ and therefore L, below which only the first dislocation will have penetrated into the precipitate. For this reason in the plot for R=50 nm, L has a minimum value not equal to zero. As can be seen in Figure 7.2, τ_s for the configuration assumed here is 444 MPa. If the local stresses in the microstructure were the same as the applied stress, then a uniaxial stress of 1088 MPa would cause shearing of the precipitates by pairs of dislocations. Figure 7.3 shows the mechanical threshold stress as a function of R. Obviously the critical penetration stress decreases with increasing R. But as R increases it is necessary for L to increase also. In a practical sense R and L will be influenced by the dislocation configurations in the matrix. If the dislocations are tied into a network, an additional stress for pulling the

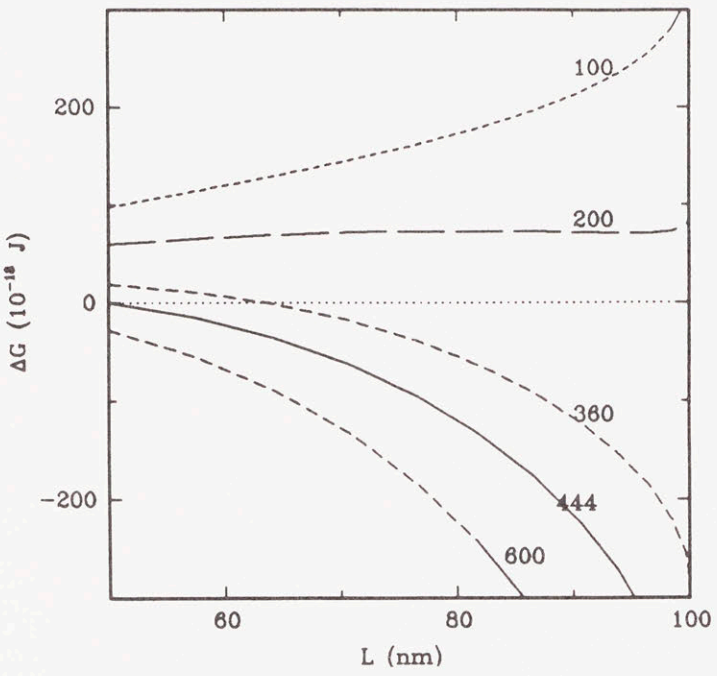

Figure 7.2 Energy required for penetration of a pair of dislocations into the γ' as a function of initial length of the activated pair, plotted for varying levels of applied τ (MPa). This is for configuration 7.1 (a) with R=50nm.

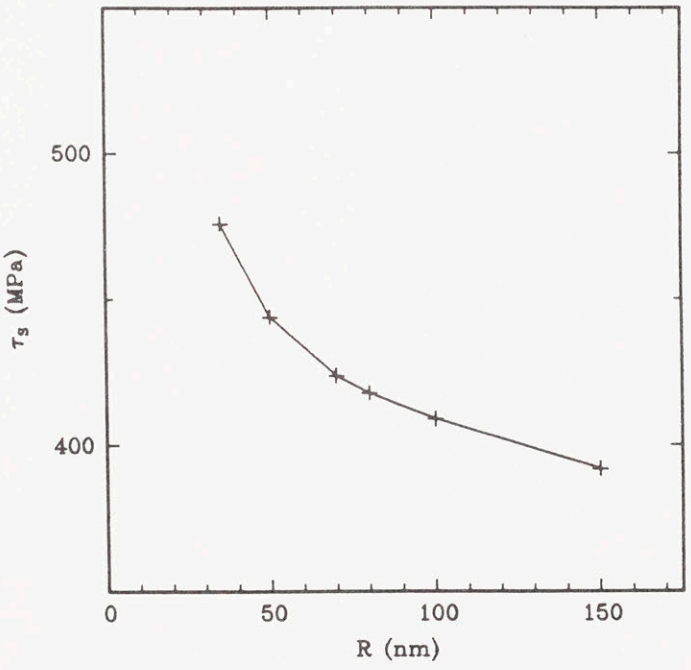

Figure 7.3 Athermal shearing stress for dislocations entering the γ' as shown in Figure 7.1(a), as function of bowout radius, R.

dislocations out of the network will be needed if the length of the activated dislocations is longer than the spacing of the dislocations in the network. Here it is assumed that R will be of the order of the network spacing of 50-80 nm, leading to stresses of 418 to 444 MPa for pushing the dislocations into the γ'.

For comparison, the stress for the penetration of a *single* dislocation into the precipitate has also been calculated. The energy required for nucleation of a single dislocation into the γ' per the geometry of 7.1(b) is:

$$\Delta G = \mathcal{E}_d(2R\theta - L) + (\chi_{APB} - \tau b)R^2(\theta - \frac{sin2\theta}{2}) \qquad (2)$$

where χ_{APB} is the antiphase boundary energy, and $\mathcal{E}_d$ is the energy per unit length of a single extended edge dislocation:

$$\mathcal{E}_d = \frac{\mu b^2}{4\pi(1-\nu)} ln\left(\frac{R}{r}\right) - \frac{\mu b^2(2+\nu)}{24\pi(1-\nu)} ln\left(\frac{\delta}{er}\right)$$

In this case there is continuous creation of APB as the dislocation moves along. For that reason the dislocation may penetrate and travel only a short distance, as seen for τ = 530 MPa in Figure 7.4, where ΔG becomes positive around L=97nm, or as the leading edge of the dislocation reaches approximately 48nm into the precipitate. The stress at which the single dislocation will shear through the precipitate is 600 MPa. These simple calculations confirm the experimental observation that pairs of dislocations will shear the γ' more easily than single dislocations may do so.

Referring now to Figure 7.1(c), it is also possible that the dislocations may become wrapped around the corner of the precipitate on a {111} plane. Entry into the γ' from the corner would initially decrease the line length, and consequently it might be expected that a lower stress would be required. In this case the change in energy would be:

$$\Delta G = \mathcal{E}_{sd}(2Rsin\theta) - \mathcal{E}_{2d}(2R\theta) - 2\tau bR^2(\theta - \frac{sin2\theta}{2}) \qquad (3)$$

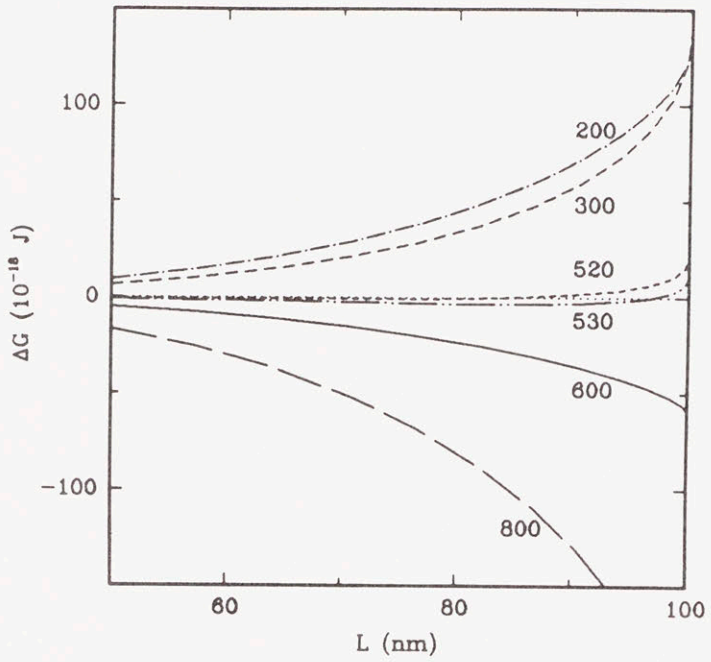

Figure 7.4 Energy required for penetration of a single dislocation into the γ' as a function of initial length of the dislocation at the interface, plotted for varying levels of applied τ (MPa). This is for configuration 7.1 (b) with R=50nm.

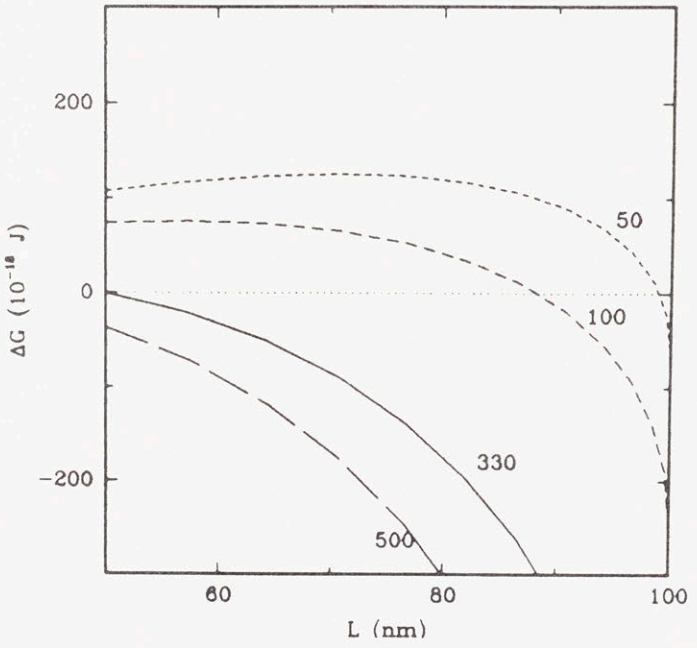

Figure 7.5 Energy required for penetration of a pair of dislocations into the γ' as a function of initial length of the activated pair, plotted for varying levels of applied τ (MPa). This is for configuration 7.1 (c) with R=50nm.

All symbols have the same meaning as earlier. From a series of micrographs of the aged material it was determined that the average radius of curvature at the the precipitate corner is 50 nm. Figure 7.5 shows that a stress of only 330 MPa is required for a pair of dislocations to enter the precipitate at the corner. Normalized by the Schmid factor, a stress of 809 MPa is required.

Referring back to the finite element contour plots of equivalent stresses in the γ' (Figure 5.5), the stresses at the corner of the precipitate reach 800 MPa after about 4.3×10^5 seconds. The stresses at the flat portion of the interface just below the corner reach the level of 1000 MPa shortly after this. The creep curve at 850°C and 552 MPa (Figure 3.1) interestingly shows upward curvature beginning at about 5×10^5 seconds, and it seems possible that the shearing of the precipitates contributes to the acceleration. It has also been shown here by TEM that dislocations are more frequently found in the precipitates in these later stages of creep.

To summarize, it will be energetically favorable for pairs of dislocations rather than individual dislocations to shear the γ'. If the stresses in the precipitates were uniform, then entry into the precipitates would be preferred at the corners, but since there is a stress concentration just below the corner of the precipitate, dislocations may enter at the corner or just below the corner with about equal ease during creep. The precipitates will not be sheared until the stresses rise to the necessary level, and this occurs in the later stages of "steady state" creep and during tertiary creep. Comparison with the results of the finite element analysis shows that the stresses in the precipitate reach the level required for shearing at about the time when the creep rate begins to accelerate, and it is likely that γ' shearing contributes in part to the long, gradually accelerating tertiary transient.

7.2 The Incubation Period

Another interesting aspect of the creep deformation problem in nickel base single crystals is the "incubation" which precedes the primary creep transient. The micrographs in Chapter Four clearly show that since the initial microstructure contains so few dislocations, and since the precipitates are effective barriers to easy spreading of dislocations, a finite amount of time is required to bow dislocations out through the matrix material. As noted in Chapter One these incubations have been reported in several other single crystal alloys under varying low and high temperature conditions, but the reason for their presence or absence has not been clear.

Before macroscopic creep deformation can be detected, some dislocations must penetrate through the cross-section of the sample. TEM micrographs of the dislocation structures present during the incubation in the sample which was tested at 825°C and 450 MPa for 120 seconds clearly show that the deformation has not progressed this far. However, some useful information about the process of spreading the dislocations through the matrix may be extracted from these micrographs.

Before the dislocations can be forced through the matrix channels, the applied stresses must be high enough to overcome the Orowan resistance, the misfit stresses, and the solid solution drag. The finite element analysis showed that there are compressive misfit stresses of 433 MPa in the planes of the interfaces, and low (50 MPa) tensile stresses normal to the interface. With the application of a uniaxial stress in the range of 450 - 552 MPa, one component of misfit in the vertical matrix channels (parallel to the applied stress) is completely relieved, while in the channels normal to the applied stress, neither component of the misfit is relieved, leading to very high equivalent stresses in these horizontal channels. With an applied stress of 450 MPa (the same stress applied to the sample from which the incubation micrographs were taken), the equivalent stress in the vertical channels is 468 MPa, and the equivalent

stresses in the horizontal channels is 934 MPa. It might be expected that the dislocations would move along in the horizontal matrix channels more easily than in the vertical channels. In the incubation micrographs this appears to be true. The horizontal matrix channels lie in the plane of the micrograph, and the long, narrow loops are contained in the horizontal gaps. Looking closely it is obvious that very few dislocations are threading vertically through the foil. In addition, the dislocations which are spreading into the vertical gaps that are encountered as a loop moves through a horizontal gap (producing "bumps" on the otherwise staight lines) have traveled only a short distance into the vertical gaps relative to the motion of the leading segment in the horizontal gap.

Viewing the incubation micrographs in stereo, it also appears that the dislocations are moving through the channels in a somewhat viscous manner. Very few of the bowing out segments are held up at the interfaces; instead they have been captured in the state of slowly moving along through the matrix. It is not unlikely that in this heavily alloyed matrix material that there are solid solution drag forces acting on the dislocations as they move through the channels.

From the information contained in the micrographs of the incubation sample, which was tested at 825°C and 450 MPa for 120 seconds, an estimate of the drag coefficient can be made. In Figure 7.6 marked by an arrow adjacent to an area of grown-in dislocations is a dislocation which has bowed out in a vertical channel. The channel diameter is 100 nm and the dislocation has bowed out through a distance of 200 nm. This particular dislocation was chosen because there was no complicating factors of cross-slip or a combined path through several vertical and horizontal channels. In the channel the temperature dependent drag force is balanced by the local resolved shear stress which is in excess of the Orowan stress:

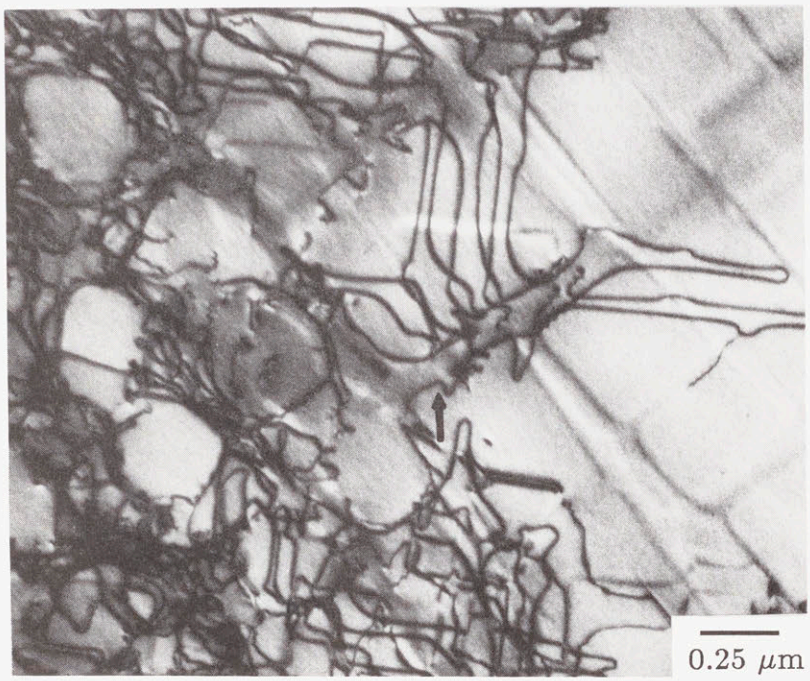

Figure 7.6 Dislocations bowing out from the grown-in dislocation network during the incubation period at 825°C and 450 MPa. The arrow marks a dislocation which is slowly moving through a vertical matrix gap (out of the plane of the micrograph).

$$B(T)v = (\tau - \tau_{OR})b \tag{4}$$

B(T) is the temperature dependent drag coefficient, v is the dislocation velocity, τ is the local resolved shear stress (including the misfit), τ_{OR} is the Orowan stress, and b is the Burgers vector. For the indicated dislocation, the average velocity would have been 1.67 nm/sec, τ=191 MPa, and τ_{OR}=87 MPa. This gives B(T)=(191-87)(0.254)/(1.67)=15.8 MPa-s. From this, a rough estimate of the length of the incubation at 850°C and 552 MPa may be obtained. Using the experimentally measured activation energy of 658 kJ/mol and B(T)=Bexp(Q/RT) gives B(850°C) =0.784. The length of the incubation will then be the amount of time to send dislocations a distance of 50μm, which is about half the distance across the presumably dislocation free areas (d/2) outlined by the dendrite arms in the lighter regions of Figure 2.1. Since deformation proceeds more easily in the horizontal channels it will develop in a fairly planar manner with dislocations winding through horizontal channels, which are on average 60 nm in diameter, under a stress of τ=419 MPa. The incubation time will then be approximately:

$$t_{inc} = \frac{B(T)(d/2)}{(\tau - \tau_{OR})b} = \frac{(0.784MPa \cdot s)(50\mu m)}{(419MPa - 144MPa)(0.254nm)} = 560seconds \tag{5}$$

This is reasonably close to the experimentally observed average value of 600 seconds. In addition it would predict an incubation of 112 seconds at 900°C. In the 900°C experiment no incubation was observed, but it is experimentally very difficult to detect short incubations due to slight thermal transients on loading.

Here there is no apparent physical significance which can be attached to the strong temperature dependence of the length of the incubation period and too few incubation observations have been made to determine if the above stress dependence is valid. A greater number of experiments on the incubation behavior would be necessary to

make more detailed conclusions about the incubation process. It is clear however that the incubation period arises because of the "slow" filling of the matrix by creep dislocations.

7.3 Deformation During Primary and Steady State Creep

During the primary creep transient dislocations continue to fill the matrix material by bowing between the γ' precipitates on $\{111\}$ planes. The common feature of the material during the early stages of primary creep is the presence of $a/2< 110 >$ dislocations at the γ/γ' interfaces lying at angles of 45^o to the cuboid edges. These are mixed dislocations, with Burgers vectors at 60^o to the line direction. During the early stages of the transient areas are locally filled with dislocations of a single $a/2< 110 >$ Burgers vector, but as the end of the transient is approached, dislocations with other Burgers vectors interpenetrate, leading to reactions, and preventing signifigant crystallographic rotations. The majority of the dislocations have Burgers vectors of the stressed slip systems, but reactions between these primary dislocations produces some $a/2[110]$ and $a/2[\bar{1}10]$ dislocations. The operation of multiple slip systems and uniform filling of the matrix material by Orowan bowing of the dislocations efficiently hardens the material and gives a relatively short primary creep transient with small primary creep strains.

The steady state dislocation structure is characterized by a three-dimensional network of dislocations which fills the matrix material. Locally the network is composed of dislocations with three different Burgers vectors. The network is somewhat irregular, with dislocation spacings and arrangements varying from channel to channel. This is likely to be due to the fact that it was formed from creep dislocations as they penetrated into individual channels. A large fraction of the dislocations which form the network are associated with the γ/γ' interfaces, which are not planar and clearly

defined as they were in primary creep. Assuming that the dislocations which are associated with the interfaces during steady state creep are still 60° dislocations, and resolving their edge components into the interfaces, a dislocation spacing in the range of 42 to 67 nm would be required to relieve a misfit in the range of -0.19% to -.305% (at 850°C the misfit of CMSX-3 is in this range). The actual spacing observed during steady state creep is in the range 50 to 120 nm, so it appears that the misfit between the phases is largely relieved. The observed dislocation spacings increase to 80 - 100 nm and are more regularly distributed after 750 hours of annealing at 850°C. However, since the networks which actually develop during steady state creep are so irregular it is likely that although the spacings indicate that the misfit could be relieved, there are local areas in the material where it is not relieved. The development of a limited amount of "linking" of the precipitates after long periods of creep at 850°C indicates that the misfit is probably not entirely relieved.

7.4 Creep Resistance of the γ/γ' Material

It is clear that nickel base alloys show exceptional resistance to creep deformation. A comparison of the bulk creep properties of the constituent phases demonstrates this fact. At 850°C for a reference rate of 2.5×10^{-8}/s a Ni-6W solid solution alloy will support a stress of 30 - 40 MPa [62], and a solid solution material designed to resemble the matrix composition of a typical single crystal alloy [64] also gives a resistance of approximately 30 MPa. Extrapolating data from slightly higher temperatures, pure Ni_3Al may support 60 - 70 MPa [63], and Ni_3Al alloyed so that its composition corresponds to that often found for γ' precipitates gives a bulk creep resistance of the as high as 150 MPa [64]. Under the same conditions, the creep resistance of CMSX-3 is 552 MPa, which is more than an order of magnitude higher than the bulk matrix creep resistance.

The TEM stereo observations reveal the reasons for the above differences. All of the dislocations which serve as sources for the creep dislocations lie in the matrix. High temperature solution and aging treatments give a very regular distribution of γ' precipitates which are free of dislocations and isolated from their neighbors by thin continuous layers (60 nm in this case) of Ni solid solution material. Since there are initially no dislocations inside the γ' precipitates and the stresses required to push dislocations into them comfortably exceeds the stresses for pushing dislocations through the matrix, a very creep resistant configuration is formed.

For the CMSX-3 single crystals investigated here, the Orowan stress for bowing the precipitates through the narrow matrix channels gives a uniaxial creep resistance of at least 388 MPa. Compared to the bulk creep resistance of the matrix material, this stress supported in the γ/γ' system is an order of magnitude higher. In fact, since the precipitates do not deform and the deformation is forced through these narrow channels, there is no reason to expect that the properties of the creeping matrix material would resemble the bulk creep properties. Certainly there is some amount of solid solution resistance to motion of dislocations through the matrix material, but this will only be a fraction of the overall resistance in the two phase alloy, while it is a very important component of the strength in the single phase material. Furthermore, in the bulk material the characteristic creep properties are determined by the buildup of a steady state structure which consists of well organized subgrains which occupy dimensions much larger than the matrix dimensions in the two phase alloy. In the γ/γ' material the dislocations bow out and fill the material during the early stages of creep. As the density of dislocations increases in the local matrix channels there are reactions between the dislocations and a space-filling three dimensional nodal network is developed.

The finite element analysis also clearly demonstrates the fact the this two phase deformation problem is not a simple problem of the two phase creep resistance being determined only by the bulk properties of the deforming (matrix) phase, since the load supported is far short of what is experimentally observed. The finite element analysis does however illuminate the effect of deformation occuring only in narrow matrix channels. Since the deforming matrix channels are contained between non-deforming precipitates which are coherent (or at least semi-coherent) there is frictional constraint to the thickening of the horizontal channels and thinning of the vertical channels, leading to the buildup of pressure gradients. These pressure gradients provide extra load support. Also, since the precipitates are not deforming, they become incresingly stressed as creep process in the matrix continues. This provides an explanation for the experimental observation that precipitates are observed to occasionally be sheared in the later stages of "steady state" creep, but not in the early stages following the primary transient.

Finally, the overall creep resistance is determined by a combination of the above factors; first the forced Orowan bowing of the dislocations with some additional solid solution resistance to the motion of these dislocations. Also, the pressure gradients which build as a result of the constraint of the precipitates on flow in the narrow rectangular channels contribute to the total resistance.

These facts indicate that optimum creep resistance should be attained in a microstructure which exhibits the smallest (and therefore most closely spaced) cuboidal precipitates possible. In the extreme limit the Orowan stress should be just below the stress for shearing the precipitates. Considering that the precipitates may be sheared at the corners at 330 MPa, for a volume fraction of 0.70 and an Orowan stress of 330 MPa, the highest strength microstucture would have 0.20μm cubes with 26 nm

diameter channels. Practically, the precipitates are usually spherical when they are this small, so then the most creep resistant microstructure would contain the smallest achievable cuboidal precipitates. This appears to be experimentally confirmed by the observations of Khan [10, 31], where he finds optimum creep resistance for cuboidal γ' precipitates 0.5μm in diameter. If the cuboidal precipitates are larger, then the creep resistance is lowered, and if the precipitates are smaller, they are no longer cuboidal in shape and the creep resistance is again lowered. For this reason the aging treatment which establishes the final γ' size and shape is critical in determining the creep properties.

7.5 Recovery

In order to construct a meaningful constitutive model for the creep process it is first necessary to understand the details of the mechanisms which govern the recovery processes. In the case of nickel base single crystals under the conditions studied here, there must be certainly be some critical rearrangements of the dislocations contained in the matrix for maintenance of the steady state creep process.

Direct and indirect methods of studying the recovery processes have been pursued. Following the establishment of steady state creep, a sample was unloaded and held at creep temperature to permit time for static (diffusion controlled) processes to proceed. Reloading transients after extended recovery periods were so slight that they were difficult to even measure, indicating that diffusional processes under no stress were ineffective in causing dislocation rearrangements in the matrix. In-situ annealing experiments also show few important rearrangements of the matrix dislocations at temperatures of 850°C or lower. The in-situ observations do indicate that static recovery may be important at temperatures above about 900°C, which interestingly is also the temperature range where the precipitates begin to raft at noticeable rates.

Considering the stability of the three dimensional networks which build up during creep at low to intermediate temperatures, and also the lack of "extra" dislocations in the structure, it is probably not too suprising that static recovery is ineffective in promoting further creep deformation. For this reason, the few models which are available for the creep process at these temperatures are inadequate in their assumption of diffusion controlled climb of long, free segments of dislocations around γ' precipitates. In addition, the very high creep stress exponents and activation energies for creep observed in nickel base alloys offer no support for these kinds of diffusion controlled creep at lower temperatures. Instead it appears that a more detailed model which includes a stress assisted dynamic recovery mechanism where dislocations mutually cancel in local areas of the channels is necessary in formulating a realistic model of the steady state creep process.

7.6 Conclusions

- The incubation periods observed prior to the onset of measurable creep deformation in nickel base single crystals are present because of the difficulty of spreading dislocations from widely spaced sources through the sample cross section. The sources of creep dislocations are networks of grown-in dislocations associated with the interdendritic areas of the crystal.

- The stress required for pushing a pair of dislocations into the ordered γ' precipitates is relatively high, and as a result the precipitates are effective barriers to creep deformation. Only in the later stages of creep, after several percent of creep deformation has accumulated in the matrix are the precipitates stressed highly enough that they are deformed.

- Since the precipitates do not deform, creep is only possible by bowing dislocations through the narrow matrix channels. The process of bowing the dislocations through the matrix gaps is responsible for a large portion of the creep resistance of the two phase γ/γ' material.

- The total creep resistance of the single crystals in the temperature regime below 900°C where the shape of the preciptates is relatively stable, arises from the Orowan resistance to bowing, solid solution resistance, and pressure gradients caused by the frictional constraint of the precipitates. As a result the optimum microstructure should have a large volume fraction of small closely spaced cuboidal precipitates.

- The dislocation structure during steady state creep consists of a three dimensional nodal network with few free dislocations. This configuration is very stable

and resistant to static recovery processes. For this reason at temperatures around 850^0C or lower, steady state creep must be maintained by a stress-dependent dynamic recovery process.

- At temperatures in excess of about 950°C the precipitates are unstable in shape and merge to form "rafts". The rafting process is apparently assisted by the presence of dislocations in the structure, but experiments on positive misfit crystals with high volume fractions of γ' confirm that the driving forces are the reduction of elastic and γ/γ' interfacial energy.

REFERENCES

1. A. Kaufman, and G.R. Halford, NASA TM 83577, (1984).

2. R.L. McKnight, J.H. Laflen, and G.T. Spamer, *Turbine Blade Tip Durability Analysis*, NASA Report 165268, (1982).

3. M.V. Nathal, Metall. Trans. **18A**, (1987), 1961.

4. A.A. Hopgood and J.W. Martin, Mater. Sci. Engng. **82**, (1986), 27.

5. G.R. Leverant and B.H. Kear, Metall. Trans. **1A**, (1970), 491.

6. B.H. Kear and J.M. Oblak, J. de Physique, **12**, (1974), 7.

7. M.V. Nathal, R.A. MacKay and R.V. Miner, Metall. Trans. **20A**, (1989), 133.

8. D.D. Pearson, F.D. Lemkey, and B.H. Kear, *Superalloys 1980*, American Society for Metals, (1980), 513.

9. M.V. Nathal and L.J. Ebert, Metall. Trans. **16A**, (1985), 1863.

10. P. Caron and T. Khan, Mater. Sci. Engng. **61**, (1983), 173.

11. R.A. MacKay and L.J. Ebert, Metall. Trans. **16A**, (1985), 1969.

12. M.V. Nathal and L.J. Ebert, Scripta Metall. **17**, (1983), 1151.

13. C. Carry and J.L. Strudel, Acta Metall. **26**, (1978), 859.

14. R. A. Stevens and P.E.J. Flewitt, Acta Metall. **29**, (1981), 867.

15. B.F. Dyson and M. McLean, Acta Metall. **31**, (1983), 17.

16. G.A. Webster and B.J. Piearcy, Metal Science J. **1**, (1967), 97.

17. W.L. Kimmerle and J.K. Tien, Scripta Metall. **21**, (1987), 1553.

18. P. Caron and T. Khan, Proc. 7th Intl. Conf. on *Strength of Metals and Alloys*, Pergamon Press, (1986), 683.

19. R.A. MacKay and L.J. Ebert, *Superalloys 1984*, ed. by M. Gell et.al., The Metallurgical Society of AIME, (1984), 135.

20. G.R. Leverant and D.N. Duhl, Metall. Trans. **2A**, (1971), 907.

21. M.V. Nathal and L.J. Ebert, Metall. Trans **16A**, (1985), 427.

22. K. Yu, Ph.D. Thesis, MIT, (1985).

23. P.J. Henderson and M. McLean, Scripta Metall. **19**, (1985), 99.

24. C.C. Law and M.J. Blackburn, Metall. Trans. **11A**, (1980), 495.

25. G. Jianting, D. Ranucci, E. Picco, and P.M. Strocchi, Metall. Trans. **14A**, (1983), 2329.

26. J.P. Dennison, P.D. Holmes, and B. Wilshire, Mater. Sci. Engng. **33**, (1978), 35.

27. R.E. Hoffman, P.W. Pickus, and R.A. Ward, Trans. AIME **206**, (1956), 483.

28. O.D. Sherby and A.K. Miller, ASME J. Mat. Tech., **101**, (1979), 387.

29. S. Takeuchi and A.S. Argon, J. Mat. Sci. **11**, (1976), 1542. .

30. A.F. Giamei, Final Tech. Report, AFOSR FR-12637, (1979).

31. T. Khan, *High Temperature Alloys for Gas Turbines and Other Applications 1986* ed. by W. Betz et. al., D. Reidel Publishing, (1986), 1395.

32. R.A. MacKay, R.L. Dreshfield, and R.D. Maier, *Superalloys 1980*, American Society for Metals, (1980), 385.

33. C. Carry and J.L. Strudel Acta Metall. **25**, (1977), 767.

34. A.F. Giamei, AFOSR report FR-11009.

35. P.J. Henderson and M. McLean, Acta Metall. **31**, (1983), 1203.

36. A. Fredholm and J.L. Strudel, *Superalloys 1984*, ed. by M. Gell et. al., The Metallurgical Society of AIME, (1984), 211.

37. M.V. Nathal and L.J. Ebert , Metall. Trans. **16A**, (1985), 1849.

38. R.A. MacKay and L.J. Ebert, Scripta Metall. **17**, (1983), 1217.

39. T. Khan, P. Caron, and C. Duret, *Superalloys 1984*, ed. by M. Gell, et. al., Metallurgical Society of AIME, (1984), 145.

40. J.E. Bird , A.K. Mukherjee, and J.E. Dorn, in *Quantitative Relationships Between Properties and Microstructure*, ed. by D.G. Brandon and A. Rosen, Israel Univ. Press, (1969), 255.

41. J. Weertman, Trans. ASM **61**, (1968), 681.

42. R. Langeborg, Metal Sci. J., **3**, (1969), 161.

43. J.H. Gittus, Acta Metall. **22**, (1974), 789.

44. M. McLean, Proc. Roy. Soc. London, **A371**, (1980), 279.

45. J. Weertman, Proc Intl. Conf. on *Creep and Fracture of Engineering Materials*, ed. B. Wilshire and D.R.J. Owen, Pineridge Press, Swansea, (1984), 1.

46. A.S. Argon and A.K. Bhattacharya, Acta Metall. **35**, (1987), 1499.

47. A.S. Argon and S. Takeuchi, Acta Metall. **29**, (1981), 1877.

48. W.D. Nix, J.C. Gibeling, and D.A. Hughes, Metall. Trans. **16A**, (1985), 2215.

49. G. Nelmes and B. Wilshire, Scripta Metall. **10**, (1976), 697.

50. P.W. Davies, G. Nelmes, K.R. Williams and B. Wilshire, Metal Sci. J., **7**, (1973), 87.

51. J. Friedel, *Dislocations*, Pergamon Press, (1964), 239.

52. J.C. Gibeling and W.D. Nix, Mater. Sci. Engng. **45**, (1980), 123.

53. A.M. Brown and M.F. Ashby, Scripta Metall. **14**, (1980), 1297.

54. W.J. Evans and G.F. Harrison, Metal Sci. J. **10**, (1979), 641.

55. J.K. Tien and S.M. Copley, Metall. Trans. **2A**, (1971), 543.

56. T. Miyazaki, K. Nakamura, and H. Mori, J. Mat. Sci. **14**, (1979), 1827.

57. S. Chakravorty, H. Hashim, and D.R.F. West, J. Mat. Sci. **20**, (1985), 2313.

58. J. Conley, Ph.D. Thesis, Northwestern Univerity, (1987).

59. A.F. Giamei, D.D. Pearson and D.L. Anton, Vol. 39, Proc. MRS Symp. on *High Temperature Intermetallic Ordered Alloys*, MRS, (1985), 293.

60. D. Lahrmann, R. Field, R. Darolia, and H. Fraser, Acta Metall. **36**, (1988), 1309.

61. A. Pineau, Acta Metall. **24**, (1976), 559.

62. W.R. Johnson, C.R. Barrett, and W.D. Nix, Metall. Trans. **3A**, (1972), 963.

63. D.M. Shah, Scripta Metall. **17**, (1983), 997.

64. M.V. Nathal, J.O. Diaz, and R.V. Miner, to be published in Proc. MRS Symp. on Intermetallic Alloys, (1988).

65. D.M. Shah, and D.H. Duhl, *Superalloys 1984*, ed. by M. Gell et.al., The Metallurgical Society of AIME, (1984), 105.

66. G.R. Leverant, B.H. Kear and J.M. Oblak, Metall. Trans. **4A**, (1973), 355.

67. F. Prinz, A.S. Argon, and W.C. Moffatt, Acta Metall. **30**, (1982), 821.

68. G. Simmons and H. Wang, *Single Crystal Elastic Constants and Calculated Aggregate Properties*, MIT Press, (1971).

69. Private Communication, Allison Gas Turbine Division of the General Motors Corporation.

70. L. Curwick, Ph.D. Thesis, University of Minnesota, (1972).

71. D.A. Grose and G.S. Ansell, Metall. Trans. **12A**, (1981), 1631.

72. W. Schroeder and D.A. Webster, J. Appl. Mech., (1949), p.289.

73. K. Hemker and W.D. Nix, to be published in Proc. MRS Symp. on Intermetallic Alloys, (1988).

74. M.F. Ashby and L.M. Brown, Phil. Mag. **8**, (1963), 1083.

75. M.V. Nathal, R.A. MacKay, and R.G. Garlick, Mater. Sci. and Engng. **75**, (1985), 195.

76. A. Huis in't Veld, G. Boom, P.M. Bronsveld, J. Th. M. De Hosson, Scripta Metall. **19**, (1985), 105.

77. P. Veyssiere, D.L. Guan, J. Rabier, Phil. Mag. **49A**, (1984), 45.

78. J. Douin, P. Veyssiere, P. Beauchamp, Phil. Mag. **54A**, (1986), 375.

LIST OF TABLES

Table		Page
Table 1.1	Experimentally measured creep parameters for a variety of high volume fraction γ' nickel base alloys.	16
Table 2.1	Nominal chemical composition of CMSX-3	39
Table 2.2	Chemical composition of the matrix phase in CMSX-2 (10).	40
Table 2.3	Chemical composition of the γ' in CMSX-2 (10).	40
Table 3.1	Experimental test conditions and results for creep in CMSX-3 single crystals.	46
Table 6.1	Summary of CMSX-3 rafting experiments and observations.	104

LIST OF FIGURES

Figure		Page
Figure 1.1	Creep curves for < 001 > single crystal alloys. 1 - SRR99, 750°C and 800 MPa (4) 2 - Mar-M-200, 760°C and 690 MPa (5) 3 - Mar-M-200, 855°C and 415 MPa (6) 4 - NASAIR 100, 760°C and 793 MPa (7) 5 - Ni-13Al-9Mo-2Ta, 1038°C and 207 MPa (8)	 14
Figure 1.2	Small strain creep curves for < 001 > single crystals. A - Mar-M-200, 760°C and 689 MPa (5) B - Alloy B, 1000°C and 207 MPa (9) C - CMSX-2, 760°C and 750 MPa (10) D - Alloy E, 1000°C and 207 MPa (9)	 17
Figure 2.1	(a) Low magnification micrograph of CMSX-3 solution treated bar. Section transverse to the growth direction. (b) Longitudinal section of CMSX-3 solution treated bar.	 38
Figure 2.2	Heating stage temperature calibration.	 38
Figure 3.1	Full creep curve for < 001 > CMSX-3 at 850°C and 552 MPa. Fracture at 273 hours.	 47
Figure 3.2	Activation energy for creep in CMSX-3 at 552 MPa.	 47
Figure 3.3	Small strain creep behavior of CMSX-3. Note the change in time scale for the 800°C data.	 49
Figure 3.4	Reloading transient following a 90% load reduction during steady state creep.	 50
Figure 3.5	Stress jump during steady state creep from 552 to 607 MPa.	 51
Figure 3.6	Stress drop from 607 MPa back to the original 552 MPa.	 51
Figure 3.7	Transient behavior immediately following the stress jump from 552 to 607 MPa.	 52
Figure 3.8	Recovery period following the stress drop from 607 MPa back to the original 552 MPa.	 52

Figure 3.9 Comparison of the transients for the 552 to 607 MPa stress jump (a), and primary creep at 552 MPa (b). 53

Figure 3.10 Constant true strain rate compression test at 800°C. 54

Figure 3.11 Compression strain rate jump test at 800°C. 54

Figure 4.1 TEM micrograph of the γ/γ' structure of the aged single crystal CMSX-3 material. 57

Figure 4.2 Network of "grown-in" dislocations in the aged material. 57

Figure 4.3 Dislocations spreading from the grown-in dislocation network during the incubation period. The network is at the center and the arrows denote the leading screw components of the expanding loops. 59

Figure 4.4 Long, narrow dislocation loops spreading through the matrix during the incubation period. These dislocations originated from the network in the upper left corner. 59

Figure 4.5(a) Schematic of the details of the cross-slipping matrix dislocations corresponding to area (B). 60

Figure 4.5(b) Cross-slipping matrix dislocations during the incubation period. A bowing out screw segment has progressed from (A) to (C) cross slipping at (B) from the $(1\bar{1}1)$ plane to the (111) plane. 60

Figure 4.6 Primary creep dislocation structure after 35 minutes of creep, $\varepsilon = 4.6\text{x}10^{-4}$. These dislocations all have the same Burgers vector of b=a/2 [011]. 62

Figure 4.7 Primary creep dislocation distribution after 402 minutes, $\varepsilon = 0.001$. Dislocations with a second Burgers vector are beginning to penetrate locally at the arrow. 62

Figure 4.8(a) One of two sets of interpenetrating primary creep dislocations in the matrix material. The arrow marks a common reference point. 63

Figure 4.8(b) The second set of the locally interpenetrating dislocations. The arrow marks the common reference point. 63

Figure 4.9 Stereo pair of dislocation structure during primary creep. Dislocations to the left of (A) are in a vertical matrix gap. The precipitate at (A) extends through the foil. The dislocations in region (B) are in a horizontal matrix gap which is contained in the plane of the thin foil. 64

Figure 4.10 Schematic of matrix dislocation arrangements. 65
(a) Dislocations bowing through vertical matrix channels. This is similar to the arrangement in region (A) in Figure 4.9.
(b) Dislocations bowing through horizontal matrix passages. This is similar to the arrangement in region (B) in Figure 4.9.

Figure 4.11 Stereo pair of the steady state dislocation structure showing all of the dislocations residing in the matrix material. 67

Figure 4.12 Matrix dislocation networks during steady state creep. A very organized three dimensional nodal network is present in the matrix in this particular area. 68

Figure 4.13 A region of locally high matrix dislocation density during steady state creep. The three dimensional network here is much less "organized" compared to other regions. 68

Figure 4.14 A precipitate sheared by dislocations in the later stages of steady state creep. 70

Figure 4.15 Dislocations in the γ' precipitates in a sample tested to fracture at 850°C. In the light areas the precipitates extend through the thickness of the foil, and all the isolated dislocations in these areas are in the γ'. 70

Figure 4.16 Recovered dislocation networks following 750 hours of bulk static annealing at 850°C. The dislocations are largely associated with the γ/γ' interfaces. 71

Figure 4.17 Recovered dislocation networks following 750 hours of bulk static annealing at 850°C. Locally, the networks contain three sets of dislocations. In the area marked by the arrows multiple diffraction conditions show the three sets of dislocations. In this area the dislocations are associated with the γ/γ' interface. 72

Figure 4.18 Shearing of the γ' precipitates as a result of compression at a rate of 1.1×10^{-4}/s at 800°C. Stacking faults which extend across the precipitates are created by dislocations shearing the γ' on multiple {111} planes. 74

Figure 4.19 (a) Dislocation structure at the start of the 853°C in-situ annealing experiment. 77

Figure 4.19 (b) Dislocation structure after 30 minutes at 853°C. 77

Figure 4.20 (a) Dislocation structure at the start of the 845°C in-situ annealing experiment. 78

Figure 4.20 (b) Dislocation structure after 17 minutes at 845°C. 78

Figure 4.20 (c) Dislocation structure after 845°C for 45 minutes and 882°C for 31 minutes. 79

Figure 4.21 Dislocation densities during the 845 and 882°C in-situ annealing experiment. 79

Figure 5.1 Finite element mesh of the γ/γ' problem. The shaded area corresponds to the matrix material. 83

Figure 5.2 Pressure gradients (MPa) in the matrix material during steady state creep. 87

Figure 5.3 Equivalent stress contours (MPa) for the matrix material during steady creep, $t=2.4 \times 10^5$ sec. 87

Figure 5.4 Displaced view of the finite element mesh. 89

Figure 5.5 Contours of equivalent stress in the precipitate at times of (a) 1.1×10^5 sec, (b) 4.3×10^5 sec, (c) 7.7×10^5 sec. 90

Figure 5.6 Comparison of normalized presssure gradients in the horizontal matrix channel for (a) the finite element analysis and (b) the Schroeder and Webster solution. The results are plotted as the fractional distance from the center of the channel, with x/L=1.0 representing the outer edge, and x/L=0 the center. 92

Figure 5.7 Displaced plot of the two material disk during steady creep. 92

Figure 6.1 PMA alloy showing cuboidal γ' precipitates following solution treatment. 99

Figure 6.2 Precipitate morphology in CMSX-3 after 8 hours of creep at 850°C and 552 MPa. Tension axis is vertical. 101

Figure 6.3 Precipitate morphology in CMSX-3 after 114 hours of creep at 850°C and 552 MPa. Tension axis is vertical. 101

Figure 6.4 γ' precipitates (dark) in CMSX-3 after 950°C and 95 MPa for 158 hours. Tension axis is vertical. 102

Figure 6.5 TEM micrograph of isolated dislocations after 950°C and 95 MPa for 158 hours. Tension axis is normal to the plane of the micrograph. 102

Figure 6.6 γ' precipitates following creep at 1050°C and 50 MPa for 48 hours. Tension axis is vertical. 105

Figure 6.7 γ' precipitates following creep at 1050°C and 50 MPa for 48 hours. Tension axis is vertical. 105

Figure 6.8 TEM micrograph of the rafted structure following creep at 1050°C and 50 MPa for 48 hours. Several dislocations are trapped at the interface of the rafting cuboids. 106

Figure 6.9 TEM micrograph of γ' precipitates in an "unrafted" area of a sample following creep at 1050°C and 50 MPa for 48 hours. Note the absence of creep dislocations in the general vicinity. 106

Figure 6.10 Rafted structure in a plane normal to the loading axis following creep at 1050°C and 50 MPa. The shape of the rafts is irregular in this plane. 107

Figure 6.11 TEM micrograph of rafted structure in a sample following creep at 1050°C and 50 MPa for 48 hours. Note the absence of dislocations at the merging γ' interfaces, indicating that the misfit has not been relieved. 107

Figure 6.12 Precipitates in a sample of PMA following creep at 1050°C and 50 MPa for 68 hours. Precipitates in the gauge section are shown in (a) and an area from the specimen shoulder is shown for comparison in (b). Tension axis is vertical. 109

Figure 6.13 Precipitates in a sample of PMA following creep at 1050°C and 150 MPa. Precipitates in the gauge section are shown in (a) and for comparsion an area from the shoulder of the sample is shown in (b). Tension axis is vertical. 109

Figure 6.14 Creep curve for the PMA alloy at 1050°C and 150 MPa. 110

Figure 7.1 Configurations for penetration of dislocations into the γ'. In (a) two dislocations enter at a flat interface, in (b) a single dislocation penetrates leaving a continuous APB and in (c) two dislocations initially wrapped around the corner of a precipitate on a $\{111\}$ plane enter the γ'. 115

Figure 7.2 Energy required for penetration of a pair of dislocations into the γ' as a function of initial length of the activated pair, plotted for varying levels of applied τ (MPa). This is for configuration 7.1 (a) with R=50nm. 117

Figure 7.3 Athermal shearing stress for dislocations entering the γ' as shown in Figure 7.1(a), as function of bowout radius, R. 117

Figure 7.4 Energy required for penetration of a single dislocation into the γ' as a function of initial length of the dislocation at the interface, plotted for varying levels of applied τ (MPa). This is for configuration 7.1 (b) with R=50nm. 119

Figure 7.5 Energy required for penetration of a pair of dislocations into the γ' as a function of initial length of the activated pair, plotted for varying levels of applied τ (MPa). This is for configuration 7.1 (c) with R=50nm. 119

Figure 7.6 Dislocations bowing out from the grown-in dislocation network during the incubation period at 825°C and 450 MPa. The arrow marks a dislocation which is slowly moving through a vertical matrix gap (out of the plane of the micrograph). 123

Appendix A

List of Alloy Compositions

Table A1.1 Nickel base superalloy compositions (weight percent).

Material	Cr	Co	C	Mo	W	Nb	Ti	Al	Ta	Hf	Zr	Other	Ni
CMSX-2	7.9	4.6		0.5	8.0		1.0	5.6	6.0				Bal
CMSX-3	7.9	4.6		0.5	8.0		1.0	5.6	6.0	0.1			Bal
NASAIR 100	9.2		.005	1.0	10.2		1.5	5.7	2.8				Bal
Mar-M-200	9.0	10.	.15		12.0	1.0	2.0	5.0			.05	.02B	Bal
SRR 99	8.5	5.0	.015		9.5		2.2	5.5	2.8				Bal
IN 738	16.	8.5	.17	1.7	2.6	0.9	3.4	3.4	1.7		.1	.01B	Bal
IN 792	12.4	9.0	.12	1.9	3.8		4.5	3.1	3.9		.1	.02B	Bal
IN 713	12.5		.12	4.2		2.0	0.8	6.1			.1	.01B	Bal
IN 100	10.0	15.	.18	3.0			4.7	5.5			.06	1.0V	Bal
Mar-M-246	9.0	10.	.15	2.5	10.		1.5	5.5	1.5		.05	.01B	Bal
Mar-M-247	8.4	10.	.15	0.7	10.		1.0	5.5	3.0	1.5	.05	.02B	Bal
PWA 1480	10.0	5.0			4.0		1.5	5.0	12.0				Bal
B6	15.4	19.6	.14		2.9	1.9	3.5	3.1	0.7	0.7	.06	.02B	Bal
MERL 76	12.3	17.9	.03	3.3		1.7	4.3	5.0		.74	.06	.02B	Bal
AF115	10.5	15.0	.15	2.8	6.0	1.8	3.9	3.9		2.1	.05	.02B	Bal
MXON	3.0	2.3		1.0	8.4			8.1	7.7				Bal
Alloy E	8.5	5.0		0.6	9.9		1.4	5.2	3.0				Bal

Appendix B

Creep Curves

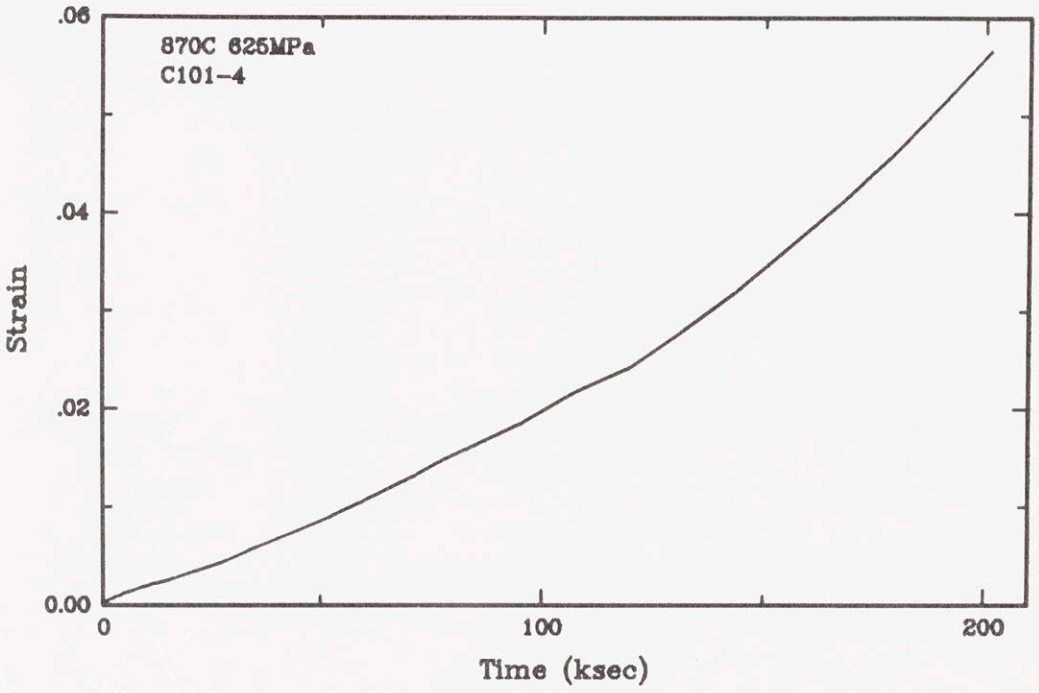
870C 625MPa
C101-4
.06
.04
.02
0.00
Strain
0
100
200
Time (ksec)

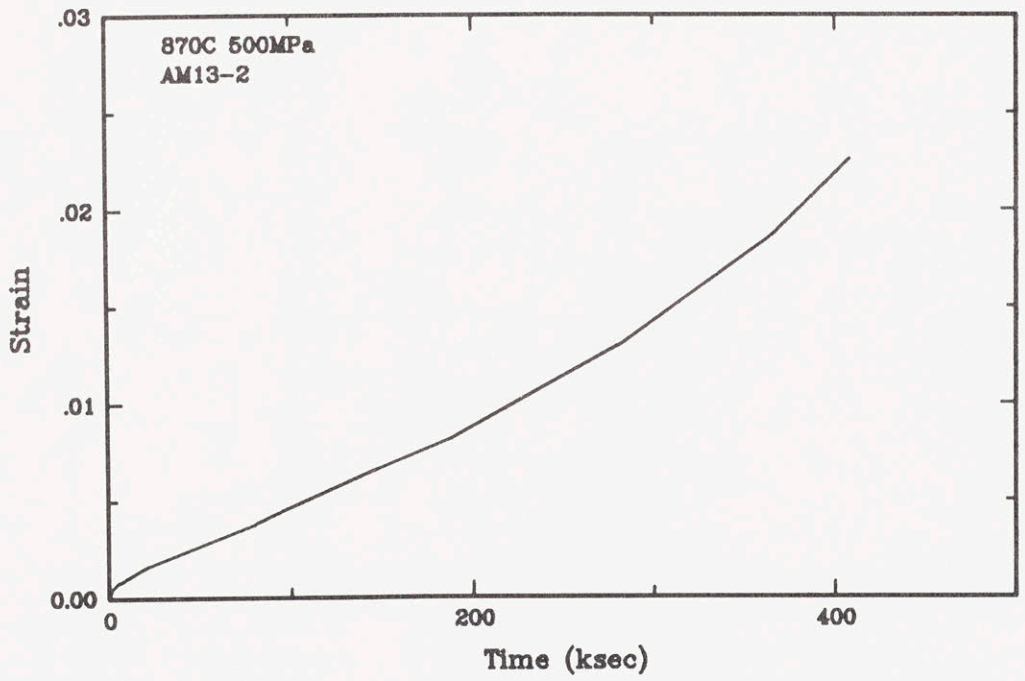
870C 500MPa
AM13-2
.03
.02
.01
0.00
Strain
0
200
400
Time (ksec)

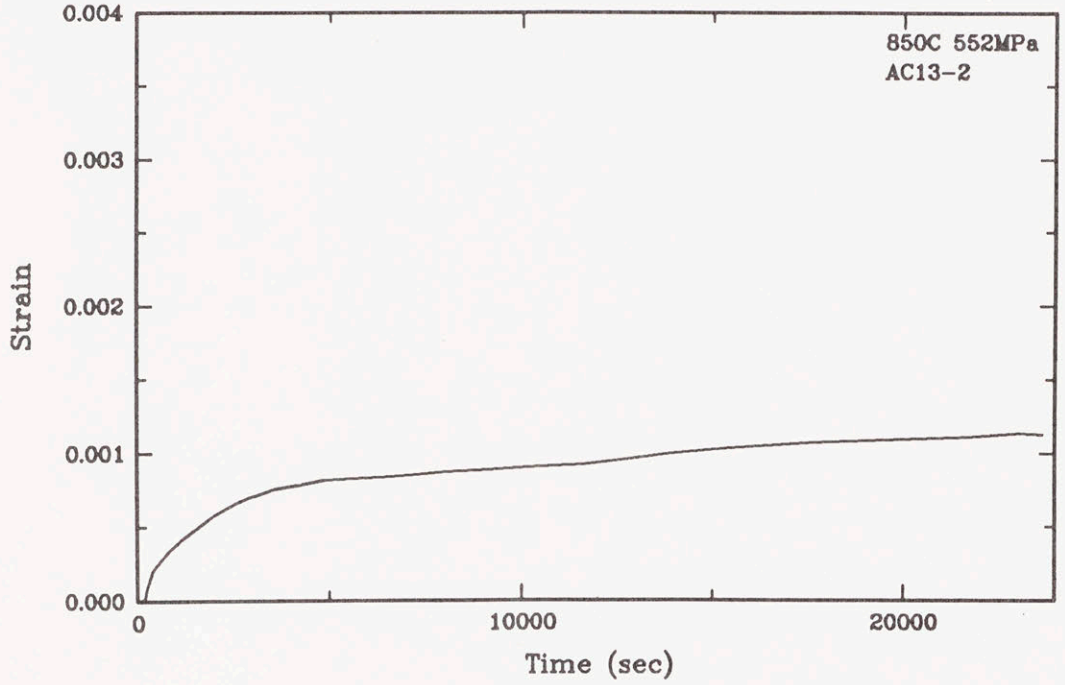
850C 552MPa
AC13-2
0.004
0.003
0.002
0.001
0.000
Strain
0
10000
20000
Time (sec)

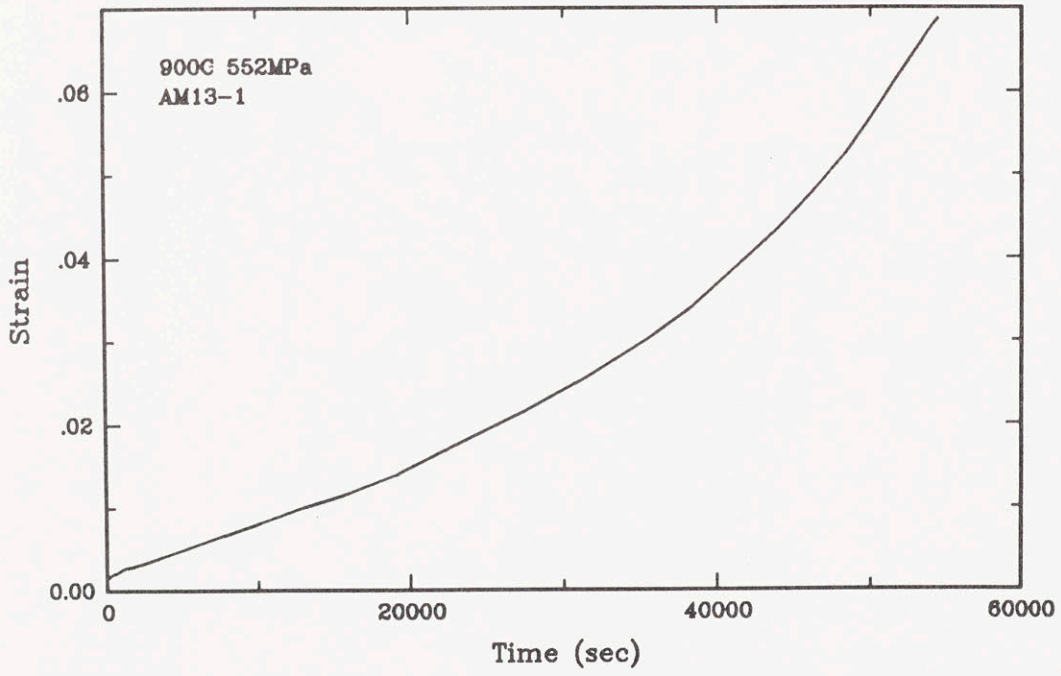
900C 552MPa
AM13-1
.06
.04
.02
0.00
Strain
0
20000
40000
60000
Time (sec)

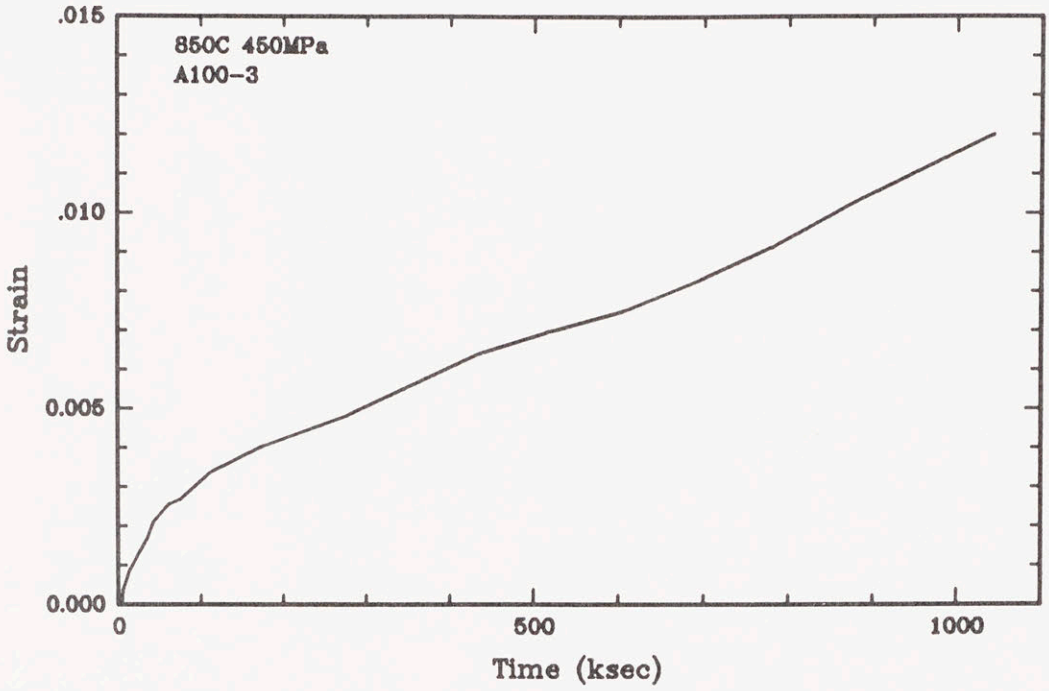
850C 450MPa
A100-3
.015
.010
0.005
0.000
Strain
0
500
1000
Time (ksec)

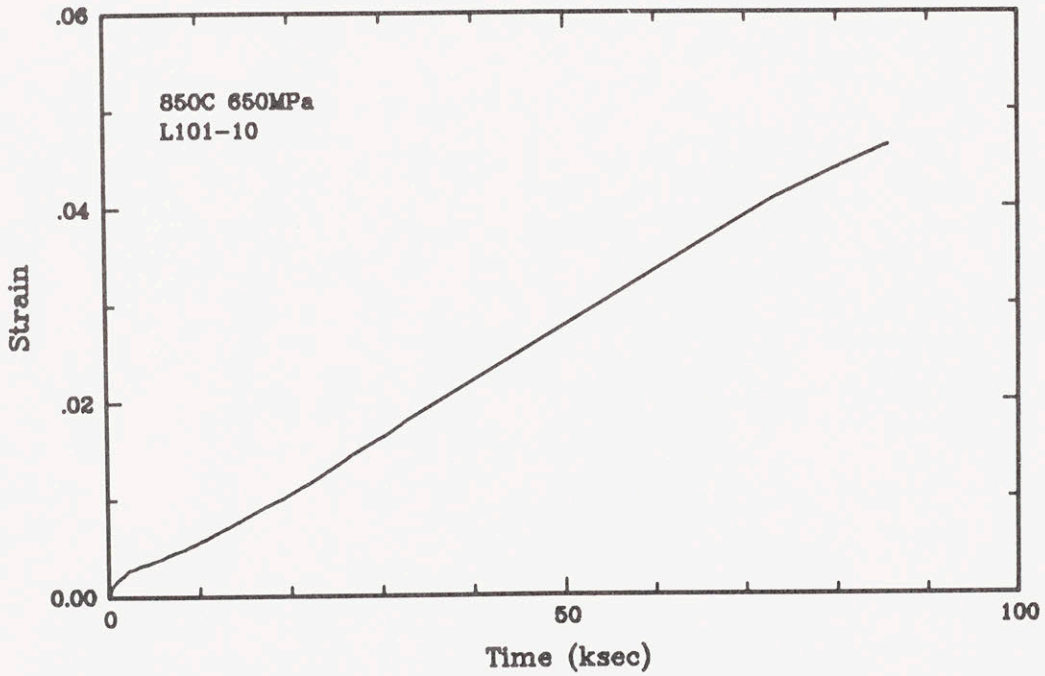
850C 650MPa
L101-10
.06
.04
.02
0.00
Strain
0
50
100
Time (ksec)

Appendix C

Finite Element Code

```
**********************************************************************************
** ABAQUS (Version 4.5) input for nickel base superalloy creep calculation
**********************************************************************************
*HEADING
CMSX-3 CREEP (SS,R-7/8/88)
**********************************************************************************
** Definition and generation of the nodes which will define the mesh.
**********************************************************************************
*NODE,NSET=ALL1
100,0.0,5.0
128,3.5,5.0
1100,0.0,4.0
1128,3.5,4.0
1228,3.5,3.875
1900,0.0,3.0
1928,3.5,3.0
1532,4.0,3.5
4300,0.0,0.0
4332,4.0,0.0
1144,3.875,3.875
1194,3.8125,3.8125
144,5.0,5.0
644,4.4375,4.4375
1260,3.875,3.5
160,5.0,3.5
1552,5.0,3.5
4352,5.0,0.0
1160,4.0,3.5
1330,3.60,3.75
1430,3.75,3.60
1332,3.75,3.75
152,5.0,4.12
156,5.0,3.8
140,4.5,5.0
136,4.12,5.0
132,3.8,5.0
148,5.0,4.5
98,0,0
99,0,5
*NGEN,NSET=ALL2
100,1100,100
128,1128,100
1100,4300,100
100,128
200,228,1
300,328
400,428
500,528
600,628
700,728
800,828
900,928
1000,1028
1100,1128
4300,4332
4332,4352,2
1128,4328,100
1200,1228
1300,1328
1400,1428
1500,1528
1532,4332,100
1528,1532
```

```
1528,4328,100
1529,4329,100
1530,4330,100
1531,4331,100
1700,1728,4
1900,1928,2
1526,4326,400
1524,4324,200
2700,2724,4
2300,2324,8
3100,3124,8
3900,3924,8
3500,3524,4
1532,1552,2
1532,4132,100
1534,4334,200
1536,4336,100
1538,4338,200
1540,4340,100
1542,4342,200
1544,4344,100
1546,4346,200
1548,4348,100
1550,4350,200
1552,4352,100
144,644,100
644,1144,100
160,1160,100
128,132
132,136
136,140
140,144
144,148
148,152
152,156
156,160
1328,1330
1330,1332
1332,1430,49
1430,1530,50
*NGEN,NSET=ALL3,LINE=C
328,360,2,1528
428,460,2,1528
528,560,2,1528
628,660,2,1528
728,760,2,1528
828,860,2,1528
928,960,2,1528
1028,1060,2,1528
1128,1160,2,1528
1228,1260,4,1528
*NGEN,NSET=ALL4
128,328,100
160,360,100
132,332,100
136,336,100
140,340,100
144,344,100
148,348,100
152,352,100
156,356,100
**********************************************************************
** Definition and generation of generalized plane strain elements.
```

```
**********************************************************************************
*ELEMENT, TYPE=CGPE10R
1,300,302,102,100,301,202,101,200,98,99
181,1300,1302,1102,1100,1301,1202,1101,1200,98,99
209,1528,1530,1332,1328,1529,1430,1330,1428,98,99
210,1728,1730,1530,1528,1729,1630,1529,1628,98,99
238,1900,1904,1504,1500,1902,1704,1502,1700,98,99
251,2700,2708,1908,1900,2704,2308,1904,2300,98,99
111,1732,1736,1536,1532,1734,1636,1534,1632,98,99
71,328,332,132,128,330,232,130,228,98,99
104,1128,1136,936,928,1132,1036,932,1028,98,99
105,1136,1140,940,936,1138,1040,938,1036,98,99
109,1532,1536,952,1152,1534,956,1052,1156,98,99
260,1328,1330,1136,1128,1329,1236,1132,1228,98,99
261,1330,1332,1144,1136,1331,1194,1140,1236,98,99
262,1430,1152,1144,1332,1252,1148,1194,1381,98,99
263,1530,1532,1152,1430,1531,1156,1252,1480,98,99
244,1924,1928,1528,1524,1926,1728,1526,1724,98,99
245,2324,2328,1928,1924,2326,2128,1926,2124,98,99
246,2724,2728,2328,2324,2726,2528,2326,2524,98,99
247,3124,3128,2728,2724,3126,2928,2726,2924,98,99
248,3524,3528,3128,3124,3526,3328,3126,3324,98,99
249,3924,3928,3528,3524,3926,3728,3526,3724,98,99
250,4324,4328,3928,3924,4326,4128,3926,4124,98,99
*ELGEN
1,14,2,1,5,200,14
181,14,2,1,2,200,14
238,7,4,1,1
111,5,4,1,14,200,5
251,3,8,1,3,800,3
71,8,4,1,4,200,8
105,4,4,1,1
210,2,2,1,14,200,2
**********************************************************************************
** Grouping of elements and nodes into sets for assigning material properties,
** applying loads and boundary conditions, and defining output.
**********************************************************************************
*NSET, NSET=LEFT,GENERATE
100,4300,100
*NSET, NSET=BOTTOM,GENERATE
4300,4352,1
*NSET, NSET=ALL
ALL1,ALL2,ALL3,ALL4
*NSET,NSET=TOP1,GENERATE
100,128
*NSET,NSET=TOP2,GENERATE
130,144,2
*NSET,NSET=TOP
TOP1,TOP2
*NSET,NSET=NOUT1
206,2308,521,3100,3108,3116,3124,3126
*NSET,NSET=NOUT2,GENERATE
3128,3152
*NSET,NSET=NOUT
100
*NSET,NSET=L
100
*NSET,NSET=L1
100,1540,4140
*ELSET,ELSET=BORDER1,GENERATE
1,14
*ELSET,ELSET=BORDER2
71,72,73,74
```

```
*ELSET,ELSET=BORDER
BORDER1,BORDER2
*ELSET,ELSET=ELOUT
32,44,148
**ELSET, ELSET=GAMMAP,GENERATE
**181,263
**ELSET, ELSET=GAMMA,GENERATE
**1,180
*ELSET,ELSET=GAMMAP1,GENERATE
181,263
*ELSET,ELSET=GAMMAP2,GENERATE
43,70
*ELSET,ELSET=GAMMAP3,GENERATE
95,112
*ELSET,ELSET=GAMMAP4
116,117,121,122,126,127,131,132,136,137,141,142,146,147,151,152
*ELSET,ELSET=GAMMAP5
161,162,166,167,171,172,176,177,156,157
*ELSET,ELSET=GAMMAP
GAMMAP1,GAMMAP2,GAMMAP3,GAMMAP4,GAMMAP5
*ELSET,ELSET=GAMMA1,GENERATE
1,42
*ELSET,ELSET=GAMMA2,GENERATE
71,94
*ELSET,ELSET=GAMMA3
113,114,115,118,119,120,123,124,125,128,129,130,133,134,135
*ELSET,ELSET=GAMMA4
143,144,145,148,149,150,153,154,155,158,159,160,163,164,165
*ELSET,ELSET=GAMMA5
173,174,175,178,179,180,138,139,140,168,169,170
*ELSET,ELSET=GAMMA
GAMMA1,GAMMA2,GAMMA3,GAMMA4,GAMMA5
*ELSET,ELSET=CORNER,GENERATE
71,110
*ELSET,ELSET=PR
32,148,44
*ELSET,ELSET=PLUS
260,261,262,263,209
*ELSET,ELSET=BIGCOR
PLUS,CORNER
*ELSET,ELSET=UP,GENERATE
1,70
**********************************************************************
** Material properties for the gamma and gamma prime materials.  The elastic
** constants are defined as E1111, E1122, E2222, E1133, E2233, E3333, E1212,
** E1313, E2323, Temperature (C).  The elastic constants are defined in units
** of  ksi.  The creep properties correspond to the creep properties of a
** Ni-W solid solution material.  The pre-exponent is in units of (sec)-1
**(ksi)-4.8.
**********************************************************************
*MATERIAL,ELSET=GAMMA
*ELASTIC, TYPE=ORTHO
34950.,22045.,34950.,22045.,22045.,34950.,18855.,18855.,
18855.,25.
30450.,20590.,30450.,20590.,20590.,30450.,14790.,14790.,
14790.,850.
*EXPANSION,ZERO=25.
1.63E-5,850.
*CREEP,LAW=STRAIN
5.7E-11,4.8,-0.001 ,850.
*MATERIAL,ELSET=GAMMAP
*ELASTIC, TYPE=ORTHO
32630.,20594.,32630.,20594.,20594.,32630.,17984.,17984.,
```

```
17980.,25.
27260.,18130.,27260.,18130.,18130.,27260.,13780.,13780.,
13780.,850.
*EXPANSION,ZERO=25.
1.26E-5,850.
**********************************************************************
** Boundary conditions and nodal constraints.
**********************************************************************
*BOUNDARY
BOTTOM,2,,0.0
LEFT,1,,0.0
99,1,2,0.0
*EQUATION
2
101,2,1,100,2,-1
2
102,2,1,100,2,-1
2
103,2,1,100,2,-1
2
104,2,1,100,2,-1
2
105,2,1,100,2,-1
2
106,2,1,100,2,-1
2
107,2,1,100,2,-1
2
108,2,1,100,2,-1
2
109,2,1,100,2,-1
2
110,2,1,100,2,-1
2
111,2,1,100,2,-1
2
112,2,1,100,2,-1
2
113,2,1,100,2,-1
2
114,2,1,100,2,-1
2
115,2,1,100,2,-1
2
116,2,1,100,2,-1
2
117,2,1,100,2,-1
2
118,2,1,100,2,-1
2
119,2,1,100,2,-1
2
120,2,1,100,2,-1
2
121,2,1,100,2,-1
2
122,2,1,100,2,-1
2
123,2,1,100,2,-1
2
124,2,1,100,2,-1
2
125,2,1,100,2,-1
```

```
2
126,2,1,100,2,-1
2
127,2,1,100,2,-1
2
128,2,1,100,2,-1
2
130,2,1,100,2,-1
2
132,2,1,100,2,-1
2
134,2,1,100,2,-1
2
136,2,1,100,2,-1
2
138,2,1,100,2,-1
2
140,2,1,100,2,-1
2
142,2,1,100,2,-1
2
144,2,1,100,2,-1
2
160,2,1,1552,2,-1
2
4252,1,1,4352,1,-1
2
4152,1,1,4352,1,-1
2
4052,1,1,4352,1,-1
2
3952,1,1,4352,1,-1
2
3852,1,1,4352,1,-1
2
3752,1,1,4352,1,-1
2
3652,1,1,4352,1,-1
2
3552,1,1,4352,1,-1
2
3452,1,1,4352,1,-1
2
3352,1,1,4352,1,-1
2
3252,1,1,4352,1,-1
2
3152,1,1,4352,1,-1
2
3052,1,1,4352,1,-1
2
2952,1,1,4352,1,-1
2
2852,1,1,4352,1,-1
2
2752,1,1,4352,1,-1
2
2652,1,1,4352,1,-1
2
2552,1,1,4352,1,-1
2
2452,1,1,4352,1,-1
2
```

```
2352,1,1,4352,1,-1
2
2252,1,1,4352,1,-1
2
2152,1,1,4352,1,-1
2
2052,1,1,4352,1,-1
2
1952,1,1,4352,1,-1
2
1852,1,1,4352,1,-1
2
1752,1,1,4352,1,-1
2
1652,1,1,4352,1,-1
2
1552,1,1,4352,1,-1
2
160,1,1,4352,1,-1
2
158,1,1,4352,1,-1
2
156,1,1,4352,1,-1
2
154,1,1,4352,1,-1
2
152,1,1,4352,1,-1
2
150,1,1,4352,1,-1
2
148,1,1,4352,1,-1
2
146,1,1,4352,1,-1
2
144,1,1,4352,1,-1
**********************************************************************************
** Multi-point constraints for mesh refinement
**********************************************************************************
*MPC
2,1501,1500,1502,1504
2,1503,1500,1502,1504
2,1505,1504,1506,1508
2,1507,1504,1506,1508
2,1509,1508,1510,1512
2,1511,1508,1510,1512
2,1513,1512,1514,1516
2,1515,1512,1514,1516
2,1517,1516,1518,1520
2,1519,1516,1518,1520
2,1521,1520,1522,1524
2,1523,1520,1522,1524
2,1525,1524,1526,1528
2,1527,1524,1526,1528
2,1628,1528,1728,1928
2,1828,1528,1728,1928
2,2028,1928,2128,2328
2,2228,1928,2128,2328
2,2428,2328,2528,2728
2,2628,2328,2528,2728
2,2828,2728,2928,3128
2,3028,2728,2928,3128
2,3228,3128,3328,3528
2,3428,3128,3328,3528
```

```
2,3628,3528,3728,3928
2,3828,3528,3728,3928
2,4028,3928,4128,4328
2,4228,3928,4128,4328
2,1902,1900,1904,1908
2,1906,1900,1904,1908
2,1910,1908,1912,1916
2,1914,1908,1912,1916
2,1918,1916,1920,1924
2,1922,1916,1920,1924
2,2124,1924,2324,2724
2,2524,1924,2324,2724
2,2924,2724,3124,3524
2,3324,2724,3124,3524
2,3724,3524,3924,4324
2,4124,3524,3924,4324
2,1329,1328,1330,1332
2,1331,1328,1330,1332
2,1381,1332,1430,1530
2,1480,1332,1430,1530
2,930,928,932,936
2,934,928,932,936
2,1138,1136,1140,1144
2,1142,1136,1140,1144
2,954,952,956,1536
2,958,952,956,1536
2,1146,1144,1148,1152
2,1150,1144,1148,1152
9,1531,1260
9,1550,260
9,1548,360
9,1546,460
9,1544,560
9,1542,660
9,1540,760
9,1538,860
9,1536,960
9,1534,1060
9,1532,1160
9,1244,1332
**********************************************************************
** Plotting of the mesh before loading
**********************************************************************
*PLOT
*DRAW
**DETAIL,ELSET=GAMMA
**DRAW,ELNUM
**DETAIL,ELSET=GAMMAP
**DRAW,ELNUM
**DETAIL,ELSET=BORDER
**DRAW,ELNUM,NODENUM
**********************************************************************
** Definition of rate of load application and initial conditions
**********************************************************************
*AMPLITUDE,TIME=V,NAME=LOWER
0.0,0.0,1.0,1.0
*INITIAL CONDITIONS,TYPE=TEMPERATURE
ALL,25.
*RESTART,WRITE,FREQ=40
**********************************************************************
** Heating of material from room temperature to 850 C, during this step the
**thermal expansion induces the misfit.
**********************************************************************
```

```
*STEP,LINEAR
*STATIC
*TEMPERATURE
ALL,850.
*EL PRINT,ELSET=PR
2,2,1,1,1
2,1,2,1,1
*NODE PRINT,NSET=NOUT
2,1,1,1,1,1
*END STEP
** Application of load and creep analysis.
*STEP,INC=60
*VISCO,PTOL=0.15,CETOL=7.0E-4
0.001,6.0E5
*CLOAD,AMP=LOWER
100,2,200.
**********************************************************************************
** Definition of output data and contour plots.
**********************************************************************************
*EL PRINT,ELSET=BORDER,FREQ=60
2,2,1,1,2,1,2,1,1,1,1
*EL PRINT,ELSET=ELOUT,FREQ=20
2,2,1,1,2,1,2,1,1,1,1
*NODE PRINT, NSET=NOUT,FREQ=1
2,1,1,1,1,1
*PLOT,FREQ=30
*DISPLACED
1,,1
*DETAIL,ELSET=GAMMA
*CONTOUR
9
11
47
42
*DETAIL,ELSET=GAMMAP
*CONTOUR
9
11
*NODE FILE ,NSET=L,FREQ=5
2,1,1,1,1,1
*END STEP
```